What the fish's eye tells the fish's brain: the functional complement of zebrafish retinal ganglion cells

Mingyi Zhou

Submitted for the degree of Doctor of Philosophy

University of Sussex

December 2020

Declaration

Part of this thesis incorporates collaborative work and as such contains data collected and/or analysed by others in order to provide context to results and inform complete discussion.

Specifically, chapter 3 includes data that has been published in a peer-reviewed journal, and adapted by Mingyi Zhou:

Zebrafish retinal ganglion cells asymmetrically encode spectral and temporal information across visual space

Zhou M*, Bear J*, Roberts PA, Janiak FK, Semmelhack J, Yoshimatsu T & Baden T.

Current Biology 30: 1-16. 2020. DOI: 10.1016/j.cub.2020.05.055. *co-first author

Contributions by others:
JB performed anatomical experiments, retinal counts and associated data processing (included in Supplementary material; Discussion); TY computed cell-density projections into visual space (Supplementary material); PAR performed clustering analyses; TB performed additional data analyses.

Throughout this thesis, all other data presented is my own original work unless specifically declared otherwise.

I hereby declare that this thesis has not been and will not be, submitted in whole or in part to another University for the award of any other degree.

Signature:

Acknowledgements

I'd like to give my heartfelt thanks to the following: my advisor Tom Baden for his invaluable mentorship and stimulating ideas, and for making neuroscience fun; my thesis advisory committee Prof. Leon Lagnado (co-advisor), Prof. Miguel Maravall and Prof. Jeremy Niven for their illuminating perspectives; colleagues at the Baden lab, especially Takeshi for showing me the ropes and being there every step of my journey, Natasha for being the life of the lab; and of course, my family.

Abstract

In the vertebrate retina, incoming visual information is split into parallel information channels and sent to the brain by distinct types of retinal ganglion cells (RGCs) (Masland, 2012). In mouse, a minimum of 32 RGC types, and possibly as many as 50, have been charted functionally (Baden et al., 2016), anatomically (www.museum.eyewire.org; – see also RGCtypes.org) (see also Sanes and Masland, 2015) and transcriptomically (Bae et al., 2018). However, a similarly detailed understanding of the complement of zebrafish RGCs and their underlying feature-extracting microcircuits is lacking. Here, we performed *in vivo* two-photon population imaging of light-evoked calcium activity in the tetrachromatic zebrafish during hyperspectral visual stimulation, to functionally chart what the fish's eye tells the fish's brain.

For this, we generated a novel transgenic line in which the calcium reporter GCaMP6f is tagged to the membrane of zebrafish RGCs under the Islet2b promoter, allowing recording from both RGC dendrites and somata. We find that RGC functional properties varied strongly with position in the eye, including a regional specialisation of UV-responsive On-sustained RGCs in the acute zone, likely to support visual prey capture. Interestingly half of RGCs display diverse forms of colour opponency, among which many are driven by a pervasive and slow blue-Off system, challenging classical models of colour vision. In addition, spectral contrast was intermixed with temporal information. Taken together, our data suggest a highly regionalized time-colour code that asymmetrically encodes distinct regions in visual space, mirroring our earlier finding in bipolar cells that different parts of the eye harbour strongly diverse functional circuits (Zimmermann et al. 2018).

Working toward more ecologically and behaviourally relevant stimuli, we next used a novel prototype of a tetrachromatic spatial stimulator (Franke et al. 2019) to map receptive fields, and potentially make better sense of more complex contextual effects such as sensitivity to a certain orientation or direction of motion. Crucially, analysing receptive fields in a population of cells can provide insight into the visual features extracted at a particular stage along the visual pathway.

Table of Contents

List of Figures

List of Movies

3.1. Supplementary Video 1. Example 2P scan from RGCs in the *in vivo* eye
https://ars.els-cdn.com/content/image/1-s2.0-S0960982220307429-mmc2.mp4

3.2. Supplementary Video 2. RGC dendritic mean responses across the eye to a step of light
https://ars.els-cdn.com/content/image/1-s2.0-S0960982220307429-mmc3.mp4

3.3. Supplementary Video 3. RGC dendritic mean responses across the eye to temporal flicker
https://ars.els-cdn.com/content/image/1-s2.0-S0960982220307429-mmc4.mp4

3.4. Supplementary Video 4. RGC dendritic mean 4-colour kernels across the eye
https://ars.els-cdn.com/content/image/1-s2.0-S0960982220307429-mmc5.mp4

List of Abbreviations

2P	Two-photon
AC	Amacrine cell
AF	Arborisation field
AZ	Acute zone
AMPA	α-Amino-3-hydroxy-5-methyl-4- isoxazolepropionic acid
BC	Bipolar cell
dpf	Days post fertilisation
DiI	1,1'-Dioctadecyl-3,3,3'3'-Tetramethylindocarbocyanine Perchlorate
GABA	Gamma-aminobutyric acid
GCL	Ganglion cell layer
HC	Horizontal cell
INL	Inner nuclear layer
IPL	Inner plexiform layer
LED	Light-emitting diode
mGluR	Metabotropic glutamate receptor
ms	Milliseconds
OMR	Optomotor response
OMS	Object motion sensitive
ONL	Outer nuclear layer
OOi	On-Off index
OPL	Outer plexiform layer
PBS	Phosphate-buffered saline
PFA	Paraformaldehyde
PR	Photoreceptor
PTU	n-phenylthiourea / 1-phenyl-2-thiourea
RBC	Rod bipolar cell
RF	Receptive field
RGC	Retinal ganglion cell
ROI	Region of interest
s	Seconds

UAS	Upstream activation sequence
µm	Micrometre
UV	Ultraviolet

Chapter 1

Introduction

1.1. The retina encodes the visual world

What type of information about the visual scene does the eye communicate to the brain? This question has long intrigued neuroscientists since the early recordings of spikes transmitted by individual optic nerve fibres of the frog (Hartline, 1938). The fundamental observation was that these fibres displayed distinct responses; some spiked at the onset of illumination (ON ganglion cells), others at offset (OFF ganglion cells); yet another separate class responded to both (ON-OFF ganglion cells). Evidently, a stimulus as simple as a step of uniform light could be simultaneously transformed in multiple ways by the retinal circuitry; which brings us to the question – what about more complex visual stimuli that the animal experiences in its natural environment? How are these visual features extracted and represented in signals the retina conveys to the brain?

1.1.1. Discrete neural circuits for different visual tasks

This enigma leads us to the concept of feature detection, which posits that the visual system filters natural stimuli to preferentially encode information most relevant to behaviour. The potential for such sophisticated processing within the retina was elegantly described by Lettvin, in what has now become one of the seminal papers in sensory neuroscience "What the Frog's Eye Tells the Frog's Brain" (Lettvin et al., 1959). In brief, complex stimuli derived from the frog's behaviour, driven by vision, singled out retinal ganglion cells (RGCs) that responded particularly robustly to a small dark object making intermittent jerky movements – a detector Lettvin coined the "bug perceiver". The idea was that a fly within striking distance would make an effective stimulus for these retinal neurons, which in turn convey encoded information to the region of the brain driving the capture of prey. For decades, a simplistic model of retinal function had prevailed – that the retina was merely a sensory structure for light detection, faithfully forwarding a copy of the mosaic of impulses to the

brain for interpretation. Contrary to conventional wisdom then, Lettvin et al. showed there exist feature detector neurons tuned to specific features of a visual stimulus – edges, contrast or motion, to name a few. In short, feature selectivity is already apparent in the inner retina, orchestrated by a network of microcircuitries. Since then, similar detectors have been suggested in multiple species; one being the "hawk detector" in the mouse retina – a motion sensitive ON-OFF retinal ganglion cell predisposed to respond to overhead circling birds of prey (Zhang et al., 2012).

While it remains unknown how many discrete retinal feature channels exist and what they encode, it is without doubt retinal processing is far more extensive than initially assumed (Fig. 1.1; Gollisch and Meister, 2010; Baden et al., 2016). Indeed differential encoding had been shown to be present at the level of retinal output in early experiments: the rabbit retina revealed RGCs with complex response properties encoding stimulus motion; some responded robustly to visual stimuli moving solely in one direction and not the others (Barlow and Hill, 1963). Experiments have since been finetuned to demonstrate both the presence of orientation- and direction- selective ganglion cells at the level of RGCs (Nikolaou et al. 2012; Gabriel et al. 2012, Lowe et al. 2013). In brief, each of the numerous ganglion cell types computes something specific about the visual scene; each type would then require a dedicated neural circuit to extract the visual feature of interest. The resultant downstream brain regions receive not a generic pixel-by-pixel copy of the image but a highly processed set of extracted features. At last count, at least 30 unique functional types of ganglion cells were suggested in the mammalian retina (Fig. 1.1; Sanes and Masland, 2015; Baden et al., 2016), which translates to upwards of 30 distinct parallel pathways in the retina.

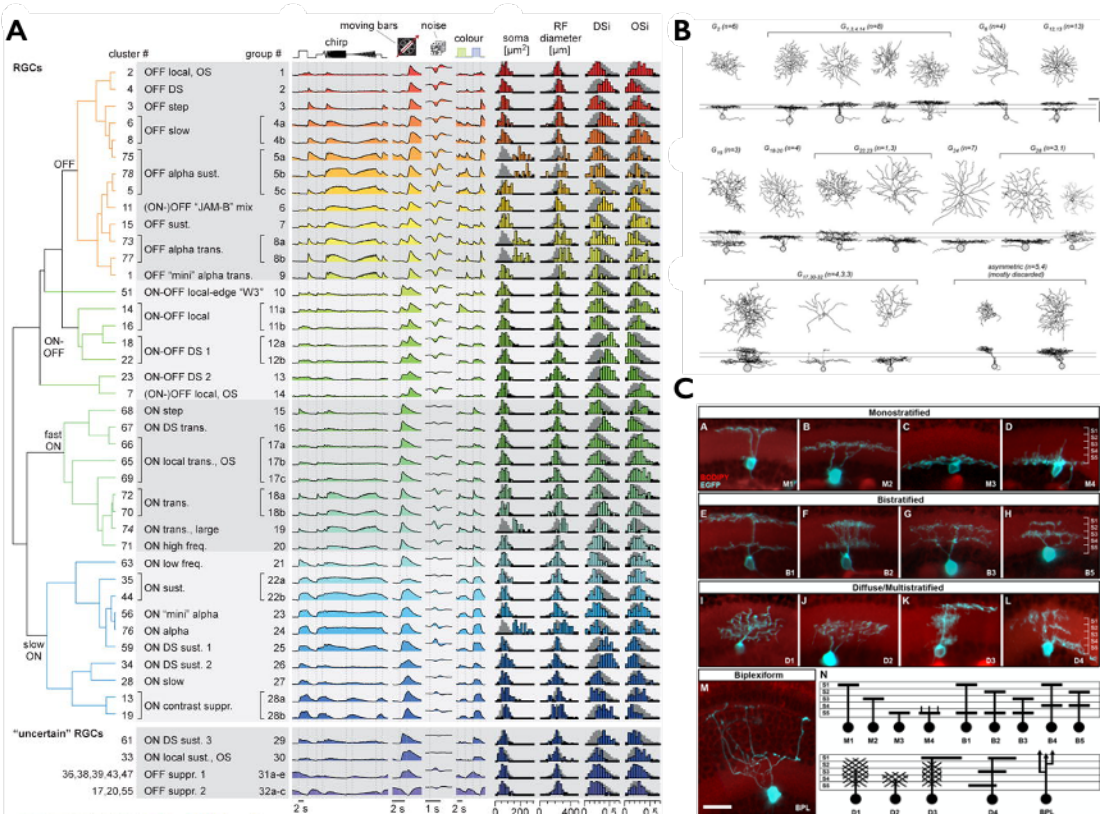

Figure 1.1. | Functional and anatomical mapping of RGC types in the vertebrate retina. A, Functional RGC types of the mouse retina. From left to right: Cluster-dendrogram of 28 functional groups and 4 "uncertain" (bottom); Cluster-mean Ca^{2+} responses to four types of stimuli: frequency chirp, moving bars, noise and colour steps; Selected metrics: region of interest (soma) area, receptive field (RF) diameter, direction-selectivity index (DSi), and orientation selectivity index (OSi). **B,** Mapping functional groups to morphologies. Example morphologies of mouse RGCs filled after electrical recording or Ca^{2+} imaging and subsequent sorting into specific RGC groups based on their light response. Scale bars, 50 µm. Images in A and B are from Baden et al., 2016. **C,** RGC classification based on dendritic stratification patterns. Panels *A-L*, The four major groups of RGCs in the larval zebrafish according to dendritic stratification – monostratified, bistratified, multistratified, and diffuse – can be further subdivided based on laminar position within the IPL. Panel *M*, Biplexiform RGCs form dendrites that span the INL to reach the OPL. Scale bar 12.5 µm Panel *N*, Schematic summary of 14 RGC classes defined by IPL stratification. Images from Robles et al., 2014.

In parallel, Robles and colleagues (Robles et al. 2014) detailed the first comprehensive anatomical connectivity map linking the retina and their target areas in the zebrafish. When both dendritic arborization in the inner plexiform layer (IPL) and axonal projection patterns to the brain were taken into account, data suggest at least 50 types of morphologically distinct RGCs in the larval zebrafish retina exist. Further, the study reaffirmed a key organizing principle of the vertebrate visual system – the divergence and convergence of ganglion cell pathways. Crucially, RGCs send axon collaterals to various combinations of tectal and extratectal target sites, while these innervation sites in turn

receive combinatorial projections of RGCs with varying dendritic morphologies. Moreover Robles et al. went on to show that ganglion cells with similar dendritic stratification profiles may display heterogeneous axonal projection patterns as some projection sites receive precisely-coordinated input from a part of the retinal surface, e.g., nasal or temporal. This topographic bias lends weight to the notion of specialised retinal regions for ecological motivation, such as detection of prey or predators in visual space. Clearly, such anatomical diversity suggests there is much function still to be discovered and we have a good distance to go before fully understanding the immense image processing performed at the front end of the visual system. At present, the functional characterisation of RGC types within the retina and their physiological responses are sorely lacking.

1.1.2. A parallel flow of information in the retinal vertical pathway

Animal eyes have evolved to filter behaviourally relevant visual information just as sensory systems have evolved to serve their behavioural needs, subject to constraints in neural hardware and metabolic cost (Land et al., 2012). Well conserved across vertebrates, the retina forms the neural layer of the eye and is a multi-laminar neuronal network comprising five canonical retinal cell types – photoreceptor, horizontal cell, bipolar cell, amacrine cell and ganglion cell (Fig. 1.2). Structurally and functionally organized into laminae, the retinal neurons are ordered by three nuclear and two synaptic (plexiform) layers (Masland, 2001; Wässle, 2004). The outermost layer, the outer nuclear layer (ONL), is populated by photoreceptors. The ONL borders the outer plexiform layer (OPL) – the synaptic layer between photoreceptors and the inner nuclear layer (INL), where retinal interneurons horizontal cells, amacrine cells and bipolar cells reside. Finally, the IPL forms the synaptic layer between the INL and the ganglion cell layer (GCL). There is minimal variation in

gross retinal structure throughout evolution, the major difference being the numbers of neuronal subtypes between species (Baden et al., 2020).

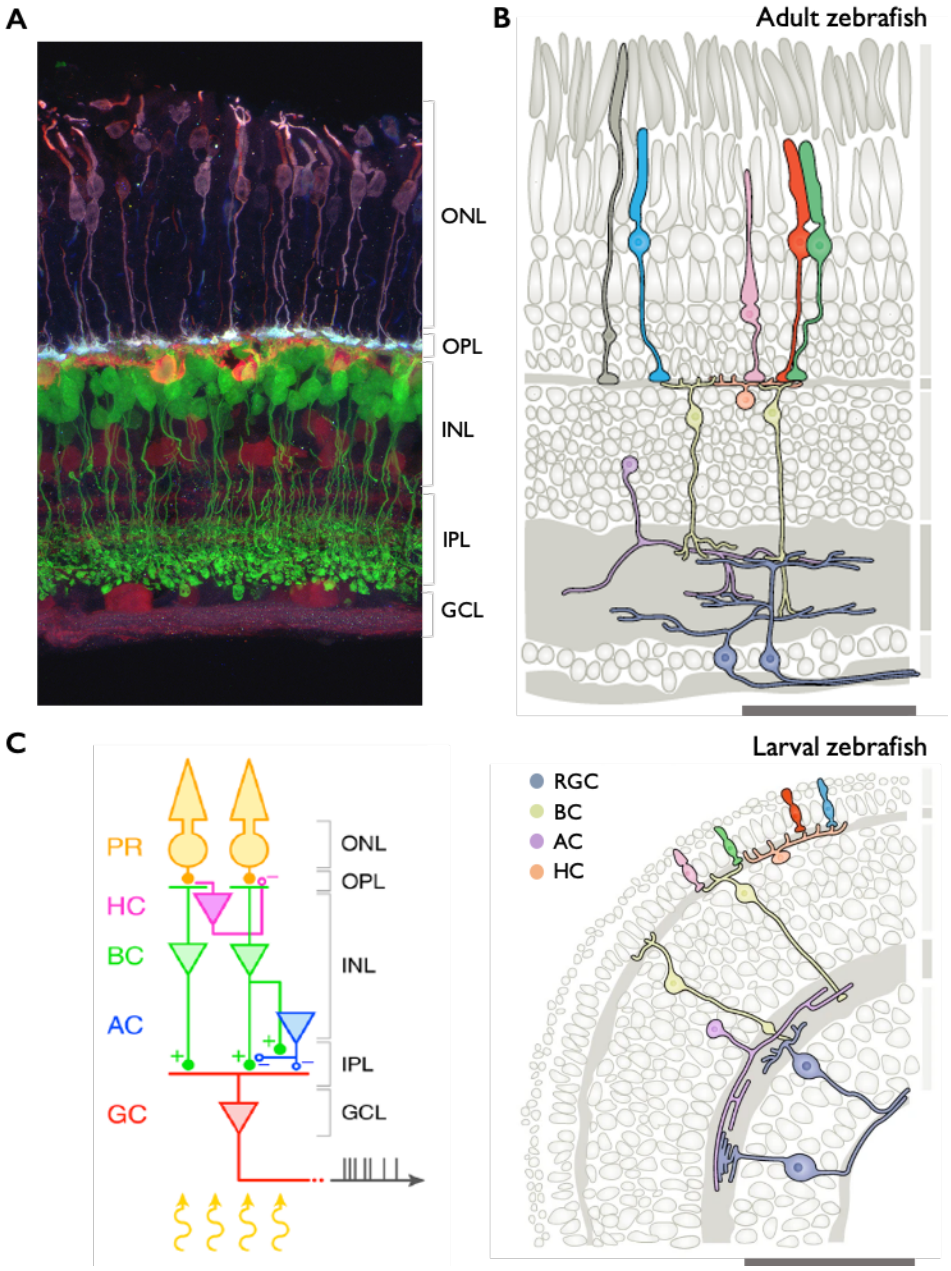

Figure 1.2. | **Cellular and synaptic lamination of the vertebrate retina. A,** Vertical section of an immunostained mouse retina with cones in purple (anti-cone arrestin); horizontal cells in orange (calbindin); bipolar cells in green (expression of mGlu6 promoter-driven GFP); amacrine and retinal ganglion cells in red (calbindin). Image by Josh Morgan (Rachel Wong lab). **B,** Schematic traverse section of the retinal composition of the adult zebrafish (top); contrast with larval zebrafish (bottom). The plexiform (synaptic) layers, the outer plexiform layer and inner plexiform layer are demarcated alongside each image. Example morphologies of different retinal neuron classes are highlighted. Scale bars 50 µm. Images from Baden et al., 2020. **C,** Basic neural circuit structure of the vertebrate retina. Cell classes are shown in colours, while layers are labelled in black. Excitatory synapses are indicated by '+' (filled circles), and inhibitory synapses with '-' (empty circles). Image from Antinucci et al., 2016. AC: amacrine cell; BC: bipolar cell; GC/RGC: ganglion cell/retinal ganglion cell; GCL: ganglion cell layer; HC: horizontal cell; INL: inner nuclear layer; IPL: inner plexiform layer; ONL: outer nuclear layer; OPL: outer plexiform layer; PR: photoreceptor.

The retina, akin to a miniaturized, computational nervous tissue lining the back of the eye, performs the first stage of visual processing. Light incident on the retina triggers a cascade of electrochemical reactions, relayed via a series of retinal neurons to the brain. In brief, incoming photons of light are converted into neural potentials through phototransduction by the outer segments of photoreceptors. These graded signals are relayed in a vertical excitatory pathway via glutamatergic synapses, to a layer of bipolar cells for further processing, and finally to RGCs, the sole output neurons of the vertebrate retina. In between these nuclear layers, synaptic inputs from horizontal cells in the OPL and amacrine cells in the IPL modulate and shape the flow of signals, predominantly by lateral inhibitory signal processing (Diamond 2017; Franke and Baden, 2017). Distinct types of RGCs then integrate and relay feature-specific information such as orientation of a stimulus or direction of motion, along multiple discrete channels to higher visual areas, encoded in the form of trains of action potentials or spikes (Wässle 2004; Masland, 2012a; Roska and Meister, 2014). As a result, information extracted from the environment becomes increasingly descriptive as it flows through the retina.

1.1.3. Discrete circuits are established through differential connectivity and receptor expression

At the first stage of convergence within the OPL, bipolar cells pool inputs from multiple photoreceptors – coupled with gain control by horizontal cells – propagate this signal to the GCL (Fig. 1.3A). The divergence of ON and OFF bipolar cells is dependent on receptor expression – namely metabotropic mGluR, or ionotropic AMPA or kainate receptors (DeVries, 2000; Puller et al., 2013; Lindstrom et al., 2014). ON and OFF bipolar cells can be further subdivided based on their temporal response properties – transient or sustained

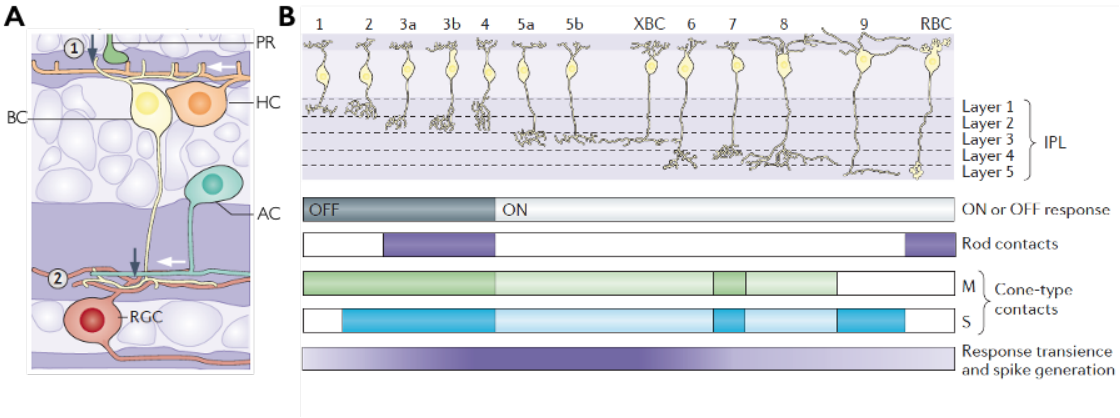

Figure 1.3. | **Bipolar cell differential connectivity in the mouse retina. A,** Vertical pathway modulated by lateral interactions. Bipolar cells (BCs) receive glutamatergic input from photoreceptors (PRs) and GABAergic input from horizontal cells (HCs) (site 1) and in turn provide glutamatergic excitatory input to retinal ganglion cells (RGCs) and inhibitory amacrine cells (ACs) (site 2). **B,** Morphological features of the types of cone bipolar cells and the rod bipolar cell (RBC) in the mouse retina. Note that each bipolar cell type has a characteristic axonal stratification pattern traversing the inner plexiform layer (IPL). Listed below are some functional properties of the bipolar cell types. Depending on the polarity of their light response, bipolar cells can be divided into ON or OFF cells. Some bipolar cells relay scotopic light signals from rods (purple bars). Mice possess short (S; blue) and medium (M; green) wavelength-sensitive cones, with many M-cones co-expressing S-opsin. Depending on the cone type (or types) they contact, bipolar cells can be classified as chromatic or achromatic (light bars indicate probable but not yet experimentally confirmed contacts). Bipolar cells with terminals in the central bulk of the IPL show more transient responses, and often generate action potentials, than those closer to the IPL borders. XBC represents a newly described mouse bipolar cell type. Images from Euler et al., 2014.

(Fig. 1.3B). Similarly, the distinction between transient and sustained bipolar cells can be attributed to rapidly or slowly inactivating glutamate receptors recovering from desensitisation (Awatramani and Slaughter, 2000). In sum, RGCs inherit physiological properties of bipolar cells in a combinatorial way, selectively sampling lamina-specified bipolar cell synapses within the IPL, subject to amacrine cell modulation (de Vries et al., 2011; Eggers and Lukasiewicz, 2011; Kim et al., 2014; Roska et al., 1998; Roska and Werblin, 2001). Given the diversity of bipolar and amacrine cell types, differential wiring of these interneurons to ganglion cells could substantially increase the number of discrete pathways in the inner retina, creating ganglion cell circuits specialized in specific retinal functions such as selectivity to certain orientations or sensitivity to motion in one direction (Antinucci et al., 2016; Baccus et al., 2008; Briggman et al., 2011; Ding et al., 2016; Euler

et al., 2002; Fried et al., 2002; Johnston, J. et al., 2019; Kim et al., 2015; Matsumoto et al., 2019; Münch et al., 2009; Zhang et al., 2012).

Often, functional types of RGCs respond to stimuli smaller than their receptive fields; it is likely these sub-receptive field responses are the resultant influence of amacrine cells, whose arbours go down to tens of microns. Interestingly, these arbours can both receive excitatory glutamatergic inputs and release inhibitory GABAergic outputs to the same bipolar cell synapses. Indeed, the functional importance of amacrine cells is evident from the sheer diversity of their subtypes, and neurotransmitters, that exist in the retina (MacNeil and Masland, 1998; Masland, 2012b). While most bipolar cells and ganglion cells extend processes into just one or two strata of the IPL, narrow-field amacrine cells extend their arbours vertically, spanning several strata. These amacrine cells perform vertical integration, predominantly in the form of crossover inhibition (Demb and Singer, 2012; Roska and Werblin, 2001; Werblin, 2010). Conversely wide-field amacrine cells, as their name suggests, are thinly stratified and extend their processes horizontally. These amacrine cells introduce contextual effects to the ganglion cell response via lateral inhibition, such as centre surround antagonism and motion relative to background (Gollisch and Meister, 2010; Ölveczky et al., 2003).

1.1.4. Lateral inhibition drives centre-surround responses in a receptive field

Hartline first used the term receptive field for the spatial region of retina within which a local change of brightness would cause the ganglion cell he was observing to discharge (Hartline, 1938). To paraphrase, the receptive field provides a description of its response properties, i.e., the nature and position of a stimulus that excites the cell. Cells in each neural layer of the retina can be described as having receptive fields. Crucially, analysing receptive fields in a population of cells can provide insight into the visual features extracted

at a particular stage along the visual pathway. The (now textbook) classic organisation of the retinal ganglion cell receptive field refers to a concentric ring structure with a centre and an antagonistic surround. Central responses can be ON with an OFF-surround or vice versa. For an ON-centre cell, a light stimulus in proximity of the centre evokes a burst of spikes at stimulus onset, while a light stimulus at the periphery evokes spiking at offset. The converse is true for an Off-centre cell. When both centre and periphery are stimulated simultaneously, the two regions antagonise each other.

Lateral inhibition within the receptive field in the vertebrate retina was first described, in separate studies, by Barlow and Kuffler (Barlow, 1953; Kuffler, 1953). Expanding upon Hartline's experiments in isolated retinae of frogs, Barlow observed that for ON-OFF ganglion cells, sensitivity to light spots decreased with increasing spot size, attributing this effect to inhibition on the receptive field centre. Further, an ON-OFF cell appeared to be particularly sensitive to local contrast of illumination, and thus motion, within its receptive field. Similarly, extending receptive field research to the mammalian visual system, Kuffler showed evidence of inhibitory surround and mutual antagonism in the ganglion cell receptive fields of cats. Collectively, their landmark research laid the foundation that inhibition plays a key role in enhancing contrast and visual acuity (Barlow, 1953; Kuffler, 1953). The inhibitory surround enables spatial frequency tuning as sensitivity to stimulation diminishes radially from the centre; ideally for maximal response, there is a large contrast between the light and dark phases. As mentioned, centre-surround responses is a common mechanism in the retina: at the first synapse, horizontal cells confer bipolar cell centre-surround receptive fields by feedforward inhibition, while amacrine cells mediate at the level of the bipolar cell-ganglion cell synapse to construct spatially complex receptive fields (Masland, 2001). At this second synapse, the variety in these cell types and

circuits form the basis of ganglion cell functional microcircuits. In sum, the receptive field of any cell can be thought of as the convolution of the primary inputs to that cell and the properties of the microcircuit that processes those inputs.

1.2. Retinal circuits for colour vision

Like motion, colour – generated as a function of the wavelength of light detected, as opposed to its intensity – is a layer of information that can be extracted from visual scenes. Chromatic pathways originate in the retina, where signals from spectrally distinct photoreceptor types are locally compared by downstream retinal circuits to extract chromatic information present in the visual input (Dacey, 2000; Neitz and Neitz, 2011; Thoreson and Dacey, 2019). Within the outer segment of the photoreceptor, a chromophore covalently bound to an opsin initiates phototransduction upon photon absorption (Hubbard and Kropf, 1958). Photoreceptors translate light of distinct wavelengths into levels of brightness as a function of their opsin's spectral sensitivity. Each individual photoreceptor is effectively colour blind; the synaptic output of a single cone is a photocurrent which can vary only in magnitude. To differentially probe the spectrum of light and discriminate among wavelengths, the signal outputs of at least two types of cones with opsins of different spectral sensitivity must be compared (Krauskopf et al. 1982).

1.2.1. Diverse species-specific photoreceptor spectral sensitivities

Most vertebrates feature at least two spectral cone types – one sensitive to short wavelengths (S-cone; "blue" or "UV") and a second sensitive to longer ("medium") wavelengths (M-cone; "green") (Fig. 1.4; Dacey, 2000; Neitz and Neitz, 2011). This blue-green (S vs. M) opponency represents most terrestrial mammals and forms the basis of dichromatic colour vision (Fig.

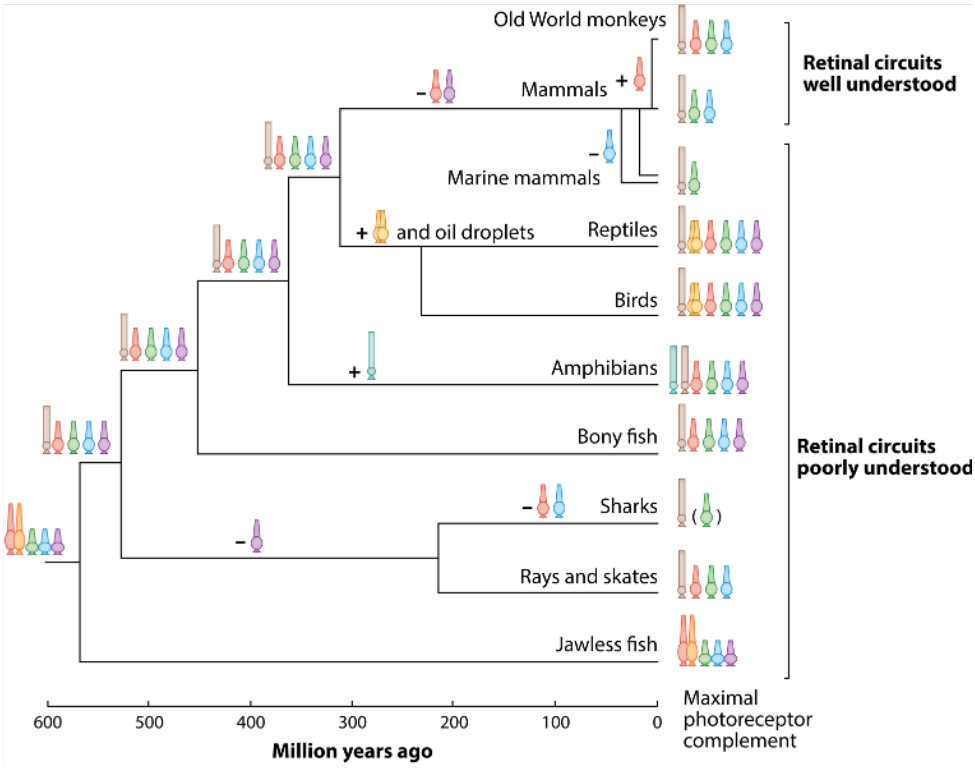

Figure 1.4. | Photoreceptor lineages. The ancient photoreceptor completement of jawless ancestral vertebrates (leftmost) gave rise to the photoreceptor complements present in jawed vertebrates today (right). At various time points along the way, different lineages added or lost particular photoreceptors: rods (beige), L cones (red), M cones (green), S cones (blue), UV cones (purple), blue rods (teal), double cones (yellow). L-type cones of jawless fish (longer icon) have a rod-like physiology (Morshedian and Fain, 2015). Photoreceptor complements shown depict the typical diversity in a lineage – often, individual groups use fewer. Image from Baden and Osorio, 2019.

1.5; Neitz and Neitz, 2011; Puller and Haverkamp, 2011). An evolutionary recent gene duplication event led to a subset of primates inheriting an additional cone type with a red-shifted opsin sensitive to longer-still wavelengths (L-cone; 'red') to become trichromats (Fig. 1.4; Nathans, 1999). Here, signals from short (S; 'blue'), medium (M; 'green') and long (L; 'red') wavelength-sensitive cones are processed along two main opponent pathways: red-green (L vs. M) and blue-yellow opponency (S vs. L+M) – the primate's equivalent of the blue-green pathway (Thoreson and Dacey, 2019; Zrenner and Gouras, 1981). While red-green opponency largely relies on cone type-unselective circuits of the high-acuity midget system (Buzás et al., 2006; Crook et al., 2011; Field et al., 2010; Martin et al., 2001; Wool et al., 2019), precise wiring in cone type-selective retinal circuits drives blue-yellow

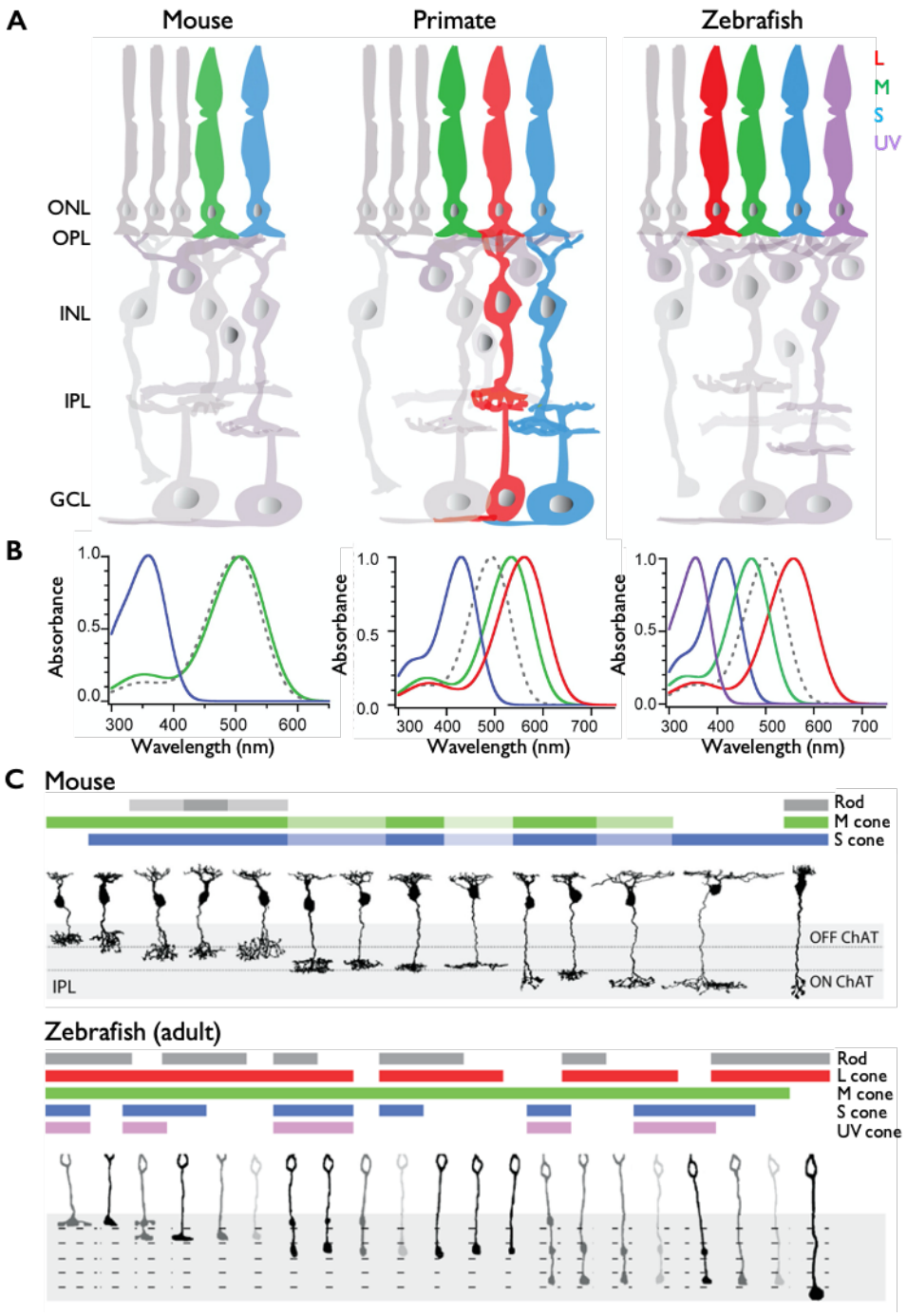

Figure 1.5. | Cone composition across species and common synaptic motifs. A, The retinae of mouse, primate (macaque) and zebrafish share a common basic architecture, with functional variations. Notably, cone composition and corresponding opsin expression, and their connectivity vary across species. L: long; M: medium; S: short; UV: ultraviolet. Primate retina has pathways dedicated for colour processing as indicated by L and S cone pathways. GCL: ganglion cell layer; INL: inner nuclear layer; IPL: inner plexiform layer; ONL: outer nuclear layer; OPL: outer plexiform layer. **B,** Absorption spectra of the variation of cone opsins across species (coloured lines) compared to rhodopsin (dotted line). Images in A and B are from Hoon et al., 2014. **C,** Wiring photoreceptors to bipolar cells. Top: The 14 mouse bipolar cell types make mostly cone-type nonselective contacts in the outer retina. Only types 1 (leftmost) and 9 (second from right) bipolar cells make selective contacts with M and S cones respectively. Rods are contacted by rod bipolar cells and a subset of Off bipolar cells. Bottom: Adult zebrafish have more than 20 bipolar cells that make diverse sets of contacts across the four cone types and one rod type in the outer retina. Images from Baden and Osorio, 2019.

opponency (Calkins et al., 1998; Crook et al., 2009; Dacey and Lee, 1994; Puller and Haverkamp, 2011; Sher and DeVries, 2012). Most teleost fish express four types of cone opsins, and tetrachromacy has been shown in goldfish and zebrafish (Fig. 1.5; Chinen et al., 2003; Neumeyer, 1992). Many birds and reptiles possess four or even five spectral cone types, containing coloured oil droplets that narrow spectral filtering (Fig. 1.4; Arnold and Neumeyer, 1987; Bowmaker et al. 1997; Hart & Hunt 2007; Toomey et al. 2015).

1.2.2. Colour opponency at the first retinal synapse

Vertebrate colour vision originates at the first synapse in the outer retina where horizontal cells mediate inhibitory interactions between cones (Chapot et al. 2017b; Perlman et al. 2009). Bidirectional feedback between horizontal cells and photoreceptor terminals or pedicles (Thoreson et al., 2008; Twig et al., 2003) alongside lateral inhibition generate colour opponency (Crook et al., 2009; Packer et al., 2010). As individual photoreceptors occupy distinct retinal locations, colour opponency has a spatial component. Spectral responses of each horizontal cell type is dependent on its cone connections, including their type and gain (Baden et al. 2013; Breuninger et al. 2011; Chapot et al. 2017a; Connaughton & Nelson 2010; Kamermans et al. 1991; Li et al. 2009). Many species possess several types of horizontal cells, each with distinct cone-selective connections and complex chromatic properties (Connaughton & Nelson 2010, Kamermans et al. 1991, Packer et al. 2010). How these inhibitory interactions finally contribute to colour vision remains unclear.

1.2.3. Chromatic processing in the inner retina

Complex chromatic circuits exist in the vertebrate inner retina and are best understood in mammals (Baden et al. 2018; Dacey 2000; Euler et al. 2014; Lee et al. 2010). The cone

contact-specificity of a bipolar cell defines its chromatic tuning. Well-characterised in primates, the small bistratified RGC selectively integrates separate blue-ON and yellow-OFF excitatory inputs from cone type-selective BCs across its respective dendritic arbours in two strata of the IPL (Calkins et al. 1998; Crook et al. 2009; Dacey & Lee, 1994; Zrenner & Gouras 1981), with further modulation by chromatic AC inputs (Marshak and Mills, 2014). In dichromatic mammals such as guinea pig (Yin et al., 2009), rabbit (Mills et al., 2014), and ground squirrel (Sher and DeVries, 2012), a similar blue-green mechanism yields chromatically opponent RGCs.

1.2.4. Environmental adaptation leads to regional specialization

Retinal specializations such as cone-photoreceptor opsin-expression gradients in relation to asymmetric statistics in visual space has been described in vertebrate species as diverse as rodents, shrews, and hyenas (Calderone et al., 2003; Peichl, 2005). While opsin coexpression broadens the spectral tuning of individual cones, opsin expression anisotropies lead to differential regional opsin dominance (Applebury et al., 2000; Rohlich et al., 1994). In mouse dorsal retina, M-cones exclusively express M-opsin, while the same

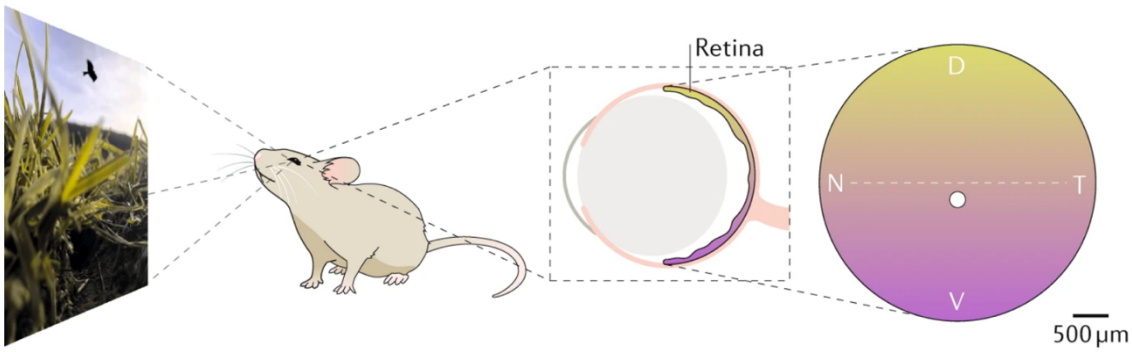

Figure 1.6. | Spectral asymmetry across the retina surface. The anisotropic gradient of cone photoreceptor opsin expression along the dorsoventral axis of the mouse retina. The retina of many visually orienting species appears to be anatomically and functionally divided into two domains, each concerned with visual information either above or below the horizon, which differ by spectral content and overall luminance. In mouse, this division is most evident at the level of cone-opsin expression – here, green-sensitive M cones dominate the ground-observing dorsal retina (approximate density indicated by green shading), while UV-sensitive S cones dominate the sky-observing ventral retina (purple shading). Image from Baden et al., 2020.

cone type progressively co-expresses S-opsin along the dorsoventral axis toward the ventral edge (Fig. 1.6). This increasing short-wavelength bias with elevation parallels the differential distribution of wavelengths above and below the visual horizon (Baden et al. 2013; Chapot et al., 2017a). The shift in spectral sensitivity of M cones in the ventral retina is thought to aid detection of the dark silhouette of an aerial predator against the bright backdrop of the sky (Baden et al. 2013).

1.2.5. Zebrafish colour vision

Expressing four types of cone photoreceptors and corresponding opsin variants, the larval zebrafish has the potential to perceive colour in a tetrachromatic space (Raymond et al., 1993). Its four cones are centered at 360 nm (UV), 415 nm (blue), 477 nm (green), and 565 nm (red) (Cameron, 2002; Endeman et al., 2013; Robinson et al., 1993). Additionally, gene duplication allows the zebrafish to express different opsin variants in a given cone (Chinen et al. 2003). In the adult retina, a crystalline mosaic of four spectral cone types comprising alternating rows of double cones with red (LWS opsin) and green (RH2 opsin) pairs, and single blue (SWS2 opsin) and UV (SWS1 opsin) cones (Allison et al. 2010, Engström 1960, Raymond et al. 1993) form relative densities of 2:2:1:1. In contrast, the relative distribution of different photoreceptor types are non-uniform and vary across the larval retina, likely reflecting behavioural specialization (Fig. 1.7A; Zimmermann et al. 2018).

The zebrafish outer retina has at least three types of cone-selective horizontal cells that differentially integrate four cone types, generating mono-, bi-, and triphasic spectral responses (Meier et al. 2018). Cone-type-specific wiring of horizontal cells observed in the adult retina (Connaughton and Nelson, 2010; Song et al., 2008) were shown in the early stages of larval development (Yoshimatsu et al. 2014), hinting at their role in shaping

colour-opponent signals. Reports on the specificity of horizontal cell-photoreceptor (Li et al., 2009) and bipolar cell-photoreceptor connectivity (Li et al., 2012), in combination suggests putative, cone-type selective input patterns feed into RGCs at the end of the retinal pathway. Further, single-cell electrophysiology in zebrafish retina ranging from horizontal cells to ganglion cells reveal rich colour opponencies (Connaughton & Nelson 2010, 2015; Klaassen et al. 2016; Torvund et al. 2017); however recent imaging of bipolar cell synapses in larval zebrafish (Zimmermann et al. 2018) suggests otherwise that only few combinations are in use (Baden and Osorio, 2019).

1.2.6. Regional specialisation in the larval zebrafish retina

Recent two-photon calcium imaging of BC terminals in the live larval zebrafish eye revealed a rich diversity of spectral responses ranging from achromatic, tetrachromatic, opponent, and even UV-specific (Fig. 1.7B; Zimmermann et al. 2018). The study highlighted functional and anatomical inhomogeneities not only across the retinal surface but the IPL depth. Crucially, systematic distribution of chromatic and colour-opponent responses within distinct layers of the inner retina were broadly congruous with BC-photoreceptor neuroanatomical connectivity, reinforcing the notion that BCs connect to cones in a colour-opponent manner. Downstream RGCs that synapse onto layer-specific BC terminals should inherit a similar physiology (Connaughton and Nelson 2015; Meier et al., 2018), thereby establishing opponent signals to higher visual areas.

Notably, the anisotropic distribution of retinal spectral responses mirrors behaviourally relevant chromatic content in the zebrafish natural habitat. In brief, there is little chromatic information in the visual space directly above the animal, and ventral circuits appear to prioritise achromatic silhouette detection. The mouse utilises a similar strategy, where cone-only dichromacy disappears above the horizon (Baden et al., 2013). In contrast, the horizon

is particularly colour-rich; correspondingly, the retinal visual equator features diverse colour-opponent circuits packed within an inner retinal region almost double in thickness. Of note, dedicated UV-ON circuits heavily dominate the temporoventral retina, or acute zone, likely to support visually-guided prey capture of UV-bright microorganisms in the upper-frontal visual field.

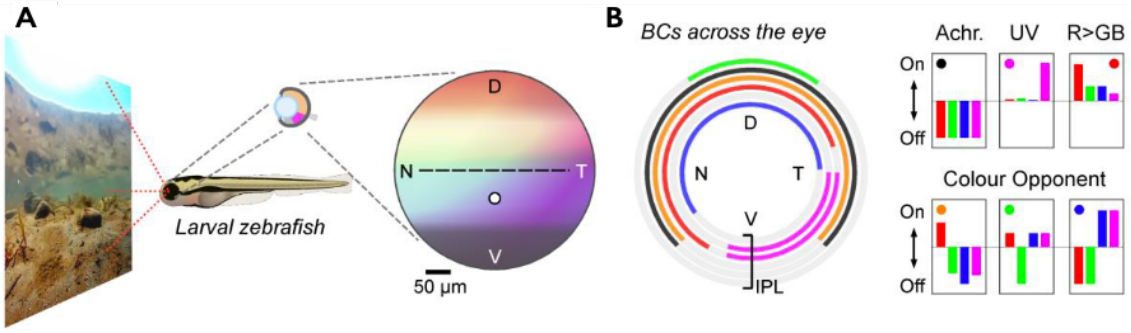

Figure 1.7. | Specialisation of retinal neurons across the eye. A, Each of the four cone-photoreceptor types (Red, Green, Blue and UV) in the larval zebrafish eye are asymmetrically distributed across the retinal surface. **B,** In parallel, there are functional inhomogeneities in bipolar cell terminals across the eye. The bar-graphs highlight the chromatic tuning of six representative functional bipolar cell types, and to the left, their corresponding distribution across the eye. Achromatic circuits are found throughout the eye, differentiated by the dominance of ON and OFF circuits in the upper-frontal- and lower-outward-facing visual fields respectively. In contrast, circuits for tetrachromatic vision – colour and colour-opponent – are largely biased to the horizon and lower visual field, which aligns with the rich chromatic content in the natural habitat. Of note, dedicated monochromatic UV-ON circuits heavily dominate the upper-frontal visual field and may be used for prey capture and the detection of UV-dark silhouettes against a UV-bright backdrop. D, dorsal; T, temporal; V, ventral; N, nasal. Images from Baden et al., 2020.

1.2.7. The zebrafish as a colour circuitry model

Colour vision is key to guiding behaviour in animals, such as navigation in ecological niches, foraging (Church et al., 1998; Potier et al., 2018), mate choice and recognition of conspecifics (Huang et al., 2014; Sabah et al., 2010), as well as prey and predator detection (Dominy and Lucas, 2001), all of which constitute strong evolutionary drives. Given that the larval zebrafish performs tetrachromatic processing and engages in wavelength specific behaviours (Oger and Baier, 2005; Yoshimatsu et al., 2020), it is well suited as an *in vivo* model to probe sensorimotor colour circuits. In particular, there has been extensive work done on prey capture (Antinucci et al., 2019; Bianco et al., 2011; Gahtan et al., 2005; Muto

et al., 2013, 2017; Semmelhack et al., 2014) or predator evasion (Dunn et al., 2016; Preuss et al., 2014; Temizer et al., 2015), and motion perception (Kubo et al., 2014; Naumann et al., 2016). These highly visual behaviours have already been partially characterized in terms of circuitry and could potentially be modulated to include colour vision components. A future direction would be to search for colour-selective receptive fields.

1.3. Thesis aim

To date, there has yet to be a consensus on a definitive classification of RGCs in any species. Crucially, a detailed understanding of the functional complement of zebrafish RGCs and their underlying feature-extracting microcircuits is lacking. Here, I sought to determine the functional output channels of the zebrafish retina, to chart what the fish's eye tells the fish's brain. I first generated a novel transgenic line in which the calcium reporter GCaMP6f is tagged to the membrane of zebrafish RGCs under the Islet2b promoter, allowing recording from both RGC dendrites and somata. Chapter 3 details the *in vivo* population imaging of light-evoked calcium activity of RGCs in the tetrachromatic zebrafish, in response to spectrally defined full-field stimuli. The responses were assigned to functional clusters, and for each cluster, the anatomical distribution across the eye and IPL depth was computed. Recognising that functional characterisation of RGCs with full-field stimuli has its limitations, Chapter 4 details the use of a novel prototype of a tetrachromatic spatial stimulator (Franke et al. 2019) to map receptive fields, to potentially make better sense of more complex contextual effects, such as sensitivity to a certain orientation or direction of motion. While instructive in itself, in reference to existing data from mouse and other species, this will also allow us to study to what extent different species extract different aspects of visual scenes, and how this matches each species' visual requirements.

Chapter 2

Methods

2.1. Experimental model

2.1.1. Animals

All procedures were performed in accordance with the UK Animals (Scientific Procedures) act 1968 and approved by the animal welfare committee of the University of Sussex. Adult animals were housed under a standard 14/10 light/dark cycle and fed 3 times daily. Larvae (~3 mm body length) were grown in E2 solution (1.5 M NaCl, 50 mM KCl, 100 mM MgSO4, 15 mM KH2PO4, 5 mM Na2HPO4) or fish water and treated with 200 μM 1-phenyl-2-thiourea (Sigma, P7629) from 12 hours post fertilization (hpf) to prevent melanogenesis (Karlsson et al., 2001). For 2-photon in-vivo imaging, zebrafish larvae were immobilised in 2% low melting point agarose (Fisher Scientific, BP1360-100), placed on a glass coverslip and submerged in fish water. Eye movements were prevented by injection of α-bungarotoxin (1 nL of 2 mg/ml; Tocris, Cat: 2133) into the ocular muscles behind the eye.

For all experiments, we used 6-8 dpf zebrafish (Danio rerio) larvae (~3 mm body-length). The following previously published transgenic lines were used: Tg(Ptf1a:dsRed) (Jusuf and Harris, 2009), Tg(Islet2b:nls-trpR, tUAS:MGCamp6f) (Janiak et al., 2019) as well as Casper (White et al., 2008), nacre (Thisse et al., 1993) and roy (Ren et al., 2002). In addition, two transgenic lines Tg(Islet2b:nls-trpR, tUAS:SyjRGeco1a) and Tg(tUAS:paGFP) were generated by injecting plasmid solution into one-cell stage embryos. Plasmid solution used are; a mixture of pTol2pA-islet2b-nlsTrpR (Janiak et al., 2019) and pTol2CG2-tUAS-SyjRGeco1a for the Tg(islet2b:nls-trpR, tUAS:SyjRGeco1a) line and pTol2BH-tUAS-paGFP for the Tg(tUAS:paGFP) line. Expression of paGFP was then obtained by crossing these two lines. With this combination, RGCs also express SyjRGeco1a, which was not

used in this study (and which did not interfere with the green channel used for paGFP detection.

Plasmids were constructed by means of a attL/attR (LR)-reaction using destination and entry plasmids as follows; for pTol2CG2-tUAS-SyjRGeco1a; pDestTol2CG2 (Kwan et al., 2007), p5E-tUAS(Suli et al., 2014), pME-SyjRGeco1a, p3E-pA(Kwan et al., 2007), for pTol2BH-tUAS-paGFP; pDestTol2BH[27], p5E-tUAS, pME-paGFP, p3E-pA. pME-SyjRGeco1a was constructed by inserting PCR amplified zebrafish synaptophysin without stop codon (Dreosti et al., 2009) followed by PCR amplified jRGeco1a fragment (Dana et al., 2016) into pME plasmid. Similarly, pME-paGFP was constructed by inserting PCR amplified paGFP fragment into pME plasmid.

For transient expression of mGCaMP6f under Islet2b we injected a mixture of pTol2pA-islet2b-nlsTrpR and pTol2BH-tUAS-MGCamp6f plasmids (Janiak et al., 2019) solution into one-cell stage eggs. Positive embryos were screened under 2-photon.

2.2. Method details

2.2.1. Tissue preparation, immunolabeling, and imaging

For immunohistochemistry, larvae were euthanised by tricaine overdose (800 mg/l) and fixed in 4% paraformaldehyde in phosphate-buffered saline (PBS) for 30 minutes at room temperature before being washed in calcium-negative PBS. Retinae were then incubated in permeabilization/blocking buffer (PBS with 0.5% Triton X-100 and 5% normal donkey serum) at 4°C for 24 hours, and thereafter transferred to the appropriate labelling solution. For nuclear labelling, tissue was incubated at 4°C in blocking solution with Hoechst 33342 nuclear dye (Invitrogen, H21492, 1:2000) for 24 hours. For membrane staining, tissue was incubated at 4°C in blocking solution with BODIPY membrane dye (Invitrogen, C34556, 1:1000) for 24 hours. For immunostaining, tissue was incubated at 4°C for 72 hours in

primary antibody solution (chicken anti-GFP (AbCam, 13970, 1:500), rabbit anti-cox iv (AbCam, 16056, 1:500), diluted in permeabilization/blocking solution). Samples were rinsed three times in PBS with 0.5% Triton X-100, then transferred to secondary antibody solution (donkey anti-chicken IgG CF488A conjugate (Sigma, SAB4600031, 1:500), donkey anti-rabbit IgG CF568 conjugate (Sigma, SAB4600076, 1:500)), diluted in permeabilization/blocking solution and incubated at 4˚C for 24 hours. Finally, samples were rinsed three times in PBS with 0.5% Triton X-100 before being mounted in mounting media (VectaShield, Vector, H-1000) for confocal imaging.

GABA immunostaining was performed using rabbit anti-GABA (Sigma, A2052, 1:500) according to the protocol described in (Jusuf and Harris, 2009). Briefly, whole retinas were fixed in 2% PFA /2% glutaraldehyde for 24 hours at 4˚C, rinsed in PBS, treated with 0.1% sodium borohydride (NaBH4) in 0.2% Triton X-100 in PBS for 10 minutes at room temperature, and rinsed again to remove excess NaBH4. For immunolabeling, all steps are as described above, with the following exceptions: blocking buffer consisted of 10% normal donkey serum, 0.1% Tween-20, and 0.5% Triton X-100 in PBS; primary and secondary antibodies were also diluted in this blocking buffer.

Confocal stacks and individual images were taken on Leica TCS SP8 using 40x water-immersion objective at xy resolution of 2,048x2,048 pixels (pixel width: 0.162 μm). Voxel depth of stacks was taken at z-step 0.3-0.5 μm. Contrast and brightness were adjusted in Fiji (NIH).

2.2.2. Cell density mapping

The 3D positions of all GCL somata (stained with Hoecht 3342), as well as dAC and AC somata (tg(Ptf1a:dsRed), and MG tg(GFAP:GFP), immunolabeled against GFP) were semi-automatically detected in Fiji from confocal image stacks of intact, whole eyes. These

positions were then projected into a local-distance preserving 2D map as shown previously (Zimmermann et al., 2018) using custom-written scripts in Igor Pro 6.37 (Wavemetrics). The density map of RGC somata was computed by subtracting the density map of dACs from that of GCL cells. Similarly, the density map of ACs was computed by summing the density maps of dACs and ACs from the inner nuclear layer. From here, RGC maps were also mapped into a sinusoidal projection of visual space (Yoshimatsu et al., 2019a).

2.2.3. Axonal tracing

The lipophilic tracer dye DiO (Invitrogen, D307) was used to trace RGC axons from the retina to their arborization fields in the pretectum and tectum. 1 mg/mL stock solution was prepared in dimethylformamide and stored at -20˚C. For injection into Tg(Islet2b:nls-trpR, tUAS:MGCamp6f) retinas, the lenses of whole fixed larvae were removed and a sufficient amount of tracer dye injected into one of either the left or the right eye so as to completely cover the exposed surface of the GCL. Tissue was then incubated at 37˚C for 3 days to allow the dye time to diffuse all the way up RGC axons to their terminals in the midbrain.

2.2.4. Two-photon functional imaging and stimulation parameters

For all in vivo imaging experiments, we used a MOM-type two-photon microscope (designed by W. Denk, MPI, Martinsried (Euler et al., 2013); purchased through Sutter Instruments/Science Projects) equipped with the following: a mode-locked Ti:Sapphire laser (Chameleon Vision-S, Coherent) tuned to 927 nm for imaging GFP and 960 nm for imaging mCherry/BODIPY in combination with GFP; two fluorescent detection channels for GFP (F48x573, AHF/Chroma) and mCherry/BODIPY (F39x628, AHF/Chroma), and; a water-immersion objective (W Plan-Apochromat 20x/1,0 DIC M27, Zeiss). For

image acquisition, we used custom-written software (ScanM, by M. Mueller, MPI, Martinsried and T Euler, CIN, Tübingen) running under Igor Pro 6.37 (Wavemetrics). Structural data was recorded at 512x512 pixels, while functional data was recorded at 64x32 pixel resolution (15.6 Hz, 2 ms line speed) or 128x64 pixel resolution (15.6 Hz, 1ms line speed). For each functional scan, we first defined a curvature of the imaged IPL segment based on a structural scan, and thereafter "bent" the scan plane accordingly ("banana scan"). This ensured that the imaging laser spent a majority of time sampling from the curved IPL and INL, rather than adjacent dead space. The banana-scan function was custom-written under ScanM.

For light stimulation, we focused a custom-built stimulator through the objective, fitted with band-pass-filtered light-emitting diodes (LEDs) ('red' 588nm, B5B-434-TY, 13.5 cd, 8°; 'green' 477 nm, RLS-5B475-S, 3-4cd, 15°, 20 mA; 'blue' 415 nm, VL415-5-15, 10-16 mW, 15°, 20 mA; 'ultraviolet' 365 nm, LED365-06Z, 5.5 mW, 4°, 20 mA; Roithner, Germany). LEDs were filtered and combined using FF01-370/36, T450/pxr, ET420/40 m, T400LP, ET480/40x, H560LPXR (AHF/Chroma). The final spectra approximated the peak spectral sensitivity of zebrafish R-, G-, B-, and UV-opsins, respectively, while avoiding the microscope's two detection bands for GFP and mCherry/BODIPY. To prevent interference of the stimulation light with the optical recording, LEDs were synchronized with the scan retrace at 500Hz (2 ms line duration) using a microcontroller and custom scripts. Further information on the stimulator, including all files and detailed build instructions can be found at (Zimmermann et al., 2020).

Stimulator intensity was calibrated (in photons per second per cone) such that each LED would stimulate its respective zebrafish cone type with a number of photons adjusted to follow the relative power distribution of the four wavelength peaks of daytime light in the

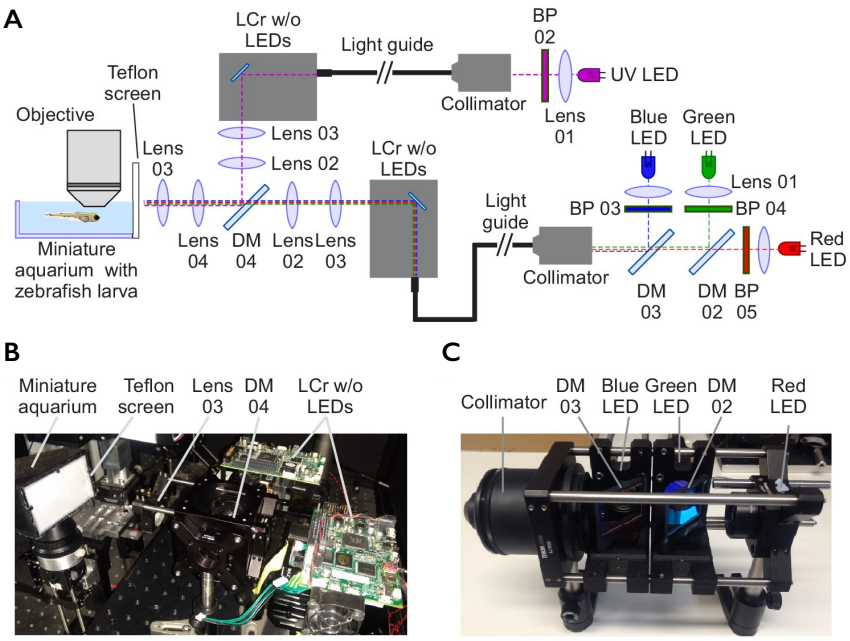

Figure 2.1. | **Visual stimulator design. A,** Schematic drawing of the tetrachromatic stimulator for in vivo recordings in zebrafish larvae. The optical pathways of two lightcrafters (LCr) are combined and the stimulus projected onto a UV-transmissive Teflon screen at one side of the miniature aquarium. **B,** Side-view of tetrachromatic stimulation setup. **C,** RGB external LED illumination unit of tetrachromatic stimulation setup.

zebrafish natural habitat (Nevala and Baden, 2019; Zimmermann et al., 2018) to yield 'natural white': red, "100%" (34x105 photons /s /cone); green, "50%" (18 x105 photons /s /cone); blue, "13%" (4.7 x105 photons /s /cone); ultraviolet, "6%" (2.1x105 photons /s /cone). We did not compensate for cross-activation of other cones. Owing to 2-photon excitation of photopigments, an additional constant background illumination of ~104 R* was present throughout (Baden et al., 2013; Euler et al., 2009, 2019). For all experiments, larvae were kept at constant illumination for at least 2 seconds after the laser scanning started before light stimuli were presented. Two types of full-field stimuli were used: a binary dense "natural spectrum" white noise, in which the four LEDs were flickered independently in a known random binary sequence at 6.4 Hz for 258 seconds, and a natural-white chirp stimulus (Baden et al., 2016) where all four LEDs were driven together. To prevent interference of the stimulation light with the optical recording, LEDs were synchronised to the scanner's retrace (Euler et al., 2019).

2.3. Data analysis

Data analysis was performed using IGOR Pro 6.3 (Wavemetrics), Fiji (NIH) and Matlab R2018b (Mathworks).

2.3.1. ROI placements and quality criterion

ROIs were automatically placed using local image correlation based on established protocols – for details see (Franke et al., 2017). To allocate ROIs to dendritic and somatic datasets a boundary between the GCL and IPL was drawn by hand in each scan - all ROIs with a centre of mass above the boundary were considered as dendritic, and all ROIs below were considered as somatic. Since the lower part of the IPL tends to be dominated by On-circuits, it is possible that a small number of On-dendrites were incorrectly classed as somata which may go part-way to explaining the generally stronger On-bias amongst somatic compared to dendritic ROIs (cf. Fig. 3.2A). Moreover, due to the ring-like nature of mGCaMP6f expression profiles in somata when optically sectioned, it was possible that two ROIs could be inadvertently placed on different halves of the same soma. However, since whether or not a soma was split in this way was likely non-systematic over functional types, we did not attempt to correct for this possibility. Only ROIs where at least one of the four spectral kernels' peak-to-peak amplitudes exceeded a minimum of ten standard deviations were kept for further analysis (n = 2,414/2,851 dendritic ROIs, 84.7%; 411/796 somatic ROIs, 51.6%). Equally, all individual colour kernels that did not exceed 10 SDs were discarded (i.e., set to NaN).

2.3.2. Kernel polarity

The use of a fluorescence-response-triggered average stimulus (here: 'kernel') as a shorthand for a neuron's stimulus-response properties, while potentially powerful (e.g. (Franke et al.,

2017; Szatko et al., 2019; Zimmermann et al., 2018)), ought to be considered with some caution. For example, determining a binary value for a kernel's polarity (On or Off) can be conflicted with the fact that a neuron might exhibit both On and Off response aspects. Moreover, different possible measures of On or Off dominance in a kernel can generate different classification biases. Here, we defined On and Off based on a measure of a kernel's dominant trajectory in time. For this, we determined the position in time of each kernel's maximum and minimum. If the maximum preceded the minimum, the kernel was classified as Off, while vice versa if the minimum preceded the maximum, the kernel was defined as On. Examples On and Off kernels classified in this way can for example be seen in Fig. 3.3B (cf. Fig. 3.3A central horizontal column for a lookup of how each kernel was classified).

2.3.3. Functional data pre-processing and receptive field mapping

Regions of interest (ROIs), corresponding to dendritic or somatic segments of RGCs were defined automatically as shown previously based on local image correlation over time (Franke et al., 2017). Next, the Ca2+ traces for each ROI were extracted and de-trended by high-pass filtering above ~0.1 Hz and followed by z-normalisation based on the time interval 1-6 seconds at the beginning of recordings using custom-written routines under IGOR Pro. A stimulus time marker embedded in the recording data served to align the Ca^{2+} traces relative to the visual stimulus with a temporal precision of 1 ms. Responses to the chirp stimulus were up-sampled to 1 KHz and averaged over 3-6 trials. For data from tetrachromatic noise stimulation we mapped linear receptive fields of each ROI by computing the Ca^{2+} transient-triggered-average. To this end, we resampled the time-derivative of each trace to match the stimulus-alignment rate of 500 Hz and used thresholding above 0.7 standard deviations relative to the baseline noise to the times t_i at

which Calcium transients occurred. We then computed the Ca^{2+} transient-triggered average stimulus, weighting each sample by the steepness of the transient:

$$\boldsymbol{F}(l,\tau) = \frac{1}{M}\sum_{i=1}^{M} \dot{\boldsymbol{c}}(t_i)\boldsymbol{S}(o, t_i + \tau)$$

Here, $\boldsymbol{S}(l,t)$ is the stimulus ("LED" and "time"), τ is the time lag (ranging from approx. -1,000 to 350 ms) and M is the number of Ca^{2+} events. RFs are shown in *z*-scores for each LED, normalised to the first 50 ms of the time-lag. To select ROIs with a non-random temporal kernel, we used all ROIs with a standard deviation of at least ten in at least one of the four spectral kernels. The precise choice of this quality criterion does not have a major effect on the results.

2.3.4. Eye-IPL maps

To summarise average functions of RGC processes across different positions in the eye and across IPL depths, we computed two-dimensional "Eye-IPL" maps. For this, we divided position in the eye (-π:π radians) into eight equal bins of width π/4. Similarly, we divided the IPL into 20 bins. All soma ROIs were allocated to bin 1 independent of their depth in the GCL. while all IPL ROIs were distributed to bins 3:20 based on their relative position between the IPL boundaries. As such, bin 2 is always empty, and serves as a visual barrier between IPL and GCL. From here, the responses of ROIs within each bin were averaged. All maps were in addition smoothed using a circular π/3 binomial (Gaussian) filter along eye-position, as well as for 5% of IPL depth across the y-dimension (dendritic bins 3:20 only).

2.3.5. On-Off index (OOi)

For each Eye-IPL bin, an On-Off index (OOi) was computed:

$$OOi = \frac{nOn - nOff}{nOn + n\,Off}$$

Where nOn and nOff correspond to the number of On and Off kernels in a bin, respectively. OOi ranged from 1 (all kernels On) to -1 (all kernels Off), with and OOi of zero denoting a bin where the number of On and Off kernels was equal.

2.3.6. Ternary response classification

Each ROI was allocated to one of 81 ternary response bins (three response states raised to the power of four spectral bands). One of three response-states was determined for each of four spectral kernels (red, green, blue, UV) belonging to the same ROI: On, Off or non-responding. All kernels with a peak-to-peak amplitude below ten standard deviations were considered non-responding, while the remainder was classified as either On or Off based on the sign of the largest transition in the kernel (upwards: On, downwards: Off).

2.3.7. Feature extraction and clustering

Clustering was performed on four data sets, each containing the functional responses of RGCs to chirp stimuli and kernels derived from colour noise stimuli: 1) pan retinal inner plexiform layer (PR-IPL) data set (n = 2,851), sampling RGC dendritic responses at all eccentricities and across a range of depths in the IPL; 2) strike zone inner plexiform layer (SZ-IPL) data set (n = 3,542), sampling RGCs at the SZ only and across the IPL; 3) pan retinal ganglion cell layer (PR-GCL) data set (n = 796), sampling RGC responses at all eccentricities from the RGC somata in the GCL; and 4) strike zone ganglion cell layer (SZ-GCL) data set (n = 1,694), sampling RGCs at the SZ only from the RGC somata. Mean responses to chirp stimuli were formatted as 2,499 time points (dt = 1 ms) while colour kernels were formatted as 649 time points (dt = 2 ms, starting at t = -0.9735 s) per spectral channel (red, green, blue and UV).

For each dataset we clustered using only the kernels portion of the data since this was found to produce a cleaner clustering than when clustering chirp responses and kernels together, or chirp responses alone. ROIs with low quality kernels, determined as the maximum standard deviation across the four colours, were identified and removed from the data set. For clustering, a kernel quality threshold of 5 was chosen, such that any ROI with a kernel quality below this threshold was eliminated from the data to be clustered.

Following quality control, the data sets had the following sizes: 1) PR-IPL: n = 2,414 (84.7% of original); 2) SZ-IPL: n = 2,435 (68.8% of original); 3) PR-GCL: n = 411 (51.6% of original); 4) SZ-GCL: n = 721 (42.6 % of original).

We scaled the data corresponding to each kernel colour by dividing each one by the standard deviation through time and across ROIs. In this way we ensured an even weighting for each colour. This is important, since the red and green kernels tended to have larger amplitudes than the blue and UV kernels.

We used principal component analysis (PCA) to reduce the dimensions of the problem prior to clustering. PCA was performed using the Matlab routine pca (default settings). We applied PCA to the portions of a data set corresponding to each of the kernel colours separately, retaining the minimum number of principal components necessary to explain ≥99% of the variance. The resulting four 'scores' matrices were then concatenated into a single matrix ready for clustering. The following numbers of principal components were used for each of the data sets: 1) PR-IPL: 8 red (R) components, 8 green (G) components, 13 blue (B) components, 33 ultraviolet (UV) components (62 in total); and 2) PR-GCL: 13 R, 11 G, 24 B, 36 UV (84 in total).

We clustered the combined 'scores' matrix using Gaussian Mixture Model (GMM) clustering, performed using the Matlab routine **fitgmdist**. We clustered the data into

clusters of sizes 1,2,...,100, using i) shared-diagonal, ii) unshared-diagonal, iii) shared-full and iv) unshared-full covariance matrices, such that (100*4 =) 400 different clustering options were explored in total. For each clustering option 20 replicates were calculated (each with a different set of initial values) and the replicate with the largest loglikelihood chosen. A regularisation value of 10-5 was chosen to ensure that the estimated covariance matrices were positive definite, while the maximum number of iterations was set at 104. All other **fitgmdist** settings were set to their default values.

In data set PR-IPL the optimum clustering was judged to be that which minimised the Bayesian information criterion (BIC), which balances the explanatory power of the model (loglikelihood) with model complexity (number of parameters), while clusters with <10 members were removed. In data set PR-GCL the BIC did not give a clean clustering; therefore, we specified 20 clusters for the PR-GCL, with unshared-diagonal covariance matrices, removing clusters with <5 members.

Using the above procedure, we obtained the following optimum number of clusters for each data set: 1. PR-IPL: 15 clusters (2 clusters with <10 members removed); 2. PR-GCL: 13 clusters (7 clusters with <5 members removed). Unshared-diagonal covariance matrices gave the optimal solution in all cases.

Chapter 3

Zebrafish retinal ganglion cells asymmetrically encode spectral and temporal information across visual space

3.1. Introduction

In vertebrate vision, the axons of retinal ganglion cells (RGCs) are tasked with transmitting information from the eye to the brain (Masland, 2012a; Wässle, 2004). Despite well-researched links between zebrafish brain circuits and output visual behaviours, comparatively little is known about the front end of the visual system. Major gaps in knowledge include information on spectral coding, and crucially, data on potentially key variations in RGC properties across the retinal surface, in line with asymmetric statistics of natural visual space and species-specific ethological needs.

Classically, RGC types are thought to encode feature-specific information such as colour, speed, orientation or direction of a moving edge. However, the exact nature of encoded output from the eye (Baden et al., 2016; Vlasits et al., 2019), and to what extent the mosaics of RGC types are indeed homogenous to meet species-specific visuo-ecological demands (Bleckert et al., 2014; Chang et al., 2013; Sabbah et al., 2017; Sinha et al., 2017; Szatko et al., 2019; Warwick et al., 2018) are largely unknown (Baden et al., 2020). Moreover, directly attributing specific ethological behaviours to select RGC types remains mostly speculative (Baden et al., 2020; Lettvin et al., 1959).

Here, the larval zebrafish offer a powerful tool to dissect the workings of retinal circuits *in vivo* (Bollmann, 2019). Their genetic amenability and optical accessibility enable real-time imaging of visual circuits as the intact awake animal perform visually-driven behaviours such as prey capture (Antinucci et al., 2019; Muto et al., 2013, 2017; Semmelhack et al., 2014) or predator evasion (Dunn et al., 2016; Preuss et al., 2014; Temizer et al., 2015). Notably, Antinucci et al. (2019) demonstrated that prey-capture-like behaviours can be elicited by optogenetic activation of single neurons in a retinorecipient nucleus of the brain.

Given the repertoire of visual behaviours, how do RGC signals emerging from the eye instruct these downstream circuits?

Optical imaging of RGC axon terminals in the brain suggest that like in mammals (Baden et al., 2018), larval zebrafish RGCs are tuned to object size (Preuss et al., 2014) in addition to orientation and motion direction (Nikolaou et al., 2012). Crucially, RGC types show distinct axonal projection patterns to target retinorecipient brain regions or arborisation fields, AF1-10 (Robles et al., 2014) – AF10 being the optic tectum, the teleost homologue of the mammalian superior colliculus (Burrill and Easter, 1994). Further, their arborisations target specific laminae of the tectal neuropil (Gabriel et al., 2012; Lowe et al., 2013; Nikolaou et al., 2012; Semmelhack et al., 2014). Through anatomical, functional and behavioural approaches, complementary studies to characterise RGCs build toward our current incomplete understanding of RGC structure and function in the zebrafish.

To address ethological needs, we first consider the zebrafish's large field of view which enables the animal to simultaneously survey the overhead sky and riverbed beneath (Bianco et al., 2011; Patterson et al., 2013; Zimmermann et al., 2018). These divided areas of visual space have vastly different behavioural relevance, in addition to distinct spatial, temporal and spectral statistics (Baden et al., 2020; Engeszer et al., 2007; Nevala and Baden, 2019; Parichy, 2015; Zimmermann et al., 2018). Accordingly, both photoreceptor (Yoshimatsu et al., 2020) and bipolar cell functions (Zimmermann et al., 2018) are asymmetrically distributed across the retina, and feature prominent reorganisation in the *area temporalis*, a region identified for visual prey capture (Bianco et al., 2011; McElligott and O'Malley, 2005; Mearns et al., 2020; Patterson et al., 2013; Semmelhack et al., 2014; Trivedi and Bollmann, 2013; Yoshimatsu et al., 2020; Zimmermann et al., 2018). In contrast, data on functional retinal anisotropies in larval zebrafish RGCs is lacking (but see [Robles et al.,

2014]). Similarly, to optimise efficient coding (Attneave, 1954; Barlow, 1961; Simoncelli and Olshausen, 2001), the zebrafish should invest in dedicated sets of functional RGC types to support various aspects of vision across their retinal surface.

Next, a major challenge of optically characterising RGC functions is reliably recording discrete signals from their densely packed axonal arborisations in the brain (Nikolaou et al., 2012). Further, RGC axons are potentially subject to central presynaptic inputs (Ferguson and McFarlane, 2002; Liang et al., 2020; Sajovic and Levinthal, 1983), adding to the difficulty of determining which aspects of their response properties originate in the eye, and which emerge only later in the brain.

Finally, long-wavelength light stimulation is routinely used in the functional imaging of zebrafish visual circuits to limit interference with fluorescence imaging systems (Bollmann, 2019), which do not fully inform given that zebrafish have spectrally diverse retinal circuits (Connaughton and Nelson, 2010; Klaassen et al., 2016; Meier et al., 2018; Zimmermann et al., 2018) to support tetrachromatic colour vision (Meier et al., 2018). Wavelength is strongly linked to specific behaviours in zebrafish; in particular, the optomotor response (OMR) is driven by long-wavelength light (Krauss and Neumeyer, 2003; Orger and Baier, 2005), conversely prey-capture circuits are reliant on short-wavelength (Yoshimatsu et al., 2020). Crucially, data on how spectrally selective RGC circuits drive zebrafish visual behaviours is lacking.

To address these significant gaps in knowledge, we systematically recorded light-driven signals from RGCs in the *in vivo* eye using two-photon imaging. By 'bending' the imaging scan-plane to align with the natural curvature of the eye (Janiak et al., 2019), and synchronising the stimulation light with the scanner retrace (Baden et al., 2013; Euler et

al., 2009, 2019; Franke et al., 2019; Zimmermann et al., 2018), we chart the *in vivo* functional diversity of larval zebrafish RGCs in time and wavelength across visual space. We find the functional properties of zebrafish RGCs to be highly position dependent to support a broad range of both achromatic and chromatic functions. Remarkably, approximately half of RGC processes display complex forms of colour opponency, challenging classical models of colour vision. Strikingly, much spectral opponency is driven by a prevalent slow blue-Off system. Of note, we find a regional prominence of UV-sensitive On-sustained circuits in the acute zone, potentially to support visual prey capture of UV-bright zooplankton. Finally, there appears to be a notable interdependence of temporal and spectral signal processing. Taken together, our results suggest that zebrafish RGCs send a diverse and highly regionalised time-colour code to the brain.

3.2. Results

3.2.1. Highly diverse light-driven RGC responses in the in vivo eye

To record light-driven activity from RGC processes in the eye, we expressed a membrane-tagged variant of GCaMP6f (mGCaMP6f) under the RGC-associated promoter Islet2b (Pittman et al., 2008), which reliably labelled most RGCs (Fig. 3.1A, Suppl. Fig. S1A-C; Methods). For stimulation, we presented full-field light modulated in time and wavelength using four LEDs spectrally aligned with the sensitivity peaks of the zebrafish's four cone opsins (R, G, B, UV; Zimmermann et al., 2018). The power of each LED was tuned to the relative power distribution across wavelength of daytime light in the zebrafish natural habitat (Nevala and Baden, 2019; Zimmermann et al., 2018) to yield a 'natural white': red (100%), green (50%), blue (13%) and UV (6%; Fig. 3.1B). This calibration was to ensure that the spectral responses of RGCs reflect their likely performance in a natural setting. Of note, separate tests using high-UV power during noise stimulation showed that although

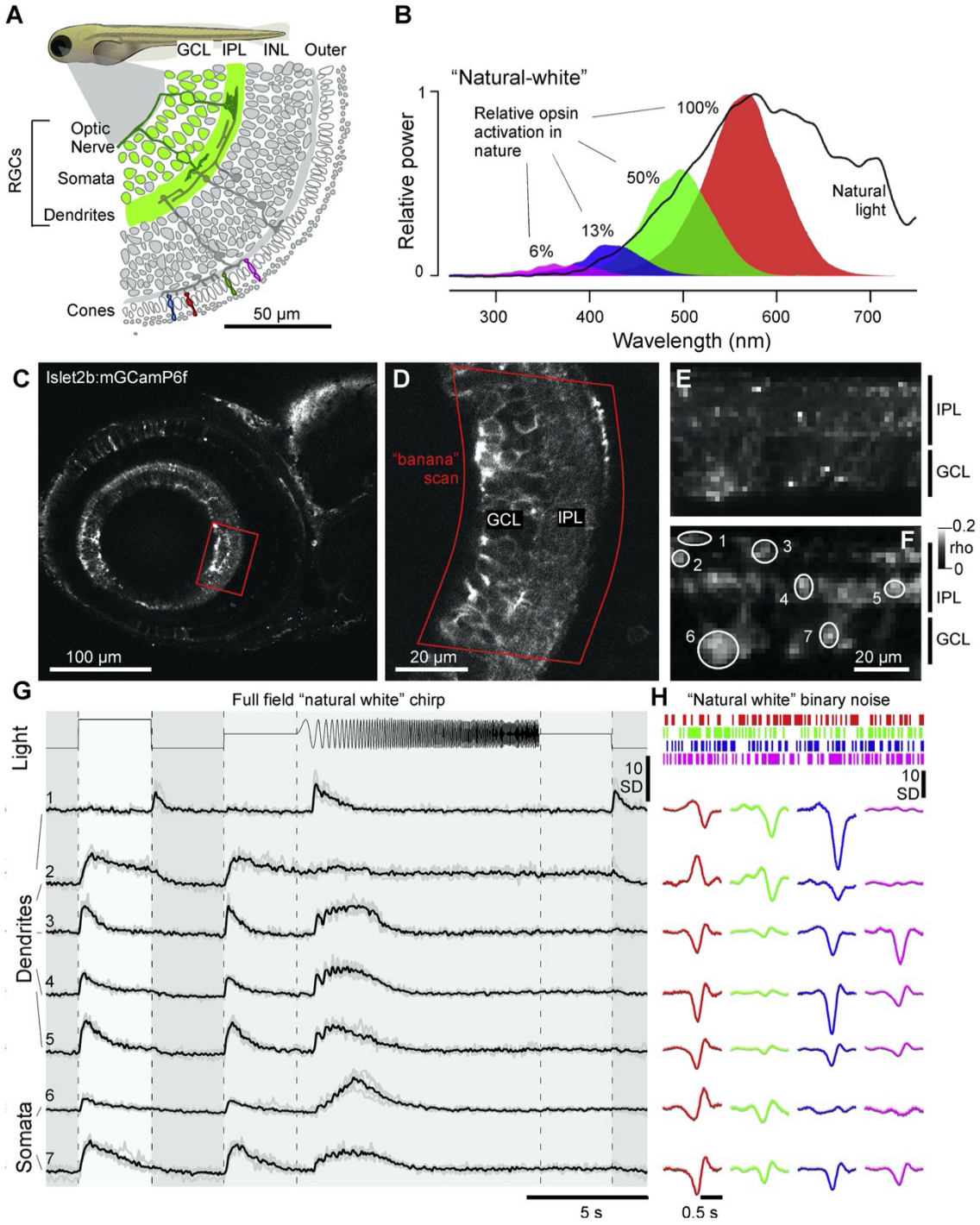

Figure 3.1. | **Recording from RGC dendrites and somata *in vivo*. A,** Schematic of Islet2b:mGCaMP6f expression in RGCs (green) across a section of the larval zebrafish eye, with somata in the ganglion cell layer (GCL) and dendrites in the inner plexiform layer (IPL); see also Suppl. Fig. S1A–C. INL, Inner nuclear layer. **B,** Average spectrum of natural daylight measured in the zebrafish natural habitat from the fish's point of view along the underwater horizon (solid line). Convolution of the zebrafish's four cone action spectra with this average spectrum (shadings) was used to estimate the relative power each cone surveys in nature, normalised to red cones (100%). Stimulation LED powers were adjusted accordingly relative to red ('natural white'). **C,D,** mGCaMP6f expression under two-photon surveyed across the eye's sagittal plane (C), and zoomed-in to the acute zone as indicated (D). Within the zoomed field of view, a curved scan path was defined ('banana scan') to align with the curved GCL and IPL for activity recordings (E), effectively 'straightening' the natural curvature of the eye. **E,F,** Example activity scan with RGC dendrites in the IPL occupying the top part of the scan, and somata in the GCL occupying the bottom part as indicated (E); and correlation projection (Franke et al., 2017) of activity highlighting responding regions in the scan following white noise stimulation, alongside example

regions of interest (ROIs; F; see also Suppl. Video S1). **G,** Mean (black) example responses of ROIs from (E), and individual repeats (grey), to full-field stimulation as indicated. **H,** As (G), now showing linear kernels to red, green, blue, and UV components recovered from natural white noise stimulation (Methods). Note that several ROIs display a robust UV component despite the ~20-fold attenuated stimulation power relative to red (B; see also Suppl. Fig. S1D–G).

high intensity UV altered the overall waveforms of RGC responses, there was remarkably no significant difference in the amplitudes and distributions of spectral receptive fields (Suppl. Fig. S1D-G).

Animals were imaged under two-photon at 6-8 days post fertilisation (dpf). Recordings were performed in the eye's sagittal plane (Fig. 3.1C). By 'bending' each scan-plane to align with the natural curvature of the eye (Fig. 3.1D, 'banana scan'; Methods), it allowed capturing both the inner plexiform layer (IPL) and adjacent ganglion cell layer (GCL) while minimising surrounding dead space (Fig. 3.1E); in addition the 'straightened' scans facilitated analyses (Methods): an example 15.6 Hz recording at 64x32 pixel resolution illustrates a 'straightened' IPL (upper) and GCL (lower) (Fig. 3.1E,F; Suppl. Video S1). Together, this enabled sampling both RGC dendrites in the IPL, which integrate inputs from bipolar cells (BCs) and amacrine cells (ACs; Baden et al., 2018), and RGC somata in the GCL, whose activity is expected to largely reflect the spiking activity for transmission to the brain (Baden et al., 2016; Methods). Throughout, we present data recorded from these distinct structures together (Fig. 3.1G,H), with summary panels showing dendrites plotted on top and somata on an inverted y-axis below (Fig. 3.2A,B). Of note, with additional single cell recordings (Suppl. Fig. S2A-E), we substantiated that the types and distributions of dendritic and somatic functions tended to be largely consistent with each other, with exceptions noted below.

For each scan, we presented two stimuli: A 'natural-white' time varying chirp stimulus (Baden et al., 2016) to probe achromatic response properties, and a 6.4 Hz natural-power

spectrum tetrachromatic binary noise stimulus to assess spectral tuning (Zimmermann et al., 2018). For the latter, four linear kernels were computed from reverse correlation of the response of each region of interest (ROI), one for each stimulated waveband (Methods).

In an example recording, a selection of ROIs revealed a rich diversity of response properties across both RGC dendrites and somata (Fig. 3.1G,H). As observed, dendritic ROI 1 was a blue-dominant transient Off-process, while immediately adjacent ROI 2 was a 'red versus green/blue' colour opponent sustained On-process. Similarly, RGC somata displayed varied responses; ROI 6 had a red-biased transient On response and band-pass frequency tuning, while ROI 7 was a largely achromatic On cell. We next systematically recorded RGC responses to these stimuli at different positions across the eye.

3.2.2. RGC polarities and spectral response properties vary across visual space

In total, we recorded 72 such fields of view (n = 17 fish), and automatically placed ROIs on functionally homogeneous processes based on local response correlation during presentation of the tetrachromatic noise stimulus (Franke et al., 2017; Suppl. Fig. S1H-J; Methods). Based on its vertical position in the scan field, each ROI was assigned as representing either dendrite or soma. This resulted in 2,851 dendritic and 796 somatic ROIs, of which 2,414 (84.7%) and 411 (51.6%) respectively, passed our response quality criterion (Methods). ROIs from the acute zone were comparatively overrepresented (Suppl. Fig. S2F), consistent with retinal thickening in this region of the eye (Schmitt and Dowling, 1999; Zimmermann et al., 2018).

From here, low-amplitude ROIs were discarded (Methods) and final ROIs classed as either dominant 'On' or 'Off' based on the dominant polarity of their largest amplitude kernel (Fig. 3.2A, Methods). Under this criteria, dendritic ROIs were approximately evenly (54:46 On:Off) divided into On and Off groups (n = 1,461 On, 1,255 Off), while somata

comprised relatively more On ROIs (66:34 On:Off; n = 388 On, 198 Off). Similarly, when considering only red or green kernels individually, On dominated at the level of somata (red: 65% On: n=378 On, 208 Off; green 85% On: n = 416 On, 70 Off) but not dendrites (red: 47% On: n = 1,291 On, 1,452 Off; green: 43% On: n = 1,164 On, 1,552 Off; Suppl. Fig. S2G). In contrast, both at the level of somata and dendrites, blue kernels were heavily Off-biased (somata: 67% Off: n = 196 On, 390 Off; dendrites: 73% Off: n = 732 On, 1,984 Off), while UV somatic, but not dendritic, kernels were On-biased (somata: 64% On: n = 378 On, 211 Off; dendrites: 44% On: n = 1,192 On, 1,542 Off; Suppl. Fig. S2H).

Next, we evaluated how On- and Off-type responses in each spectral waveband varied throughout the eye and therefore, corresponding position across visual space (Fig. 3.2B). For both dendrites and somata, consistent with our previous findings in bipolar cells (Zimmermann et al., 2018), On- and Off-processes were generally biased to the upper and lower visual fields, respectively. Blue-responsive RGC processes were the exception; strikingly, blue-Off dominated over blue-On processes throughout visual space. Also of note, both On and Off UV-dendritic processes largely surveyed the upper visual field, with one difference – UV-On processes were heavily biased to the frontal-upper visual field whereas UV-Off processes generally evenly surveyed the upper visual space without any obvious preference. Notably, unlike the major eye-wide trends observed above, the highly asymmetrical distribution of dendritic UV signals was only approximately reflected at the level of somata. To what extent dendrite-soma variation can be explained by putative type-specific diversity in somatic calcium channels and/or actual differences between these distinct cellular compartments remains unclear (Methods). This is further confounded by the difficulty in reliably recording calcium signals from the soma, likely due to a lack of

calcium channels, thereby limiting calcium flux. We next asked how these spectral and regional differences are established within the layers of the IPL.

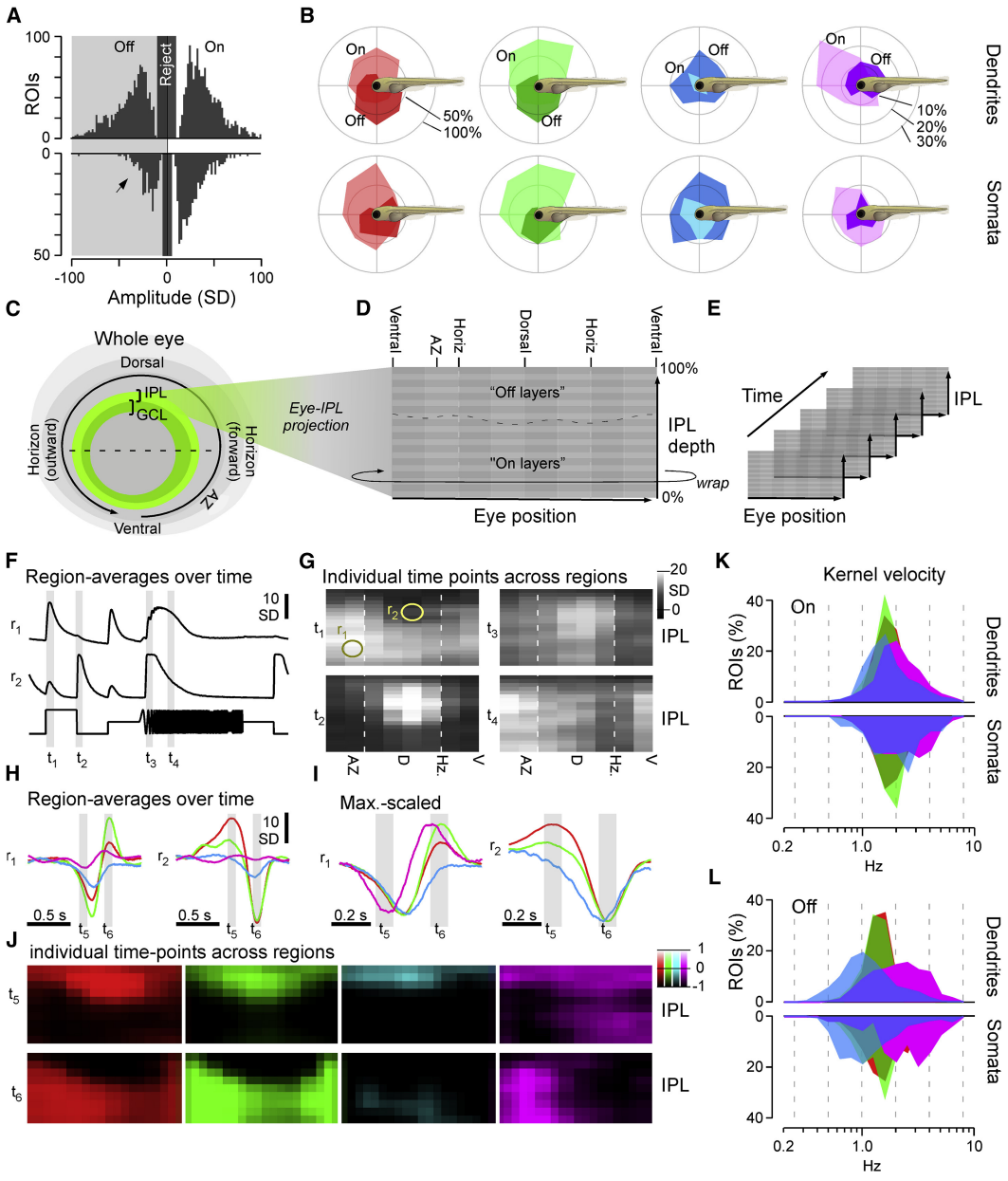

Figure 3.2. | **Major functional response trends across the eye. A,** Kernel amplitudes of all dendritic (top) and somatic (bottom; y-flipped) ROIs, shown for the maximal amplitude kernel of each ROI irrespective of colour. For a breakdown by colour, see Suppl. Fig. S2G,H. The arrowhead highlights a relative reduction in Off-responses at the level of somata. Chi-square with Yates correction for On:Off distribution dendrites vs. somata: $p < 0.00001$. **B,** Prominence of different colour and polarity responses among dendrites (top row) and somata (bottom row), plotted across visual space. All kernels that exceeded a minimum amplitude of 10 SDs were included. Scale bars in percent of dendritic/somatic ROIs that were recorded in a given section of the eye such that the percentages of On, Off, and non-responding (<10 SD) add to 100% are shown. **C-E,** Schematic illustrating how dendritic ROIs from different regions of the eye and IPL depth (C) were mapped onto a 2D 'Eye-IPL' map (D), which can subsequently be analysed over experimental time (E). Note that this involved 'cutting' the circular range of eye positions such that the ventral retina is represented at either edge

along the x axis. **F,G,** Example mean responses to chirp stimulation (cf. Fig. 3.1G) mapped onto an Eye-IPL map as schematized above (C–E). Data can be plotted as time traces for a given region of the eye and IPL (F; $r_{1,2}$ as indicated in G) or alternatively as a time-frozen snapshot of activity across the eye and IPL at specific points in time (G; $t_{1–4}$ as indicated in F). See also Suppl. Videos S2, S3. **H-J,** As (F) and (G) but instead showing mean kernels across the four spectral wavebands, where (H) and (I) are mean and max-scaled mean kernels for Eye-IPL regions $r_{1,2}$ (as in F) respectively. (J) shows each kernel's full Eye-IPL map at two time points $t_{5,6}$ as indicated in (H) and (I) (see also Suppl. Fig. S2I). In the colour scale bar, 0 equates to the baseline of each bin's kernel and 1/−1 their respective maximum or minimum (cf. I). See also Suppl. Video S4. **K,L,** Distribution of central frequencies (Methods) of dendritic (top) and somatic (bottom; inverted y axis) kernels in the four wavebands, separated into On (K) and Off (L) kernels. Wilcoxon rank-sum test, 1 tailed with correction for multiple comparisons for all pairwise comparisons between same polarity distributions of spectral centroids, is shown. Dendrites: all $p < 0.001$ except R_{Off} versus G_{Off} ($p = 0.0011$) and G_{On} versus B_{On} ($p = 0.69$). Somata: all $p < 0.001$ except R_{On} versus U_{On} ($p = 0.00101$), R_{Off} versus G_{Off} ($p = 0.033$), G_{On} versus B_{On} ($p = 0.045$), B_{On} versus U_{On} ($p = 0.064$), R_{On} versus B_{On} ($p = 0.25$), and R_{On} versus G_{On} ($p = 0.57$).

3.2.3. RGC dendrites simultaneously encode contrast, time and colour

To determine the dominant functional properties of RGC processes in different regions of the eye, we mapped each dendritic ROI to a bin within an 'Eye-IPL map'. In this representation, the x-coordinate indicates position across the eye (e.g., dorsal, nasal) while the y-coordinate represents IPL depth (Fig. 3.2C,D). We then computed the mean light response of each Eye-IPL bin to the chirp stimulus and projected its time axis into the third dimension to generate an array linking eye position (x), IPL position (y) and time (z) (Fig. 3.2E). In this representation, the spatially resolved mean response of all RGC dendrites could be visualised as a movie (Suppl. Videos S2,S3). Alternatively, the mean RGC response in an eye region could be viewed as a trace over time (Fig. 3.2F) or individual time-points depicted as images over Eye-IPL-space (Fig. 3.2G). As observed, the polarity, transience and frequency tuning of RGC dendrites all varied systematically across the eye. For comparison, a region in the acute zone's On-layer (region 1 [r_1]) on average responded to the onset of a flash of light and displayed broad frequency tuning to temporal flicker (Fig. 3.2F, top). In contrast, a region in the dorsal eye's Off-layer (r_2) on average presented an Off-dominant transient On-Off-response and low-pass tuning to temporal flicker (Fig. 3.2F, bottom). Accordingly, inspection of individual time points (t_{1-4}) revealed a highly

asymmetrical distribution of these response properties across both the IPL (y) and the eye (x; Fig. 3.2G). For instance, instead of neatly forming two parallel bands of On- and Off responses, the position of the On-Off boundary was highly variable across the eye ($t_{1,2}$ in Fig. 3.2G). Off responses dominated much of the IPL dorsally but were reduced to a tenth of the IPL width ventrally. The mean temporal frequency preference was also dependent on eye position; the dorsal-most retina displayed the most low-pass tuning to temporal flicker, while increasingly ventral regions progressively switched to band-pass tuning ($t_{3,4}$ in Fig. 3.2G; Suppl. Video S3). As observed under this achromatic scheme, different regions of the eye on average differentially encoded the polarity and speed of visual stimuli.

We next asked how these properties relate to the zebrafish's four spectral input channels. First, we mapped the spectral kernels onto the same reference frame, generating four kernel-movies, one each for red, green, blue and UV stimulation (Suppl. Video S4). We then compared the temporal profiles across the same regions r_1 and r_2 as before. Consistent with the achromatic chirp response (Fig. 3.2F), r_1 was dominated by On-kernels, while r_2 was dominated by Off-kernels (Fig. 3.2H,I). Further, time-courses between individual spectral bands varied considerably. For instance, r_1 presented a biphasic UV-On-kernel, temporally offset biphasic red and green On-kernels, and a monophasic blue Off-kernel. Similarly, r_2 revealed distinct temporal profiles across red (biphasic), green (weakly biphasic) and blue (monophasic). Notably, spectral information was not only encoded by the gain and polarity of RGC responses, but also intermixed with temporal information.

To more systematically explore the potential interdependence between spectral and temporal processing, we plotted the kernel movies as a time series (Suppl. Fig. S2I; cf. Suppl. Video S4) and focused on two time points that aligned with the peaks of On- and Off-lobes of most kernels (t_6 and t_5, respectively, in Fig. 3.2J). In this representation, the red

and green kernel-maps echoed that of the achromatic On (t_1) and Off (t_2) response profiles during chirp stimulation (Fig. 3.2J; cf. $t_{1,2}$ in Fig. 3.2G). In contrast, a dominant On-lobe was markedly absent in blue kernels (Fig. 3.2J, blue, bottom), in line with their overall Off-dominance (cf. Fig. 3.2B and Suppl. Fig. S2H). Finally, UV-kernels were even more distinctive; in the acute zone, their IPL-depth profile largely resembled red/green kernels (Fig. 3.2J, magenta), whereas for the remainder of the eye, much of the On-band seen in red/green instead transitioned into a secondary UV Off-band (Fig. 3.2J, magenta, top). To quantify the differences in the distribution of On- and Off- signals, we computed an On-Off index (OOi; Methods): OOis of 1 and -1 denote regions entirely comprised of On and Off kernels respectively, while an OOi of zero indicates an equal proportion of On and Off kernels. The resultant OOi maps reaffirmed the differential distributions of On- and Off-signals observed across the individual kernel-maps (Suppl. Fig. S2J).

Next, we considered the temporal domain. Throughout Eye-IPL space, red and green maps mirrored each other (Fig. 3.2J, cf. Suppl. Fig. S2I). In contrast, the blue-map consistently lagged across the entire eye, while the UV-map displayed a complex temporal behaviour; in particular, the acute zone was distinctive from the rest of the eye yet again (Fig. 3.2J; best seen in Suppl. Video S4). These broad differences were also reflected in the central frequencies of the kernels (spectral centroid from Fourier transform; Methods) irrespective of eye position (Fig. 3.2K,L). Red and green kernels displayed a narrow range of intermediate central frequencies, while blue kernels were slowed and UV sped up. These differences were particularly pronounced for Off- (Fig. 3.2L) versus On-kernels (Fig. 3.2K). Together, this functional overview strongly suggests that (1) information received across the four individual wavebands of light are potentially used in distinct ways to support vision, and (2) their variable use is position-dependent within the visual field space (Baden et al.,

2020; Discussion). To further examine how spectral information might serve zebrafish vision at the level of the retina's output, we next probed RGC responses for spectral opponency.

3.2.4. An abundance of temporally complex colour opponent RGCs

When combining the signal from multiple cone pathways for output to the brain, the number of possible wiring combinations is given by the number of possible wiring states (i.e., 3: On, Off, and no connection) raised to the power of the number of cone types (i.e., 4). Accordingly, the zebrafish's four cone types could be wired in a total of $3^4 = 81$ combinations. Of these, 50 are colour-opponent, 30 are non-opponent (15 On + 15 Off), and one represents the case where none of the four cones is functionally connected. We assessed how zebrafish RGCs span this combinatorial space and ranked the results based on the number of allocated dendritic ROIs in each wiring group (Fig. 3.3).

Most ROIs constitute a small subset of groups with relatively simple functional wiring motifs. Among dendrites, the two most common combinations were RGB_{Off} and RG_{Off} (Fig. 3.3A, top, dark grey and Fig. 3.3B, groups 1,2). These non-opponent Off groups were followed by one colour opponent group (RG_{On}-B_{Off}, brown/orange; group 3) and then two non-opponent On groups (RG_{On} and RGB_{On}, light-grey; groups 4,5). Together, these accounted for 42% of all dendritic ROIs. Thereafter, remaining groups were more diverse and largely comprised colour opponent groups to represent a total of 47% colour opponent ROIs among dendrites (e.g., Fig. 3.3B, groups 6,7,9,10). Of these, as high as 75% opponent computations had a single zero crossing in wavelength: R/G (30%), G/B (31%), B/U (8%), G/U (4%) and R/U (2%), respectively (e.g., Fig. 3.3B, groups 3,6,10). The remaining 25% of opponent ROIs exhibited a range of complex opponencies (e.g., Fig. 3.3B, groups 7,9).

Somatic ROIs presented a similar distribution; 51% non-opponent and 49% opponent – of which 67% and 33% had simple and complex opponencies, respectively (Fig 3.3A, bottom), with a notable reduction in the first two Off groups (cf. Fig. 3.2A).

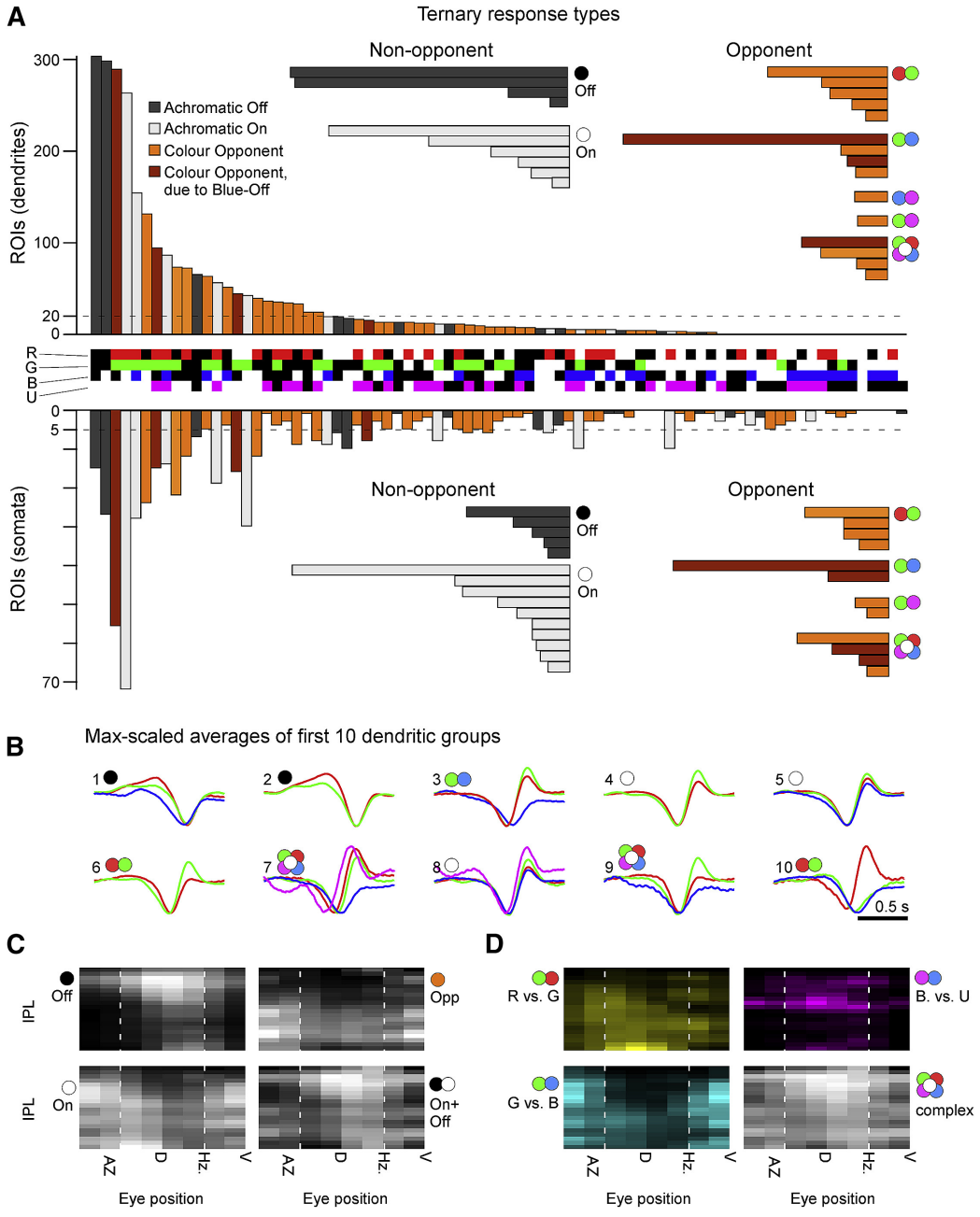

Figure 3.3. | **Diverse colour opponencies in RGCs. A,** Each dendritic (top) and somatic (bottom; inverted y axis) ROI that passed a minimum response criterion (Methods) was allocated to a single bin in a ternary classification scheme based on the relative polarities of their four spectral kernels (3 response states: On, Off, and no response) raised to the power of 4 spectral channels (red, green, blue, and UV): $3^4 = 81$ possible combinations. The central row between the bar graphs specifies each bin's spectral profile: 'On' (red, green, blue, and UV); 'Off' (black in the respective row); and no response (white in the respective row). For example, the leftmost group, which comprised the highest number of dendritic ROIs, represents ROIs displaying Off

kernels in red, green, and blue, while showing no response in UV. The bar graphs are colour coded as follows: dark grey (non-opponent Off); light grey (non-opponent On); and orange/brown (opponent). Brown bins indicate opponent bins that are only classified as opponent because they comprise a Blue-Off component (see main text). The horizontal insets summarise all ternary response groups that exceeded a minimum size (indicated by the dashed line) across the following categories: Off, On, and Opponents, here divided into types of spectral computations as indicated by the coloured circle; two-colour symbols denote 'simple' opponencies (single spectral zero crossing, e.g., red versus green) between the indicated wavebands (red, green, blue, and UV), while the 'flower' symbol denotes complex opponencies (>1 spectral zero crossing, e.g., red and blue versus green). **B,** Maximum-amplitude scaled average kernels of the ten most abundant spectral classes among dendrites in (A). **C, D,** Dendritic groups from (A) summarised based on their position in an Eye-IPL map (cf. Fig. 3.2). (C) outlines major groups: Off (left, top) and On non-opponent (left, bottom); opponent (right, top); and On+Off non-opponent (right, bottom). (D) As (C), with opponent groups segregated by their specific spectral computations as indicated. Note that most specific functions in (C) and (D) are confined to specific regions of the eye and IPL. For example, green versus blue simple opponent computations occur mainly in the ON layers of the ventral retina that survey the environment overhead (D, bottom left).

As before (cf. Fig. 3.2), the diverse functional groups of non-opponent and opponent RGC processes distributed asymmetrically across the eye and IPL depth (Fig. 3.3C,D). Colour-opponent RGCs were present throughout the eye, but differed in the types of opponencies that dominated different regions of the IPL and visual field (Fig. 3.3D). For instance, B/U opponent responses were mainly confined to the Off-layer of the dorsal retina, while G/B computations mostly occurred ventrally. R/G computations were more widely distributed but, like B/U computations, were biased to the dorsal retina.

3.2.5. Pronounced regionalisation of functional RGC types

While sorting RGCs based on their relative polarities to different wavelength light is informative on the distribution of spectral computations (Fig. 3.3), it omits key temporal and amplitude details. As an alternate means to visualise the major functional RGC types of the larval zebrafish eye, we clustered their full temporo-chromatic response profiles (Methods). Dendritic ROIs were sorted into 17 functional clusters, of which 15 ($C_{1\text{-}15}$) that contained a minimum of 10 ROIs were kept for further analyses. Somatic ROIs were allocated to 20 clusters, of which 13 that had more than 5 ROIs were retained (Suppl. Fig. S3). In general, dendritic and somatic clusters presented similar functional properties and distributions across the eye; although overall, dendritic ROIs produced more cleanly

separated clusters, as expected based on their higher abundance and larger signal-to-noise (cf. Fig. 3.2A). We therefore focus on the description of dendritic data, drawing on somatic clusters as a point of comparison, while taking into account whether and how our functional clusters correspond to 'real' RGC types with stereotypical morphology, function and genetics, remains an open question.

Dendritic clusters comprised mainly achromatic On- ($C_{1,10,12}$) and Off- ($C_{11,\ 13\text{-}15}$) clusters as well as clusters presenting a variety of spectral and temporal response properties ($C_{2\text{-}9}$; Fig. 3.4). Here, when clustered by this broader range of response properties, opponency was a less obvious feature, unlike previous sorting by opponency alone (Fig. 3.3). Moreover, opponency was often primarily driven by the slow B_{Off} component opposing non-blue On-kernels (Fig. 3.4A,D,E, see also Fig. 3.4H). In fact, only four clusters did not present an obvious slow B_{Off} response: C_3, which was non-responsive to short wavelength stimulation, and the three achromatic On clusters ($C_{1,10,12}$). Somatic clusters similarly showed a marked prevalence of slow B_{Off} signals ($C_{1\text{-}8,10\text{-}13}$ in Suppl. Fig S3).

Most clusters of either dataset displayed skewed regional biases to specific areas of visual space. For instance, many dendritic clusters were biased to either the upper ($C_{4\text{-}8}$) or lower visual field ($C_{10,12\text{-}15}$ Fig. 3.4C; summarised in Fig. 3.4G, top). Other clusters showed varying levels of preference for the horizon ($C_{2,11}$), the outward visual field ($C_{3,9}$), or the frontal visual field (C_5), including the acute zone (C_1). Somatic clusters showed similar regional biases (Fig. 3.4G, bottom); although their two largest clusters ($C_{5,8}$) presented a more complex distribution, suggesting that these clusters likely include a variety of differentially distributed functional RGCs (Fig. 3.4G, bottom, 'mixed').

Among dendritic clusters, C_1, and to a lesser extent $C_{6,8}$, stood out due to its strong response to UV-stimulation (Fig. 3.4A, D, E), despite the ~17-fold reduction in UV signal

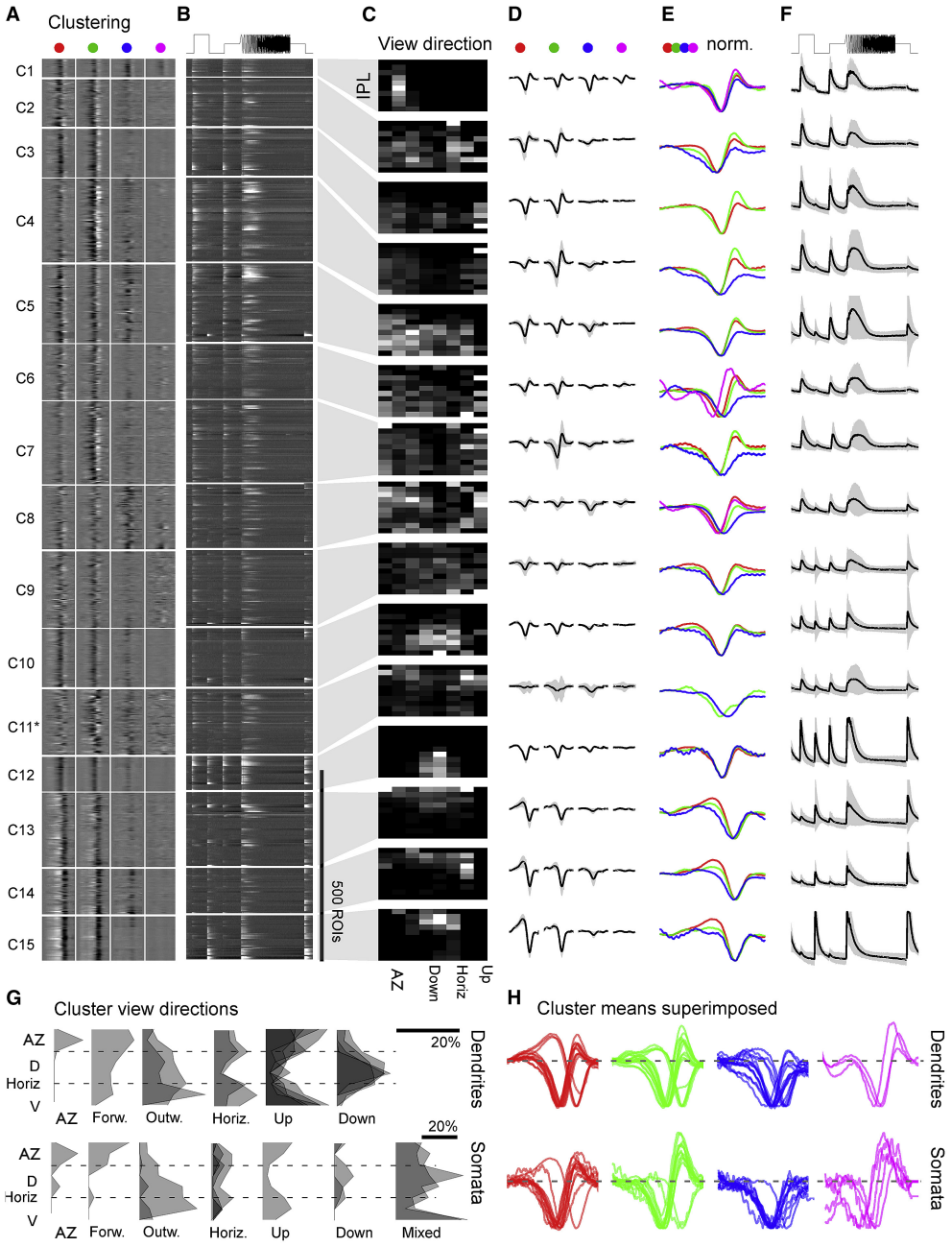

Figure 3.4. | **Functional clustering of dendritic ROIs. A-F,** Dendritic ROIs from across the entire eye were clustered based on their four spectral kernels (Methods) to generate a total of n = 15 functional clusters that comprised a minimum of 10 ROIs. Shown are heatmaps of red, green, blue, and UV kernels (A; from left to right, respectively) and associated mean chirp response (B), with each entry showing a single ROI, followed by each cluster's Eye-IPL projection (C), each mean kernel (D), max-scaled kernels superimposed (E), and the mean chirp response (F). Error shadings in SD are shown. For clarity, low-amplitude mean kernels were omitted from column (E). Note that C_{11}* comprised a mixture of responses and may include a variety of low-n functional RGC types. Greyscale colour maps (A–C) were linearly equalized by hand to maximize subjective discriminability of the full response range across the population of all recordings in a dataset. Lighter greys indicate higher activity/kernel amplitudes. For corresponding data on somata, see Suppl. Fig. S3. **G,** Summary of cluster distributions across the eye, irrespective of IPL depths, for dendritic (top) and somatic (bottom) clusters, scaled by their relative abundance (in %; see scale bars). Eye-distribution profiles were manually allocated to one of the following groups based on which area of visual space is mainly surveyed: AZ (dendritic C_1; somatic C_2); forward (dendritic C_5; somatic C_3); outward (dendritic $C_{3,9}$; somatic $C_{9,11}$); horizon (dendritic $C_{2,11}$; somatic $C_{1,4,10}$); up (dendritic C_{4-8}; somatic C_7); and down (dendritic $C_{10,12-15}$; somatic $C_{12,13}$). Two large clusters (somatic $C_{5,8}$) did not obviously fit to any of these categories and were instead grouped separately as

'mixed'. It is possible that these clusters comprise several smaller groups of functional RGCs with distinct eye-wide distributions. **H,** As (E) for both dendritic (top) and somatic (bottom) data, but with all spectral kernels in each waveband superimposed. Note kinetic similarities across most red and green kernels and near complete absence of positive deflections in blue kernels.

power relative to red to match natural light (cf. Fig. 3.1B). This sustained On-cluster (Fig. 3.4F) remained neatly confined to a single regional bin, coinciding with the acute zone (Fig. 3.4C). A functionally alike cluster restricted to the acute zone also featured among somatic ROIs (C_2). Taking into account the strong regionalisation of behavioural responses to prey-like stimuli (Bianco et al., 2011; Gebhardt et al., 2019; Mearns et al., 2020), and the strong facilitatory effect of UV light in prey-capture performance (Yoshimatsu et al., 2020), dendritic C_1 and somatic C_2 may collectively constitute a subset of RGCs responsible for visual guided prey-capture in larval zebrafish (Antinucci et al., 2019; Semmelhack et al., 2014; Yoshimatsu et al., 2020). Of note, likely in part due to their strict localisation, these putative prey-capture clusters only made up a small fraction of ROIs in this dataset (3%-5% among dendrites and somata, respectively).

3.3. Discussion

We have shown that the function of larval zebrafish RGC circuits is highly dependent on their position in the eye, likely to meet visuo-ecological and behavioural demands in their natural visual environment (Baden et al., 2020). The localised presence of sustained UV-On RGCs in the acute zone (Fig. 3.4) can be linked to their survival need to detect and focalise small UV-bright prey in the upper frontal visual field (Bianco et al., 2011; Mearns et al., 2020; Semmelhack et al., 2014; Yoshimatsu et al., 2020). Likewise, the dominance of long- over short-wavelength responses in the lower visual field (Fig. 3.2B) is consistent with the predominance of long-wavelength light in the lower water column (Muaddi and Jamal, 1991; Nevala and Baden, 2019), and crucially, the zebrafish's innate stabilisation

behaviour to monitor the ground for image shifts that drive the long-wavelength biased optomotor response (Krauss and Neumeyer, 2003; Orger and Baier, 2005).

In the above aspects, our data from RGCs expand on our previous findings on the spectral responses of presynaptic BCs (Zimmermann et al., 2018). However, not all functions of BCs were faithfully acquired by downstream RGCs. For instance, the marked prevalence of slow blue-Off circuits among RGCs (Figs. 3.2-3.4) was not predicted from BCs, which instead presented an approximately even mix of blue-On and -Off circuits (Zimmermann et al., 2018). Further, the striking near-complete absence of blue-On signals in zebrafish RGCs is at odds with the significance of blue-On RGC circuits in mammals (Marshak and Mills, 2014; Mills et al., 2014) including primates (Calkins et al., 1998; Dacey and Lee, 1994). Next, while many of the dominant spectral opponencies observed in RGCs (Fig. 3.3) are already present at the level of BCs (Zimmermann et al., 2018), the interplay between time and wavelength was more evident in the former (Fig. 3.2,3.4). Together, our data suggests other influences in combination with BCs, likely ACs (Torvund et al., 2017), involved in further processing of temporo-spectral information.

Notably, there was no expected increase in the diversity of zebrafish RGC functions (Fig. 3.4) compared to BCs (Zimmermann et al., 2018), in stark contrast to the approximate 3-fold increase in neuron types from BCs to RGCs in mice (Baden et al., 2018). Although, it is highly likely that zebrafish functional RGC diversity would substantially increase if spatial processing were factored in (Franke et al., 2019), which was not a focus of this study. Indeed, an anatomical census place the number of structural RGC types in larval zebrafish upwards of 50 (Robles et al., 2014), which cannot be adequately explained by the comparatively modest diversity obtained from our clustering of temporo-chromatic receptive fields.

3.3.1. A note on ROI segmentation and identity

We used 2-photon imaging of Islet2b:mGCaMP6f signals in the eye's GCL and IPL to functionally survey RGC functions in larval zebrafish. While this approach likely provides for a useful approximation of what the zebrafish's eye tells the zebrafish's brain, two main caveats must be considered. First, while Islet2b is an effective and popular marker for zebrafish RGCs it is neither exclusive to RGCs nor inclusive of all RGCs. In our Islet2b:mGCaMP6f line, immunostaining against GFP and GABA revealed that some dACs also express GCaMP6f (Suppl. Fig. S1B), indicating that our dataset contains a minority of signals from dACs. In addition, small numbers of INL somata are labelled, indicating that also a minority of ACs contribute to our dendritic signals (AC somata are not included since these are easily discarded based on location). Conversely, not all axonal arborisation fields (AFs) in the brain, as revealed after DiO injection into the eye, were also strongly innervated by mGCaMP6f expressing RGCs (Suppl. Fig. S1C), suggesting that a subset of RGC types may be absent in our dataset. Finally, also a small fraction of central neurons were labelled as evident from their soma locations near the (pre)tectal neuropils. Second, population imaging of RGC dendrites in the eye is potentially fraught with many of the same problems that are associated with delineating their axonal signals in the brain (Nikolaou et al., 2012). Specifically, the high density and overlap of dendritic processes across the IPL means that it is impossible to tell if groups of dendritic ROIs belong to the same RGC (Figs. 3.1D,E). Nevertheless, functional dendritic data is indicative of the local computations that occur within RGC dendrites as they integrate signals from BCs and ACs in different layers of the IPL and in different positions of the eye (Ran et al., 2019). Further, our single cell data (Suppl. Fig. 2A-D) suggests that dendritic signals in population recordings are probably also a reasonable proxy for somatic signals, with the added benefit

that their signal-to-noise was generally higher (cf. Fig. 3.2A). To what extent the indicated close similarity of dendritic and somatic signals in zebrafish RGCs applies across all RGC types, and to what extent this can be linked to their generally small absolute size (e.g., compared to RGCs in larger eyes), will be important to address in the future.

The somata of RGCs in the GCL could generally be reliably segmented in population recordings. In view of their proximity to the axon hillock, data from RGC somata may serve as a useful indication of the signal sent from the eye to the brain. Nevertheless, addressing how exactly somatic calcium signals are linked to spikes sent down the optic nerve will be important in the future. This may then also go partway to explaining the marked reduction in Off-responses in somatic data compared to dendrites (Fig. 3.2A,B; 3.3A), and more broadly to drive our understanding of how this tiny animal's eye communicates with its brain.

3.3.2. Linking wavelength to visual and behavioural functions

In general, our data from zebrafish substantiates the long-held view that achromatic image forming vision in animals is dominated by mid- and long-wavelength channels (Fig. 3.2G,J, 3.3A,B) (Baden and Osorio, 2019). Indeed, a close link between mid/long-wavelength vision and achromatic vision is a recurring theme in diverse species across both invertebrates and vertebrates, including humans (Buchsbaum and Gottschalk, 1983; Jacobs and Rowe, 2004; Osorio and Vorobyev, 2008; Solomon and Lennie, 2007). It enables visual systems to take advantage of the abundance of mid- and long-wavelength photons in natural light (Muaddi and Jamal, 1991), utilising the majority of retinal channels, to support high spatial and temporal acuity vision (Atick et al., 1992; Baden et al., 2020; Buchsbaum and Gottschalk, 1983; Lewis and Zhaoping, 2006; Maloney, 1986). In parallel,

spectral information can then be transmitted by reasonably fewer retinal output channels to 'colour in' the greyscale scene in central circuits (Baden and Osorio, 2019; Dacey and Packer, 2003; Jacobs, 1993; Kelber et al., 2003; Neitz and Neitz, 2011). Our finding that, in zebrafish, most opponent RGCs encode simple rather than complex opponencies is in agreement with previous work (Baden and Osorio, 2019; Kamermans et al., 1991, 1998; Zimmermann et al., 2018), and can be linked to the predominance of simple over complex spectral contrasts in natural scenes (Buchsbaum and Gottschalk, 1983; Lewis and Zhaoping, 2006; Maloney, 1986; Nevala and Baden, 2019; Ruderman et al., 1998; Zimmermann et al., 2018).

This fundamental textbook view however, does not adequately explain the other crucial findings. It does not answer (1) why nearly half of all output channels are colour opponent – it should be considerably fewer (Lewis and Zhaoping, 2006; Nevala and Baden, 2019), (2) the striking mix of time and spectral information throughout the eye, (3) the near complete absence of blue-On circuits or the ubiquitous blue-Off lagging channel, or (4) the complex distribution of diverse UV-responses across the eye.

Presumably spectral processing and opponency should in some way accomplish image forming colour vision (Baden and Osorio, 2019), yet spectral information has been shown to be utilised for other means. For instance, blue-light opponency may serve other non-image-forming functions such as circadian entrainment (Lazopulo et al., 2019; Mouland et al., 2019; Walmsley et al., 2015), and/or as serve as a depth gauge (Verasztó et al., 2018).

More generally, we propose that the zebrafish may use two separate and spectrally distinct achromatic systems: a long-wavelength biased achromatic system for traditional image forming vision, and a second, short-wavelength biased achromatic system to detect image features that stand out in this waveband – prey and predators. The latter system could

potentially be linked to how water scatters UV-light (Janssen, 1981), submerging the typically busy visual background in a horizontally homogenous UV-haze. Objects appearing in the foreground, such as paramecia or predators, then stand out as UV-bright or UV-dark objects, respectively (Cronin and Bok, 2016; Yoshimatsu et al., 2020). Additionally, this scatter of UV-light sets up a vertical brightness gradient, which could in part contribute to the dominance of UV-circuits in the upper visual field.

This hypothetical dual-achromatic strategy would position the blue channel somewhere in between, encoding a mixture of red/green background and the UV-foreground. Perhaps blue circuits could then potentially be utilised as a subtraction signal to better delineate achromatic red/green-vision from achromatic UV-vision. Daylight tends to be red/green biased yet highly correlated across the full visible spectrum in the zebrafish natural habitat (Nevala and Baden, 2019); therefore, as much of the brightness information in natural-scenes will also be visible to the long-wavelength tail of the UV-photopigment, any UV-specific signals, which tend to be comparatively weaker, could potentially be contaminated (Nevala and Baden, 2019; Yoshimatsu et al., 2020). To a lesser extent, such spectral contamination could also occur in reverse. By picking up the low-power tail of both signals, the blue photopigment is ideally positioned to segregate long- from short- wavelength circuits. Accordingly, subtracting the blue component from either or both UV- and red/green circuits may enhance spectral delineation without sacrificing overall signal power.

Indeed, if the main function of blue-Off circuits were not to support image forming colour vision, but instead serve as a 'universal background signal', we may disregard it from our account of colour-opponency in zebrafish RGCs (Fig. 3.3A, highlighted in brown). As a result, two of the three most abundant colour-opponent groups among both dendrites and

somata (RG_{On}-B_{Off} and RGU_{On}-B_{Off}) would instead be classed as non-opponent On-responses (Fig. 3.3A); remaining colour opponent RGCs would also drop to 28% and 32% among dendrites and somata, respectively (Baden and Osorio, 2019). The interdependence between spectral and temporal processing could also be explained by a dual-achromatic segregation by a blue channel: a blue-Off background subtraction system might benefit from a long integration time to be relatively less perturbed by rapid changes in the visual scene. Notwithstanding our findings, our interpretations remain largely speculative. In the future, it will be imperative to specifically address feasible predictions.

3.3.3. The zebrafish area temporalis as an accessible model for the primate fovea?

Most studies on foveal function and dysfunction have been restricted to primates, due to the lack of an equivalent specialisation in many accessible model systems in vertebrate vision research, notably including mice (Baden et al., 2020). Here, we find that the larval zebrafish's *area temporalis* (or acute zone) mimics several properties of the primate fovea, and may potentially serve as an experimentally accessible alternative. Behaviourally, larval zebrafish guide their acute zone onto prey targets during fixational eye movements for high acuity binocular vision and distance estimation (Bianco et al., 2011; Mearns et al., 2020; Yoshimatsu et al., 2020), analogous to fixational eye-movements in primates. Functionally, zebrafish UV-cones in the acute zone boost signal-to-noise by using enlarged outer segments and slowed kinetics based on molecular tuning of their phototransduction cascade (Yoshimatsu et al., 2020) – specialisations that also occur in primate foveal cones (Peng et al., 2019; Sinha et al., 2017). Our data on RGC distributions and functions in larval zebrafish substantiates this notion. First, zebrafish have a fovea-like reduced ratio of ACs compared to RGCs in their acute zone (Suppl. Fig. 4A,B). Next, like in the primate fovea (Dacey, 2000; Sinha et al., 2017), RGC circuits in the acute zone are spectrally distinct to

those of the peripheral retina (Fig. 3.2-3.4). Finally, in separate anatomical experiments, we find structurally distinct RGCs in the acute zone (Suppl. Fig. S5A-M), including morphological types with a small dendritic field area barely covering the width of their soma (Suppl. Fig. 5J,K; see also [Robles et al., 2014]). Crucially, a small dendritic field is associated with a correspondingly small-sized spatial receptive field (Jacoby and Schwartz, 2017) necessary to detect minute prey-like visual targets (Bianco et al., 2011; Semmelhack et al., 2014; Yoshimatsu et al., 2020). In the future, it will be imperative to explore further aspects of the zebrafish acute zone, if any, analogous to primate foveal vision; and in parallel, explore how such links between the two retinal systems may generalise across acute zones of other vertebrates (Baden et al., 2020).

Chapter 4

Mapping RGC receptive fields in the in-vivo larval zebrafish

4.1. Introduction

Hubel and Wiesel (1959) observed that while some cortical neurons responded to a single spot of light, majority were maximally activated by a moving edge of the same orientation as their receptive field (RF) – earning the term edge detectors. Lettvin et al., (1959) would later follow up with work on the response properties of *Xenopus* ganglion cells. From their recordings, they proposed a bug perceiver – a 'convexity detector' sensitive to small (3°) objects moving within the receptive field of a particular neuronal subtype. This was perhaps one of the first proposed links of a neuron type receptive field preference to a behavioural outcome. Later RF mapping studies would substitute the physiological stimuli used by Lettvin et al., (1959) with more objective stimuli, including drifting gratings (Enroth-Cugell and Robson, 1966) and white noise (Jones and Palmer, 1987).

4.1.1. Ganglion cells have context-dependent dynamic receptive fields

A common theme among feature detectors identified to date is that most of these neuron types process some form of image motion. Indeed, moving objects in the visual scene tend to be of interest, be it a threat or opportunity. Similarly, optic flow on the retina informs self-motion through the environment. From an ethological standpoint, it is reasonable that specific circuits evolved to extract such salient cues from a visual scene. The once classical description of a 'static' ganglion cell receptive field has since been reworked to capture dynamic properties and contextual influences that cannot be explained by linear summation within the spatial receptive field. Individual neurons integrate incoming visual signals over their receptive fields; it is this signal integration that confers types of ganglion cells with specific functions (Gollisch and Meister, 2010; Schwartz and Rieke, 2011). To date, studies on feature selective neurons and their underlying neural circuits have identified zebrafish RGCs selective for stimulus size (Del Bene et al., 2010; Preuss et al.,

2014), orientation (Antinucci et al., 2016) and direction of motion (Gabriel et al., 2012; Lowe et al., 2013; Nikolaou et al., 2012). Yet, despite the fact that mapping receptive fields of neurons can provide valuable insight into how visual input is processed, surprisingly little is known about the visual receptive fields of zebrafish RGCs; only a handful of studies have characterised the receptive field properties of these cells and their tectal counterparts in the zebrafish (Bergmann et al., 2018; Johnston et al., 2014; Niell and Smith, 2005; Sajovic and Levinthal, 1982a,b; Zhang et al., 2011).

4.1.2. Defining a visual receptive field

The most general definition of a RGC receptive field would be an understanding of the stimulus to response relationship – the link between spatiotemporal patterns of light and RGC spikes. The visual system processes stimuli through differential spatial and temporal filters (Kuffler, 1973); in the spatial domain, the RF is the area in visual space in which presentation of a stimulus elicits a response, while the temporal RF describes how the neuron responds over time to a given stimulus. Receptive field properties of individual visual neurons are dictated by the precise patterns of synaptic inputs, including their arrangement in visual space and features such as polarity. The process of mapping RFs generates an informative readout of the visual tuning properties of individual neurons.

4.1.3. Measuring the RGC receptive field

The first-order classification of a RGC receptive field is generally defined by the polarity of its light response, i.e., On, Off, or On-Off (Sanes and Masland, 2015). Following polarity, receptive field size is highly prioritised, being a major determinant of the spatial resolution of a RGC channel, which in turn, is highly predictive of the spatial extent of an RGC's dendrites across the retina surface. It would similarly be intuitive to describe the kinetics

of RGC light responses, i.e., transient versus sustained, to distinguish between RGC types (Baden et al., 2016; Levick, 1967). Though not typically included in RF mapping, other aspects of RGC responses such as contrast sensitivity, or spatial frequency, and selectivity for specific features e.g., orientation or direction of motion, are equally informative in adding to a comprehensive description of RGC light responses.

4.1.4. RF mapping with spatiotemporal white noise

Initial approaches to map RFs in the visual system utilised spots or bars flashed at various locations while simultaneously recording spikes from a single neuron (Hubel and Wiesel, 1959). Such a time-consuming technique cannot be systematically applied to recording activity from a population of neurons. It was not until Enroth-Cugel and Robson (1966) who introduced the revolutionary method of using sinusoidal drifting gratings, a stimulus most RGCs respond robustly to, that rapid measurement of spatial RFs was feasible. Similarly following a linear systems approach, spatiotemporal white noise would later succeed as the method of choice to investigate RGC receptive fields (Brown et al., 2000; Chichilnisky, 2001; De Vries and Baylor, 1997; Field et al., 2010; Marre et al., 2012; Sher & De Vries, 2012). Classically, a 'checkerboard' with randomly flickering squares – a 'white noise' stimulus varying randomly in space and time – is presented to the retina, and RGC responses recorded (Chichilnisky, 2001; Meister et al., 1994). The principle behind the straightforward method of spike-triggered-average (STA) is reverse correlation of the spikes to the white noise stimulus; whenever the neuron responds, this operation looks at the stimulus sequence preceding the spike, and computes the mean. The result is an estimate of the stimulus that optimally activated the neuron. Like the drifting gratings, this method allows reconstruction of RFs from many cells in parallel to monitor activity across

populations of RGCs, making it particularly applicable for *in vivo* optical population imaging or multi-electrode array (MEA) recordings.

4.1.5. Imaging spatial activity in the in vivo larval zebrafish eye

As probing the response properties of zebrafish RGCs with full-field stimuli misses key information such as size, orientation or direction preference – critical for visually-driven behaviours i.e., prey hunting or predator avoidance – we followed up with a prototype of a tetrachromatic spatial stimulator (Franke et al., 2019), to reveal more complex features of RGC visual receptive fields using motion stimuli. We first verified with moving bars that our spatial stimulator was functional, and that motion stimuli was able to elicit robust responses from our RGC transgenic line. Next, we developed variations of the spatiotemporal white noise using colour checkerboards presented individually, as well as in sequential order or combinatorial overlays, to systematically characterise the spatial receptive field structure, and potentially explore if the RFs constitute one or more coherent functional channels. Continuing with the *Islet2b:mGCaMP6f* larval zebrafish (Janiak et al., 2019; Zhou et al., 2020), we tested a variety of preliminary stimuli, adjusting parameters and refining analyses as we went along, based on RGC responses obtained in the preceding experiments. Preliminary data demonstrate the potential of using variations of tetrachromatic checkerboards to reconstruct RGC RFs in the zebrafish retina, as well as further exploration of other types of motion stimuli for a comprehensive functional characterisation of zebrafish RGCs.

4.2. Results

4.2.1. Motion and oriented stimuli evoked robust responses in RGCs in the in vivo eye

We recorded visually evoked calcium responses from RGC processes in the retina under two-photon while presenting light moving bars across the visual field of 6-8 dpf *Islet2b:mGCaMP6f* larval zebrafish. Recordings were performed in the eye's transverse plane (Fig. 4.1A,B). The moving bar travelled in eight directions evenly spanning 360°. Moving bar stimulation is routinely used to characterise direction- and orientation-selectivity in the zebrafish visual system (Antinucci et al., 2016; Gabriel et al., 2012; Hunter et al., 2013; Nikolaou et al., 2012), and here, induced robust responses in RGC dendrites and somata.

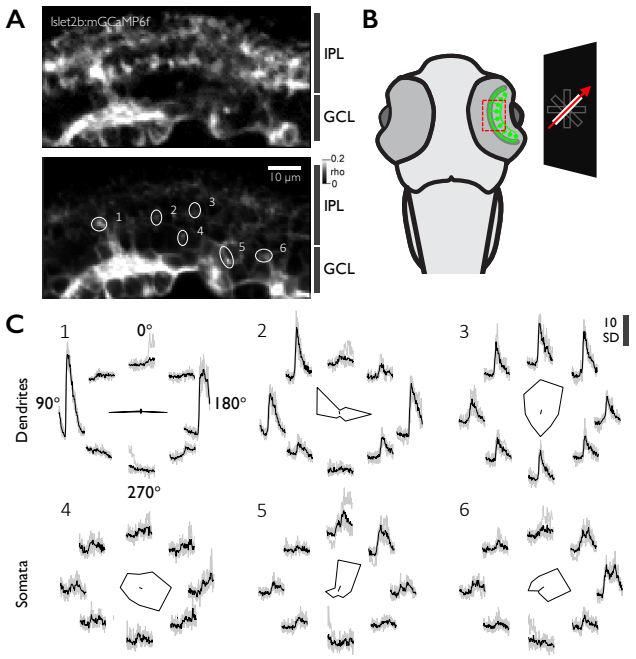

Figure 4.1. | RGC dendrites and somata exhibit a range of direction or orientation selectivity to the moving bar stimulus. A, *Islet2b:mGCaMP6f* expression under two-photon surveyed across the eye's transverse plane as indicated (B). Top: example activity scan with RGC dendrites in the IPL occupying the top part of the scan, and somata in the GCL occupying the bottom part as indicated; bottom: correlation projection (Franke et al., 2017) of activity highlighting responding regions in the scan to a moving bar stimulus, alongside example regions of interest (ROIs). **B,** Schematic of *Islet2b:mGCaMP6f* expression in RGCs (green) across a transverse section of the larval zebrafish eye with the scan area (A) indicated. Light bars on a dark background projected on a screen, travel across the visual field of the zebrafish. **C,** Direction/Orientation-selectivity: mean (black) example responses of dendritic (top row) and somatic (bottom row) ROIs from (A), and individual repeats (grey), to a light bar moving in 8 directions evenly spanning 360°; corresponding polar plots of peak response with the vector sum at the centre.

In an example recording, a selection of ROIs revealed a range of direction or orientation selectivity across both RGC dendrites and somata (Fig. 4.1C); as observed in some ROIs, the response magnitude varied selectively with direction or orientation, i.e., some directions or orientations were preferred over others. For example, dendritic ROI 1 indicated a clear preference for orientation along the horizontal axis, while dendritic ROI 2 was tuned to an oblique orientation. In contrast, dendritic ROI 3 responded robustly whenever the moving bar appeared in its visual field, but in general displayed no obvious bias to any motion direction or orientation; somatic ROI 4 similarly exhibited no directional tuning. By contrast in the same scan region, direction selectivity was observed in somatic ROIs, ROIs 5 and 6. In general, somatic ROIs displayed broader response profiles as compared to the dendrites, and at a lower signal. Overall, RGC processes in the *in vivo* larval zebrafish eye responded robustly to achromatic motion and oriented stimuli.

4.2.2. Chromatic checkerboards reveal a variety of RGC RFs by wavelength

The visual scene comprises parallel layers of information that in addition to colour, describes local contrast, motion, and shapes. Functional characterisation of RGC populations using full-field stimuli in our previous study has its limitations, we therefore followed up with developing motion stimuli protocols, namely flickering colour checkerboards, with a newly custom built tetrachromatic spatial stimulator (Franke et al., 2019). For stimulation, we presented light modulated in time and wavelength, and the added third component – space. As before, the four LEDs were spectrally aligned with the sensitivity peaks of the zebrafish's four cone opsins (R, G, B, UV; Zimmermann et al., 2018), and the power of each LED was tuned to the relative power distribution across wavelength of daytime light in the zebrafish natural habitat (Nevala and Baden, 2019; Zimmermann et al., 2018) to yield a 'natural white' (cf. Fig. 3.1B).

For each binary noise stimulus, a movie of a flickering checkerboard was created where the value assigned to each checker square was either the respective stimulated waveband, i.e., red, green, blue, or UV, or 0, in a random sequence independent of the other squares. We tested a number of protocols, varying the size of checkers on the screen, i.e., 50, 70, 100, or 200 pixels, as well as duration of each frame of the movie, i.e., 0.2, 0.5, 1, or 2 seconds. We first presented checkerboards of a single colour and were able to reconstruct spatially defined RFs with 10 minutes of noise stimulation for each of the four wavebands. However, that was equivalent to a total of 40 minutes scan-time over a single region, leading to several issues including sample drift and fluorescence bleaching. An alternative would be to reduce the length of movie and it appeared that 5 minutes of noise may be sufficient to recover RFs. To come up with a better solution, we created a noise stimulus that displayed the four checkerboards in sequential order R-G-B-U, enabling us to probe responses to all four wavebands in a single scan (Fig. 4.2B). We varied the number of frames per colour switch and found that a 60-frame sequence produced better RFs than a 20-frame sequence. The parameters used for the sequential noise experiments were a 100x100-pixel size checkerboard and 0.5-second frame duration, as this combination appeared to deliver the most consistent response in the single colour checkerboard experiments.

In an example 15.6 Hz recording at 128x64 pixel resolution (Fig. 4.2A), we observed robust activity in the red and green channels, and some activity in the blue and UV (Fig. 4.2B). In agreement, we were able to reconstruct prominent RFs from the red and green channels, and fewer and weaker RFs in the blue channel. However, we weren't able to recover spatial RFs in the UV channel (Fig. 4.2C). To determine if this region lacked UV-sensitive RGCs, we played the UV checkerboard on its own, and managed to recover spatially defined RFs. One such example is the dendritic ROI in the scan region (Fig. 4.2A, red dotted circle),

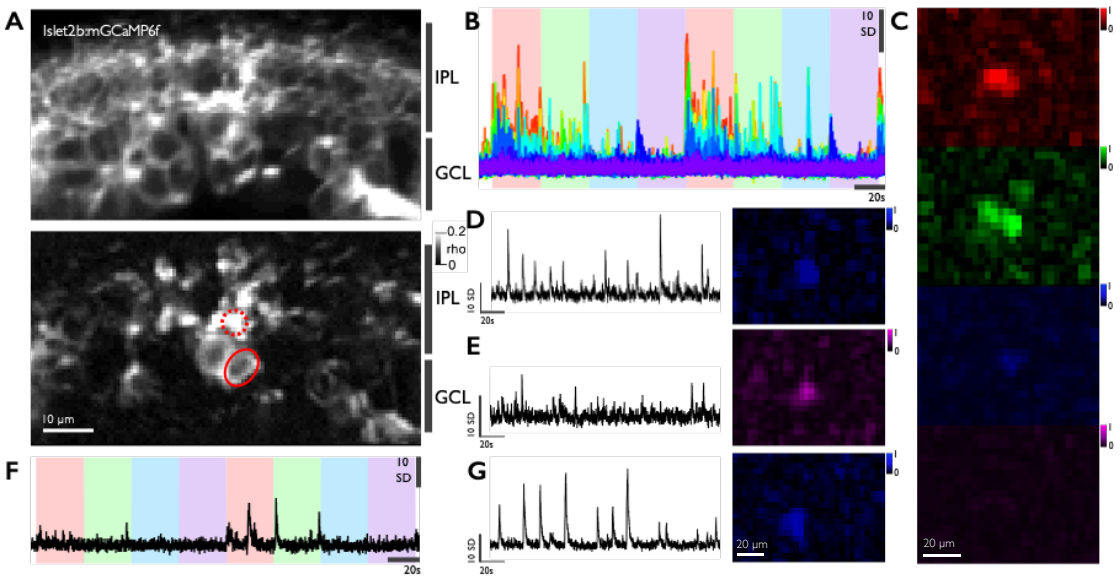

Figure 4.2. | Spatiotemporal colour checkerboards reconstruct a variety of RGC RFs in the four colour channels. A, *Islet2b:mGCaMP6f* expression under two-photon surveyed across the eye's transverse plane. Top: example activity scan with RGC dendrites in the IPL occupying the top part of the scan, and somata in the GCL occupying the bottom part as indicated; bottom: correlation projection (Franke et al., 2017) of activity highlighting responding regions in the scan to flickering colour checkerboards, alongside example regions of interest (ROIs). **B,** Ca^{2+} signals from the scan region in (A) in response to sequential noise stimulation (100x100px checkerboard); each colour trace represents a responding RGC process (ROIs by manual selection). Colour panels represent the order in which the four colour checkerboards were displayed, i.e., R, G, B, U, and in this case, 60 frames for every colour sequence switch (frame duration=0.5s). **C,** Receptive field (RF) centre maps of the four colour channels, reconstructed from responses obtained in (B) from scan region in (A). **D,** Example Ca^{2+} trace recorded from the dendritic ROI in (A; red dotted circle), in response to a flickering blue checkerboard, and its corresponding RF centre map. **E,** Example Ca^{2+} trace recorded from the dendritic ROI in (A; red dotted circle), in response to a flickering UV checkerboard, and its corresponding RF centre map. **F,** Example Ca^{2+} trace recorded from the somatic ROI in (A; red oval), in response to sequential noise stimulation. **G,** Example Ca^{2+} trace recorded from the somatic ROI in (A; red oval), in response to a flickering blue checkerboard, and its corresponding RF centre map.

which displayed a small yet consistent response to the UV checkerboard; subsequent RF reconstruction revealed a spatial RF with a well-defined centre (Fig. 4.2E). Similarly, when presenting only the blue checkerboard, the same dendritic process responded strongly, and exhibited a more pronounced spatial RF (Fig. 4.2D), compared to the weaker general response of the blue channel in the same region, during sequential noise stimulation (cf. Fig. 4.2B,C). The location of the blue and UV RF centres of the dendritic ROI correspond to their position in visual space, and appear consistent with each other (Fig. 4.2D,E). Notably, the somatic ROI in the scan region (Fig. 4.2A, red oval) was non-responsive to all four wavebands during sequential noise stimulation (Fig. 4.2F) but displayed a particularly

robust response when presented with the single blue checkerboard stimulation (Fig. 4.2G). RF reconstruction revealed a spatially well-defined and pronounced RF, which also appeared to be larger in size compared to that of the dendritic ROI above it (cf. Fig. 4.2D). Its irregular shape differed as well from the typically round RFs we recovered from dendritic processes in general. Of note, the location of both the dendritic and somatic ROI in visual space appeared to vary according to the position of their RGC process within the IPL and GCL (Fig. 4.2A). Next, to introduce colour opponency, we presented combinations of a RGBU and a RGU checkerboard, with respective overlying checkerboards, i.e., RGU: a red, a green, and a UV checkerboard overlaid. However, when presenting the checkerboards together, red and green responses continue to dominate; conversely, no responses were registered in the blue and UV channels. In agreement, we were only able to reconstruct red and green RFs from the checkerboard overlays.

4.3. Discussion

4.3.1. Potential of spatiotemporal chromatic checkerboards as a RF mapping method

In general, our variation of flickering colour checkerboards revealed a small variety of RFs with slight differences in size, shape and position of the RF centre. Overall, the RF sizes reconstructed were consistently small, likely an indication that a 100x100-pixel size checkerboard is too large to define the spatial resolution of the RF of a typical RGC process in the larval zebrafish retina. Moreover, most RFs could be described as having a round, rather than an elliptical or irregular shape. A smaller-checker size relative to the RF centre should allow for finer resolution RF maps, to reveal a more well-defined centre and overall structure and shape of the RF, and in turn, greater differences in the variety of RFs.

A key practical issue is the length of time required to map RFs; the longer the period over which responses are measured, the higher the quality of the reconstruction. We started off

with, and find that 10 minutes of single colour flickering checkerboards with a 0.5-second frame duration was a good length to evoke robust responses and recover many spatial RFs within a scan field. Consequently, the length of acquisition time was likely one of the factors we were unable to recover stronger blue or any UV RFs during presentation of the sequential noise stimulus, taking into consideration that responses to both the blue and UV noise were more sparse over a given length of time. Another issue to consider is the masking of blue and UV responses during presentation of both the RGBU and RGU checkerboard overlays. It is possible that the red (at 100%) especially, and green (at 50%) LED powers, following a 'natural spectrum', were overpowering the blue and UV LED (at 13% and 6% respectively) in both space and time.

4.3.2. Motion stimuli to characterise feature detectors

Most known ganglion cells would respond to a small spot flashing in its receptive field centre. This includes looming detectors and object-motion-sensitive (OMS) cells. Yet, a static flashing spot is not readily encountered in natural vision. Instead, objects move into a neuron's receptive field from a neighbouring region, or move within the receptive field. Indeed, detecting movement of an object and its path is key to survival for any visually oriented animal, whether predator or prey. Consequently, motion and its direction are computed at multiple levels along the vertebrate visual pathway, starting in the retina. While spatiotemporal noise would provide a more detailed RF structure, the resultant description of RFs would be far from complete. To complement a comprehensive dataset, functional characterisation should ideally include more physiological stimuli that the animal encounters in its native environment.

4.3.2.1. Size selectivity and looming responses

Small moving spots, for instance, have been shown to evoke appetitive prey-capture behaviour in zebrafish (Bianco et al., 2011; Filosa et al., 2016; Semmelhack et al., 2014). These size-selective RGCs, with their relatively narrow dendritic field diameter (Preuss et al. 2014), in conjunction with their projection pattern to AF7, potentially identifies them as narrow-field bistratified or diffuse RGCs (Robles et al., 2014; Semmelhack et al. 2014). In contrast, RGC axons terminating in AF8 and AF6 are evoked by dimming and looming stimuli (Temizer et al. 2015), in line with anatomical reconstruction (Robles et al., 2014), strongly suggesting they originate from RGCs with large dendritic fields in the OFF layer of the IPL. Whether these signals arise from a genuine approach-sensitive ganglion cell type (Munch et al. 2009) or, from RGCs sensitive to large laterally moving edges (Del Bene et al. 2010, Preuss et al. 2014), warrants further investigation.

4.3.2.2. Orientation and direction selectivity

Natural visual scenes can be efficiently described by local, oriented filters with defined spatial structures (Simoncelli and Olshausen, 2001); unsurprisingly, orientation- and direction-selective neurons are present in the retinae of most, if not all, vertebrate species analysed to date, with species-specific differences in frequency and degree of tuning. Indeed, orientation- and direction-selectivity in the zebrafish is already computed at the level of the retina (Antinucci et al., 2016; Nikolaou et al., 2012; Lowe et al., 2013). Notably in the orientation-selective amacrine cell types described by Antinucci et al. (2016), orientation tuning appears to be a direct consequence of their highly elongated dendritic fields, rather than generated by upstream inhibitory mechanisms.

4.3.3. Refinement of motion stimuli to map RGC RFs

From our preliminary data, we have demonstrated the potential of using flickering chromatic checkerboards to map RGC RFs in the larval zebrafish eye. Our prototype tetrachromatic stimulator and stimulation protocols require further calibration and refinement, i.e., LED power adjustment, checker size. Natural visual stimuli are rarely homogenous spots of light or darkness; a RGC typically integrates a mix of local bright and dark-evoked events across its RF. Further, mapping RF features such as RF size, has direct implications on estimating the spatial extent of an RGC's dendrites, which in turn infers the morphological type of RGC associated with a specific function, i.e., size selectivity. We may draw several observations from the "punctate" response profiles; firstly, we are capturing the RFs of specific dendritic regions in space and time, but crucially, the checker sizes remain too crude to obtain meaningful information. Refining checker sizes should in theory reveal different shapes and sizes of these RFs. In the future, it will also be imperative to introduce more relevant salient stimuli, for instance instead of a moving bar stimulus, we could modify it to be a small moving UV spot, mimicking the size and appearance of a paramecium, the prey of the larval zebrafish. We could also further modify protocols where instead of moving in straight paths, the UV spot traces the path of what the paramecium may take in a natural setting.

Chapter 5

Conclusion and perspectives

5. Conclusions and perspectives

Defining cell types has been a reliable method for dissecting the function of neural circuits since Santiago Ramon y Cajal started cataloguing the brain's neuronal wildlife. To date, neuron types have been classified by gene expression pattern, morphological features, anatomical connectivity, and functional properties. Yet, we have not reached a consensus on a definitive classification of RGCs, largely due to the fact that the exact nature of visual information extracted in the retina is an ongoing debate (Baden et al., 2016; Masland, 2012). Notwithstanding, large-scale classifications ideally allow for an unbiased characterisation of retinal circuits, such as defining distinctive morphological features of RGC types, or the diversity of functional responses across the RGC population in response to a set of stimuli.

We have demonstrated that the retinal properties of the larval zebrafish is in line with the statistics of its visual surroundings, i.e., the distribution of spatial, temporal and spectral information, in addition to its species-specific behavioural demands, i.e., visually guided UV-prey capture. Further, even within this one species, the function of retinal circuits can vary substantially between different regions across the retina, challenging the traditionally-held notion that a neuron type that tiles the retina regularly also exhibits one stereotyped morphology and one function. Whether the properties of all retinal neurons vary systematically across the retinal surface remains an open question.

Because the ecological environment of animals share common visual characteristics, it is reasonable to expect some RGC types to be broadly conserved. These may include feature types that detect luminance, spectral contrast, edges, or motion. On the other hand, visual specialisations in eye designs, morphological and functional inhomogeneities across the retinal surface, and local circuit motifs mean that all species' retinae are unique. In general,

our understanding of the variation in species visual ecology, behavioural repertoire and evolutionary history, and their individual relationships with functional differences at the level of their retinal circuits, remains scarcely explored. This can be attributed to the fact that available data is drawn from a handful of mostly mammalian model species. Accordingly, to better understand vertebrate vision and its retinal computations, it is imperative to quantitatively relate different species' retinal functions to their ethological requirements.

Recent trends have been to use naturalistic stimuli to probe retinal circuit organization in the context of its function. Indeed, literature is full of examples of specialised computations in RGCs, shaped by selective pressure to extract ethologically relevant signals. Still, it remains a challenge to convincingly link functional local adaptations to properties of the natural environment.

The above arguments are all valid, and it has proven difficult to capture the dynamics of RGCs in a succinct manner. Perhaps instead of trying to impose a unifying framework on the diversity of computations that exist among RGCs, the strategy moving forward would be to appreciate the vast diversity of RGC types, including the dynamic nature of RGC RFs.

Bibliography

Allison W.T., Barthel L.K., Skebo K.M., Takechi M., Kawamura S., and Raymond P.A. (2010). Ontogeny of cone photoreceptor mosaics in zebrafish. J. Comp. Neurol. *518*, 4182–4195.

Antinucci, P., Folgueira, M., and Bianco, I.H. (2019). Pretectal neurons control hunting behaviour. eLife *8*, e48114.

Antinucci, P., Suleyman, O., Monfries, C. and Hindges, R. (2016). Neural mechanisms generating orientation selectivity in the retina. Curr. Biol. *26*, 1802–1815.

Applebury, M.L., Antoch, M.P., Baxter, L.C., Chun, L.L., Falk, J.D., Farhangfar, F., Kage, K., Krzystolik, M.G., Lyass, L.A., and Robbins, J.T. (2000). The murine cone photoreceptor: a single cone type expresses both S and M opsins with retinal spatial patterning. Neuron *27*, 513–523.

Arnold, K., and Neumeyer, C. (1987). Wavelength discrimination in the turtle pseudemys scripta elegans. Vision Research *27*, 1501-1511.

Attneave, F. (1954). Some informational aspects of visual perception. Psychol. Rev. *61*, 183–193.

Awatramani, G.B., and Slaughter, M.M. (2000). Origin of transient and sustained responses in ganglion cells of the retina. J. Neurosci. *20*, 7087–7095.

Baccus S.A., Olveczky B.P., Manu, M., and Meister, M. (2008). A retinal circuit that computes object motion. J Neurosci *28*, 6807–6817.

Baden, T., Berens, P., Franke, K., Roman-Roson, M., Bethge, M., and Euler, T. (2016). The functional diversity of retinal ganglion cells in the mouse. Nature *529*, 345–50.

Baden, T., Euler, T., and Berens, P. (2020). Understanding the retinal basis of vision across species. Nat. Rev. Neurosci *21*, 5-20.

Baden, T., and Osorio, D. (2019). The retinal basis of vertebrate color vision. Annu. Rev. Vis. Sci. *5*, 177-200.

Baden, T., Schubert, T., Berens, P., and Euler, T. (2018). The functional organization of vertebrate retinal circuits for vision. Oxford Res. Encycl. Neurosci.

Baden, T., Schubert, T., Chang, L. Le, Wei, T., Zaichuk, M., Wissinger, B., and Euler, T. (2013). A tale of two retinal domains: near-optimal sampling of achromatic contrasts in

natural scenes through asymmetric photoreceptor distribution. Neuron *80*, 1206–1217.

Bae, J.A., Mu, S., Kim, J.S., Turner, N.L., Tartavull, I., Kemnitz, N., Jordan, C.S., Norton, A.D., Silversmith, W.M., and Prentki, R. (2018). Digital Museum of Retinal Ganglion Cells with Dense Anatomy and Physiology. Cell *173*, 1293-1306.e19.

Barlow, H.B.H. (1961). Possible principles underlying the transformation of sensory messages. In Sensory Communication, pp. 217–234.

Barlow, H.B., and Hill, R.M. (1963). Selective sensitivity to direction of motion in ganglion cells of the rabbit's retina. Science. *139*, 412–414.

Bianco, I.H., Kampff, A.R., and Engert, F. (2011). Prey capture behavior evoked by simple visual stimuli in larval zebrafish. Front. Syst. Neurosci. *5*, 101.

Bergmann, K., Meza Santoscoy, P., Lygdas, K., Nikolaeva, Y., MacDonald, R.B., Cunliffe, V.T., and Nikolaev, A. (2018). Imaging Neuronal Activity in the Optic Tectum of Late Stage Larval Zebrafish. J Dev Biol. *6*, 6.

Bleckert, A., Schwartz, G.W., Turner, M.H., Rieke, F., and Wong, R.O.L. (2014). Visual space is represented by nonmatching topographies of distinct mouse retinal ganglion cell types. Curr. Biol. *24*, 310–315.

Bollmann, J.H. (2019). The zebrafish visual system: from circuits to behavior. Annu. Rev. Vis. Sci. *5*, 269–293.

Bowmaker, J.K., Heath, L.A., Wilkie, S.E., Hunt, D.M. (1997). Visual pigments and oil droplets from six classes of photoreceptor in the retinas of birds. Vis. Res. *37*, 2183–2194.

Breuninger, T., Puller, C., Haverkamp, S., and Euler, T. (2011). Chromatic bipolar cell pathways in the mouse retina. J. Neurosci. *31*, 6504–6517.

Briggman, K.L., Helmstaedter, M., and Denk, W. (2011). Wiring specificity in the direction-selectivity circuit of the retina. Nature *471*, 183–188.

Brown, S.P., He, S., and Masland, R.H. (2000). Receptive field microstructure and dendritic geometry of retinal ganglion cells. Neuron. *27*, 371–383.

Burrill, J.D., and Easter, S.S. Jr. (1994) Development of the retinofugal projections in the embryonic and larval zebrafish (Brachydanio rerio). J Comp Neurol *346*, 583-600.

Buzás, P., Blessing, E.M., Szmajda, B.A., and Martin, P.R. (2006) Specificity of M and L cone inputs to receptive fields in the parvocellular pathway: random wiring with functional bias. J Neurosci *26*, 11148–11161.

Calderone, J.B., Reese, B.E., and Jacobs, G.H. (2003) Topography of photoreceptors and retinal ganglion cells in the spotted hyena (Crocuta crocuta). Brain Behav Evol *62*, 182–192.

Calkins, D.J., Tsukamoto, Y., and Sterling, P. (1998) Microcircuitry and mosaic of a blue-yellow ganglion cell in the primate retina. J. Neurosci *18*, 3373–3385.

Cameron, D.A. (2002). Mapping absorbance spectra, cone fractions and neuronal mechanism to photopic spectral sensitivity in the zebrafish. Vis. Neurosci. *19*, 365–372.

Chang, L., Breuninger, T., and Euler, T. (2013). Chromatic coding from cone-type unselective circuits in the mouse retina. Neuron *77*, 559–571.

Chapot, C.A., Behrens, C., Rogerson, L.E., Baden, T., and Pop, S. (2017a). Local signals in mouse horizontal cell dendrites. Curr. Biol. *27*, 3603–3615.

Chapot, C.A., Euler, T., and Schubert, T. (2017b). How do horizontal cells 'talk' to cone photoreceptors? Different levels of complexity at the cone-horizontal cell synapse. J. Physiol. *595*, 5495–506.

Chichilnisky, E.J. (2001). A simple white noise analysis of neuronal light responses. Network *12*, 199–213.

Chinen, A., Hamaoka, T., Yamada, Y., and Kawamura, S. (2003). Gene duplication and spectral diversification of cone visual pigments of zebrafish. Genetics *163*, 663–675.

Church S,C., Bennett, A-T.D., Cuthill, I.C., and Partridge, J.C. (1998). Ultraviolet cues affect the foraging behaviour of blue tits. Proc. Royal Soc. Lond. B Biol. Sci, *265*, 1509–1514.

Connaughton, V.P., and Nelson, R. (2010). Spectral responses in zebrafish horizontal cells include a tetraphasic response and a novel UV-dominated triphasic response. J. Neurophysiol. *104*, 2407–2422.

Connaughton, V.P. and Nelson, R. (2015). Ultraviolet dominates ganglion cell responses in larval zebrafish. Invest. Ophthalmol. Vis. Sci. *56*, 3251.

Crook, J.D., Davenport, C.M., Peterson, B.B., Packer, O.S., Detwiler, P.B., and Dacey, D.M. (2009). Parallel ON and OFF cone bipolar inputs establish spatially coextensive

receptive field structure of blue-yellow ganglion cells in primate retina. J. Neurosci. *29*, 8372–8387.

Crook, J.D., Manookin, M.B., Packer, O.S., and Dacey, D.M. (2011). Horizontal cell feedback without cone type-selective inhibition mediates "red–green" color opponency in midget ganglion cells of the primate retina. Journal of Neuroscience *31*, 1762–1772.

Dacey, D.M. (2000). Parallel pathways for spectral coding in primate retina. Annu. Rev. Neurosci. *23*, 743–775.

Dacey, D.M. and Lee, B.B. (1994). The "blue-on" opponent pathway in primate retina originates from a distinct bistratified ganglion cell type. Nature *367*, 731–735.

De Vries, S.H. (2000). Bipolar cells use kainate and AMPA receptors to filter visual information into separate channels. Neuron *28*, 847–856.

De Vries, S.E., Baccus, S.A., and Meister,M. (2011). The projective field of a retinal amacrine cell. J. Neurosci. *31*, 8595–8604.

De Vries, S.H. and Baylor, D.A. (1997) Mosaic arrangement of ganglion cell receptive fields in rabbit retina. J Neurophysiol. *78*, 2048–2060.

Del Bene, F., Wyart, C., Robles, E., Tran, A., Looger, L., Scott, E.K., Isacoff, E.Y., and Baier, H. (2010). Filtering of visual information in the tectum by an identified neural circuit. Science. *330*, 669-673.

Demb, J.B., and Singer, J.H. (2012). Intrinsic properties and functional circuitry of the AII amacrine cell. Vis. Neurosci. *29*, 51–60.

Demb J.B., and Singer, J.H. (2015). Functional circuitry of the retina. Ann. Rev. Vis. Sci. *1*, 263-289.

Diamond, J.S. (2017). Inhibitory interneurons in the retina: types, circuitry, and function. Annu. Rev. Vis. Sci. *3*, 1-24.

Ding, H., Smith, R.G., Poleg-Polsky, A., Diamond, J.S., and Briggman, K.L. (2016). Species-specific wiring for direction selectivity in the mammalian retina. Nature *535*, 105–110.

Dominy, N.J., and Lucas, P.W. (2001) Ecological importance of trichromatic vision to primates. Nature *410*, 363–366.

Dunn, T.W.W., Gebhardt, C., Naumann, E.A.A., Riegler, C., Ahrens, M.B.B., Engert, F., Del Bene, F., and Del Bene, F. (2016). Neural circuits underlying visually evoked escapes in larval zebrafish. Neuron *89*, 613–628.

Endeman, D., Klaassen, L.J., and Kamermans, M. (2013). Action spectra of zebrafish cone photoreceptors. PLoS One *8*, e68540.

Engeszer, R.E., Patterson, L.B., Rao, A.A., and Parichy, D.M. (2007). Zebrafish in the wild: a review of natural history and new notes from the field. Zebrafish *4*, 21–40.

Engström, K. (1960). Cone types and cone arrangements in the retina of some cyprinids. Acta Zool. *41*, 277–295.

Enroth-Cugell, C., and Robson, J.G. (1966). The contrast sensitivity of retinal ganglion cells of the cat. J. Physio. *187*, 517–552.

Eggers, E.D., and Lukasiewicz, P.D. (2011). Multiple pathways of inhibition shape bipolar cell responses in the retina. Vis. Neurosci. *28*, 95–108.

Euler, T., Detwiler, P.B., and Denk, W. (2002). Directionally selective calcium signals in dendrites of starburst amacrine cells. Nature *418,* 845–852.

Euler, T., Franke, K., and Baden, T. (2019). Studying a light sensor with light: Multiphoton imaging in the retina. In Neuromethods, pp. 225-250.

Euler, T., Hausselt, S.E., Margolis, D.J., Breuninger, T., Castell, X., Detwiler, P.B., and Denk, W. (2009). Eyecup scope--optical recordings of light stimulus-evoked fluorescence signals in the retina. Pflugers Arch. *457*, 1393–1414.

Euler, T., Haverkamp, S., Schubert, T., and Baden, T. (2014). Retinal bipolar cells: elementary building blocks of vision. Nat. Rev. Neurosci. *15*, 507–519.

Ferguson, S.C.D., and McFarlane, S. (2002). GABA and development of the Xenopus optic projection. J. Neurobiol. *51,* 272–284.

Field, G.D., Gauthier, J.L., Sher, A., Greschner, M., Machado, T.A., Jepson, L.H., Shlens, J., Gunning, D.E., Mathieson, K., Dabrowski, W., Paninski, L., Litke, A.M., and Chichilnisky, E.J. (2010). Functional connectivity in the retina at the resolution of photoreceptors. Nature *467*, 673–677.

Filosa, A., Barker, A.J., Maschio, M.D., and Baier, H. (2016). Feeding state modulates behavioural choice and processing of prey stimuli in the zebrafish tectum. Neuron *90,* P596-608.

Franke, K and Baden, T. (2017). General features of inhibition in the inner retina. J. Physiol. *595,* 5507-5515

Franke, K., Chagas, A.M., Zhao, Z., Zimmermann, M.J.Y., Bartel, P., Qiu, Y., Szatko, K., Baden, T., and Euler, T. (2019). An arbitrary-spectrum spatial visual stimulator for vision research. eLife *8*, e48779.

Fried, S.I., Munch, T.A., Werblin, F.S. (2002). Mechanisms and circuitry underlying directional selectivity in the retina. Nature *420*, 411–414.

Gabriel, J.P., Trivedi, C.A., Maurer, C.M., Ryu, S., Bollmann, J.H. (2012). Layer-specific targeting of direction-selective neurons in the zebrafish optic tectum. Neuron *76*, 1147–1160.

Gahtan, E., Tanger, P., and Baier, H. (2005). Visual prey capture in larval zebrafish is controlled by identified reticulospinal neurons downstream of the tectum. J. Neurosci. *25*, 9294–9303.

Gollisch, T. and Meister, M. (2010). Eye smarter than scientists believed: neural computations in circuits of the retina. Neuron *65*, 150–164.

Guggiana-Nilo, D.A., Riegler, C., Hubener, M., and Engert, F. (2020). Colors everywhere: enhanced chromatic processing across the first visual synapse in the zebrafish central brain. bioRxiv.

Hart, N.S., and Hunt, D.M. (2007). Avian visual pigments: characteristics, spectral tuning, and evolution. Am. Nat. *169*, S7–26

Hartline, H.K. (1938). The responses of single optic nerve fibers of the vertebrate eye to illumination of the retina. Am J Physiol.121:400–415.

Huang, S.C., Chiou, T.H., Marshall, J., and Reinhard, J. (2014). Spectral sensitivities and color signals in a polymorphic damselfly. PLoS One *9*, e87972.

Hubbard, R., and Kropf, A. (1958). The action of light on rhodopsin. Proc. Natl. Acad. Sci. USA *44*, 130–139.

Hubel, D.H., and Wiesel, T.N. (1959). Receptive fields of single neurones in the cat's striate cortex. J. Physiol. *148*, 574–591.

Hubel, D.H., and Wiesel, T.N. (1962). Receptive fields, binocular interaction and functional architecture in the cat's visual cortex. J. Physiol. *160*, 106–154.

Janiak, F.K., Bartel, P., Bale, M., T, Y., Komulainen, E.H., Zhou, M., Staras, K., Prieto-Godino, L.L., Euler, T., and Maravall, M. (2019). Divergent excitation two photon microscopy for 3D random access mesoscale imaging at single cell resolution. bioRxiv 821405.

Johnston, J., Ding, H., Seibel, S.H., Esposti, F., and Lagnado, L. (2014). Rapid mapping of visual receptive fields by filtered back projection: application to multi-neuronal electrophysiology and imaging. J. Physiol. *592*, 4839–4854.

Johnston, J., Seibel, S-H., Darnet, L.S.A., Renninger, S., Orger, M., and Lagnado, L. (2019). A retinal circuit generating a dynamic predictive code for oriented features. Neuron *102*, 1211–1222.

Kamermans M., van Dijk B.W., and Spekreijse, H. (1991). Color opponency in cone-driven horizontal cells in carp retina: specific pathways between cones and horizontal cells. J. Gen. Physiol. *97*, 819–843.

Kim, J.S., Greene, M. J., Zlateski, A., Lee, K., Richardson, M., Turaga, S.C., Purcaro, M., Balkam, M., Robinson, A., Behabadi, B.F., Campos, M., Denk, W., and Seung, H.S. (2014). Space–time wiring specificity supports direction selectivity in the retina. Nature *509*, 331–336.

Kim, T., Soto, F., and Kerschensteiner, D. (2015). An excitatory amacrine cell detects object motion and provides feature-selective input to ganglion cells in the mouse retina. eLife *4*, e08025

Klaassen, L.J., de Graaff, W., van Asselt, J.B., Klooster, J., and Kamermans, M. (2016). Specific connectivity between photoreceptors and horizontal cells in the zebrafish retina. J. Neurophysiol. *116*, 2799–2814.

Krauskopf , J., Williams, D.R., and Heeley, D.W. (1982). Cardinal directions of color space. Vis. Res. *22*, 1123–1131.

Krauss, A., and Neumeyer, C. (2003). Wavelength dependence of the optomotor response in zebrafish (Danio rerio). Vis. Res. *43*, 1273–1282.

Kubo, F., Hablitzel, B., Maschio, M., Driever, W., Baier, H., and Arrenberg, A. (2014). Functional architecture of an optic flow-responsive area that drives horizontal eye movements in zebrafish. Neuron *81*, 1344–1359.

Kuffler, S.W. (1953) Discharge patterns and functional organization of mammalian retina. J. Neurophysiol. *16*, 37-68.

Kuffler, S.W. (1973). The single-cell approach in the visual system and the study of receptive fields. Invest. Ophthalmol. *12*, 794–813.

Land, M., and Nilson, D.-E. (2012). Animal Eyes (Oxford University Press).

Lee, B.B., Martin, P.R., Grünert, U. (2010). Retinal connectivity and primate vision. Prog. Retinal Eye Res. *29*, 622–639.

Lettvin, J.Y., Maturana, H.R., McCulloch, W.S, and Pitts, W.H. (1959). What the frog's eye tells the frog's brain. Proceedings of the Institute of Radio Engineers, *47*, 1940–1951.

Levick, W.R. (1967). Receptive fields and trigger features of ganglion cells in the visual streak of the rabbits retina. J Physiol. *188*, 285–307.

Li, Y.N., Matsui, J.I., and Dowling, J.E. (2009). Specificity of the horizontal cell-photoreceptor connections in the zebrafish (Danio rerio) retina. J. Comp. Neurol. *516*, 442–453.

Li, Y.N., Tsujimura, T., Kawamura, S., and Dowling, J. (2012). Bipolar cell-photoreceptor connectivity in the zebrafish (Danio rerio) retina. J. Comp. Neurology *520*, 3786–3802.

Liang, L., Fratzl, A., Mansour, O. El, Reggiani, J.D.S., Chen, C., and Andermann, M.L. (2020). Selective gating of retinal information by arousal. bioRxiv 2020.03.12.989913.

Lindstrom, S.H., Ryan, D.G., Shi, J., and Devries, S.H. (2014). Kainate receptor subunit diversity underlying response diversity in retinal Off bipolar cells. J. Physiol. *592*, 1457–1477.

Lowe, A.S., Nikolaou, N., Hunter, P.R., Thompson, I.D., and Meyer, M.P. (2013). A systems-based dissection of retinal inputs to the zebrafish tectum reveals different rules for different functional classes during development. J. Neurosci. *35*, 13946–13956.

MacNeil, M.A., and Masland, R.H. (1998). Extreme diversity among amacrine cells: implications for function. Neuron *20*, 971–982.

Marre, O., Amodei, D., Deshmukh, N., Sadeghi, K., Soo, F., Holy, T.E., and Berry, M.J. (2012). Mapping a complete neural population in the retina. J. Neurosci. *32*, 14859–14873.

Marshak, D.W., and Mills, S.L. (2014). Short-wavelength cone-opponent retinal ganglion cells in mammals. Vis. Neurosci. *31*, 165–175.

Martin, P.R., Lee, B.B., White, A.J., Solomon, S.G., and Rüttiger, L. (2001). Chromatic sensitivity of ganglion cells in the peripheral primate retina. Nature *410*, 933–936.

Masland, R.H. (2001). The fundamental plan of the retina. Nat. Neurosci. *4*, 877–886.

Masland, R.H. (2012a) The neuronal organization of the retina. Neuron *76*, 266-280.

Masland, R.H. (2012b). The tasks of amacrine cells. Vis. Neurosci. *29*, 3–9.

Matsumoto, A., Briggman, K.L., and Yonehara, K. (2019). Spatiotemporally asymmetric excitation supports mammalian retinal motion sensitivity. Curr. Biol. *29*, 3277–3288.

McElligott, M.B., and O'Malley, D.M. (2005). Prey tracking by larval zebrafish: Axial kinematics and visual control. Brain. Behav. Evol.

Mearns, D.S., Donovan, J.C., Fernandes, A.M., Semmelhack, J.L., and Baier, H. (2020). Deconstructing hunting behavior reveals a tightly coupled stimulus-response loop. Curr. Biol. *30*, 54-69.e9.

Meier, A., Nelson, R,. and Connaughton ,V.P. (2018). Color processing in zebrafish retina. Front. Cell Neurosci. *12*, 327.

Meister, M., Pine, J. and Baylor, D.A. (1994). Multi-neuronal signals from the retina: acquisition and analysis. J. Neurosci. Methods *51*, 95–106.

Mills, S.L., Tian, L.M., Hoshi, H., Whitaker, C.M., and Massey, S.C. (2014). Three distinct blue-green color pathways in a mammalian retina. J. Neurosci. 34, 1760–1768.

Morshedian, A., and Fain, G.L. (2015). Single-photon sensitivity of lamprey rods with cone-like outer segments. Curr. Biol. *25*, 484-487.

Münch ,T.A., da Silveira, R.A., Siegert, S., Viney, T.J., Awatramani, G.B., and Roska, B. (2009). Approach sensitivity in the retina processed by a multifunctional neural circuit. Nat. Neurosci. *12*,1308–1316.

Muto, A., Ohkura, M., Abe, G., Nakai, J., and Kawakami, K. (2013). Real-time visualization of neuronal activity during perception. Curr. Biol. *23*, 307–311.

Muto, A., Lal, P., Ailani, D., Abe, G., Itoh, M., and Kawakami, K. (2017). Activation of the hypothalamic feeding centre upon visual prey detection. Nat. Commun. *8*, 15029.

Nathans, J. (1999). The evolution and physiology of human color vision: insights from molecular genetic studies of visual pigments. Neuron *24*, 299–312.

Naumann, E.A., Fitzgerald, J.E., Dunn, T.W., Rihel, J., Sompolinsky, H., and Engert, F. (2016). From whole-brain data to functional circuit models: The zebrafish optomotor response. Cell *167*, 947–960.e20.

Neitz, J. and Neitz, M. (2011). The genetics of normal and defective color vision. Vision Res. *51*, 633–651.

Neumeyer, C. (1992). Tetrachromatic color vision in goldfish: evidence from color mixture experiments. J. Comp. Physiol. A *171*, 639–649.

Nevala, N.E., and Baden, T. (2019). A low-cost hyperspectral scanner for natural imaging and the study of animal colour vision above and under water. Sci. Rep. *9*, 10799.

Nikolaou, N., Lowe, A.S., Walker, A.S., Abbas, F., Hunter, P.R., Thompson, I.D., and Meyer, M.P. (2012). Parametric functional maps of visual inputs to the tectum. Neuron, *76*, 317-324.

Niell, C. M., and Smith, S. J. (2005). Functional imaging reveals rapid development of visual response properties in the zebrafish tectum. Neuron *45*, 941–951.

Orger, M.B., and Baier, H. (2005). Channeling of red and green cone inputs to the zebrafish optomotor response. Vis. Neurosci. *22*, 275–281.

Ölveczky, B.P., Baccus, S.A., and Meister, M. (2003). Segregation of object and background motion in the retina. Nature *423*, 401–408.

Packer, O.S., Verweij, J., Li, P.H., Schnapf, J.L., and Dacey, D.M. (2010). Blue-yellow opponency in primate S cone photoreceptors. J. Neurosci. *30*, 568–572.

Parichy, D.M. (2015). Advancing biology through a deeper understanding of zebrafish ecology and evolution. eLife *4*, e05635.

Patterson, B.W., Abraham, A.O., MacIver, M.A., and McLean, D.L. (2013). Visually guided gradation of prey capture movements in larval zebrafish. J. Exp. Biol. *216*, 3071–3083.

Peichl, L. (2005) Diversity of mammalian photoreceptor properties: adaptations to habitat and lifestyle? Anat. Rec. A Discov. Mol. Cell Evol. Biol. *287*, 1001–1012.

Peichl, L. and Wassle, H. (1979). Size, scatter and coverage of ganglion cell receptive field centres in the cat retina. J Physiol. *291*, 117–141.

Perlman, I., Weiner, E., and Kolb, H. (2009). Retinal horizontal cells. In Encyclopedia of Neuroscience, ed. LR Squire, pp. 233–43. New York: Academic.

Pittman, A.J., Law, M.-Y., and Chien, C.-B. (2008). Pathfinding in a large vertebrate axon tract: isotypic interactions guide retinotectal axons at multiple choice points. Development *129*, 617–624.

Preuss, S.J., Trivedi, C.A., vom Berg-Maurer, C.M., Ryu, S., and Bollmann, J.H. (2014). Classification of Object Size in Retinotectal Microcircuits. Curr. Biol. *24*, 2376–2385.

Puller, C., and Haverkamp, S. (2011). Bipolar cell pathways for color vision in non-primate dichromats. Vis. Neurosci. *28*, 51–60.

Puller, C., Ivanova, E., Euler, T., Haverkamp, S., and Schubert, T. (2013). OFF bipolar cells express distinct types of dendritic glutamate receptors in the mouse retina. Neuroscience *243*, 136–148.

Raymond, P.A., Barthel, L.K., Rounsifer, M.E., Sullivan, S.A., and Knight, J.K. (1993). Expression of rod and cone visual pigments in goldfish and zebrafish: A rhodopsin-like gene is expressed in cones. Neuron *10*, 1161–1174.

Robles, E., Laurell, E., and Baier, H. (2014). The retinal projectome reveals brain-area-specific visual representations generated by ganglion cell diversity. Curr. Biol. *24*, 2085–2096.

Robinson, J., Schmitt, E. A., Hárosi, F. I., Reece, R. J., and Dowling, J. E. (1993). Zebrafish ultraviolet visual pigment: absorption spectrum, sequence, and localization. Proc. Natl. Acad. Sci. USA *90*, 6009–6012.

Röhlich, P., van Veen, T., and Szel, A. (1994). Two different visual pigments in one retinal cone cell. Neuron *13*, 1159–1166.

Roska, B., and Meister, M. (2014). The retina dissects the visual scene into distinct features. In: Werner J.H, Chalupa L.M, editors. The new visual neurosciences. Cambridge, MA: MIT Press; pp. 163–183.

Roska, B., Nemeth, E., and Werblin, F.S. (1998). Response to change is facilitated by a three-neuron disinhibitory pathway in the tiger salamander retina. J. Neurosci. *18*, 3451–3459.

Roska, B. and Werblin, F.S. (2001). Vertical interactions across ten parallel, stacked representations in the mammalian retina. Nature *410*, 583–587.

Sabbah, S., Gemmer, J.A., Bhatia-Lin, A., Manoff, G., Castro, G., Siegel, J.K., Jeffery, N., and Berson, D.M. (2017). A retinal code for motion along the gravitational and body axes. Nature *546*, 492–497.

Sabbah, S., Laria, R.L., Gray, S.M., and Hawryshyn, C.W. (2010). Functional diversity in the color vision of cichlid fishes. BMC Biol. 8, 133.

Sajovic, P., and Levinthal, C. (1982a) Visual cells of zebrafish optic tectum: mapping with small spots. Neuroscience 7, 2407–2426.

Sajovic, P., and Levinthal, C., (1982b). Visual response properties of zebrafish tectal cells. Neuroscience 7, 2427–2440.

Sajovic, P., and Levinthal, C. (1983). Inhibitory mechanism in zebrafish optic tectum: Visual response properties of tectal cells altered by picrotoxin and bicuculline. Brain Res. *271,* 227–240.

Sanes J.T. and Masland, R.H. (2015). The types of retinal ganglion cells: current status and implications for neuronal classification. Annu. Rev. Neurosci. *38,* 221-246.

Schmitt, E.A., and Dowling, J.E. (1999). Early retinal development in the zebrafish, Danio rerio: light and electron microscopic analyses. *404*, 515–536.

Schwartz, G. and Rieke, F. (2011). Nonlinear spatial encoding by retinal ganglion cells: when 1 + 1 ≠ 2. J. Gen. Physiol. *138*, 283–290.

Semmelhack, J.L., Donovan, J.C., Thiele, T.R., Kuehn, E., Laurell, E., and Baier, H. (2014). A dedicated visual pathway for prey detection in larval zebrafish. eLife *3*, e04878.

Sher, A. and DeVries, S.H. (2012). A non-canonical pathway for mammalian blue-green color vision. Nat. Neurosci. *15,* 952–953.

Simoncelli, E.P., and Olshausen, B.A. (2001). Natural image statistics and neural representation. Annu. Rev. Neurosci. *24,* 1193–1216.

Sinha, R., Hoon, M., Baudin, J., Okawa, H., Wong, R.O.L., and Rieke, F. (2017). Cellular and circuit mechanisms shaping the perceptual properties of the primate fovea. Cell *168*, 413-426.e12.

Song, P.I., Matsui, J.I., and Dowling, J.E. (2008). Morphological types and connectivity of horizontal cells found in the adult zebrafish (Danio rerio) retina. J. Comp. Neurol. *506*, 328–338.

Szatko, K.P., Korympidou, M.M., Ran, Y., Berens, P., Dalkara, D., Schubert, T., Euler, T., and Franke, K. (2019). Neural circuits in the mouse retina support color vision in the upper visual field. bioRxiv 745539.

Temizer, I., Donovan, J.C., Baier, H., and Semmelhack, J.L. (2015). A visual pathway for looming-evoked escape in larval zebrafish. Curr. Biol. *25,* 1823–1834.

Thoen, H.H., How, M.J., Chiou, T-H., and Marshall, J. (2014). A different form of color vision in mantis shrimp. Science, *343*, 411–413.

Thoreson, W.B., Babai, N., and Bartoletti, T.M. (2008). Feedback from horizontal cells to rod photoreceptors in vertebrate retina. J. Neurosci. *28*, 5691–5695.

Thoreson, W.B. and Dacey, D.M. (2019). Diverse cell types, circuits, and mechanisms for color vision in the vertebrate retina. Physiol. Rev. *99*, 1527–1573.

Toomey, M.B., Collins, A.M., Frederiksen, R., Cornwall, M.C., Timlin, J.A., and Corbo, J.C. (2015). A complex carotenoid palette tunes avian colour vision. J. R. Soc. Interface *12*, 20150563.

Torvund, M.M., Ma, T.S., Connaughton, V.P., Ono, F., and Nelson, R.F. (2017). Cone signals in monostratified and bistratified amacrine cells of adult zebrafish retina. J. Comp. Neurol. *525*, 1532–1557.

Trivedi, C.A., and Bollmann, J.H. (2013). Visually driven chaining of elementary swim patterns into a goal-directed motor sequence: a virtual reality study of zebrafish prey capture. Front. Neural Circuits *7*, 86.

Twig, G., Levy, H., and Perlman, I. (2003). Color opponency in horizontal cells of the vertebrate retina. Prog. Retinal Eye Res. *22*, 31–68.

Vlasits, A.L., Euler, T., and Franke, K. (2019). Function first: classifying cell types and circuits of the retina. Curr. Opin. Neurobiol. *56*, 8–15.

Warwick, R.A., Kaushansky, N., Sarid, N., Golan, A., and Rivlin-Etzion, M. (2018). Inhomogeneous encoding of the visual field in the mouse retina. Curr. Biol. *28*, 655–665.

Wässle, H. (2004). Parallel processing in the mammalian retina. Nat. Rev. Neurosci. *5*, 1–11.

Werblin, F.S. (2010). Six different roles for crossover inhibition in the retina: correcting the nonlinearities of synaptic transmission. Vis. Neurosci. *27*, 1–8.

Wool, L.E., Packer, O.S., Zaidi, Q., and Dacey, D.M. (2019). Connectomic identification and three-dimensional color tuning of S-OFF midget ganglion cells in the primate retina. J. Neurosci.

Yin, L., Smith, R.G., Sterling, P., and Brainard, D.H. (2009). Physiology and morphology of color-opponent ganglion cells in a retina expressing a dual gradient of S and M opsins. J. Neurosci. *29*, 2706–2724.

Yoshimatsu, T., Schröder, C., Nevela, N. E., Berens, P., and Baden, T. (2020). Fovea-like photoreceptor specializations underlie single UV cone driven prey-capture behaviour in zebrafish. Neuron. *107*, P320-337.E6.

Yoshimatsu, T., Williams, P.R., D'Orazi, F.D., Suzuki, S.C., Fadool, J.M., and Allison, W. (2014). Transmission from the dominant input shapes the stereotypic ratio of photoreceptor inputs onto horizontal cells. Nat. Commun. *5*, 3699.

Zhang, Y., Kim, I.J., Sanes, J.R., and Meister, M. (2012). The most numerous ganglion cell type of the mouse retina is a selective feature detector. Proc. Natl. Acad. Sci. USA *109*, E2391–E2398.

Zhang, M., Liu, Y., Wang, S.-Z., Zhong, W., Liu, B.-H., and Tao, H.W. (2011). Functional elimination of excitatory feed forward inputs underlies developmental refinement of visual receptive fields in zebrafish. J. Neurosci. *31*, 5460–5469.

Zhou, M., Bear, J., Roberts, P.A., Janiak, F.K., Semmelhack, J., Yoshimatsu, T., and Baden, T. (2020). Zebrafish retinal ganglion cells asymmetrically encode spectral and temporal information across visual space. Current Biology *30*: 1-16.

Zimmermann, M.J.Y., Nevala, N.E., Yoshimatsu, T., Osorio, D., Nilsson, D-E., Berens, B., and Baden, T. (2018). Zebrafish differentially process color across visual space to match natural scenes. Curr. Biol. *28*, 2018-2032.E5.

Zrenner, E. and Gouras, P. (1981). Characteristics of the blue sensitive cone mechanism in primate retinal ganglion cells. Vis. Res. *21*, 1605–1609.

Appendix

Supplementary Material for Chapter 3

This section contains the supplementary figures referenced in Chapter 3.

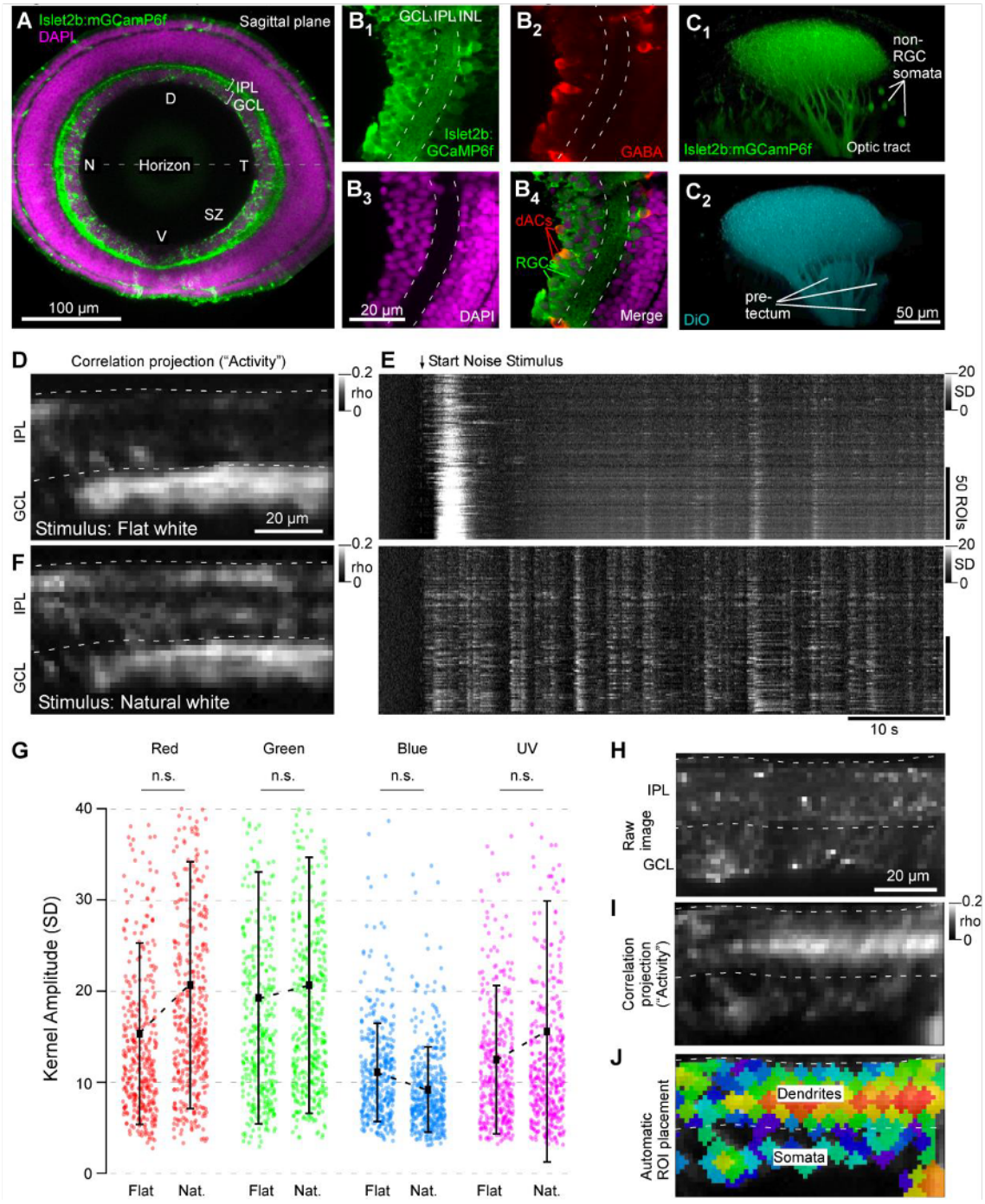

Supplementary Figure S1 | related to Figure 3.1. Islet2b expression, stimulation with 'natural' white light and ROI placement. A, 7 dpf larva whole-eye sagittal plane confocal image of Islet2b:mGCaMP6f expression (green) on the background of a DAPI stain, labelling all somata (magenta). D, dorsal; T, temporal; V, ventral; N, Nasal; AZ, Acute zone; INL Inner nuclear layer; GCL, Ganglion cell layer. **B_{1-4},** Example higher magnification as in (A) from a second animal, with additional immunolabelling for GABA (red) to reveal GABAergic dACs and AC. Note the subset of somata showing both GABA labelling and mGCaMP6f expression (B_4). Note also the near doubling of GCL thickness across the region from the ventral retina

(bottom) leading into the AZ (top). **C,** Confocal projections of mGCaMP6f signal in the brain (C_1) and counter labelling by DiO injection in the eye (C_2). Though generally similar, C_1 shows expression in small numbers of brain-somata, while C_2 shows stronger labelling in pretectal axonal arborisation fields. **D-F,** Comparison of light-evoked activity in the same scan region in the SZ during stimulation with spectrally-flat white-noise (D, E top) and identical sequence 'natural spectrum' white noise (i.e. with green, blue and UV attenuated relative to red, cf. Fig. 3.1B) (F, E bottom). Panels D,F show the correlation projection for the entire scan, while E top and bottom shows heatmaps of all extracted ROIs from each scan, respectively. Note the strong initial response when starting the noise-stimulus in the flat-white condition (E, top), followed by an extended period of response suppression. In contrast, ROIs during the natural-white condition responded briskly to the noise sequence without showing strong adaptation (E, bottom). Similarly, a more diverse set of scan-regions strongly responded in the natural white condition (F) compared to flat-white (D). **G,** The mean of the distributions of resultant kernel amplitudes across n=6 such scans from an identical number of animals (n=388 and 428 ROIs for the flat and natural-white condition, respectively) were indistinguishable (Wilcoxon Rank Sum Test, 2 tailed). Based on these results, we decided to use natural-white noise stimulation throughout this study. **H-J,** example scan demonstrating typical automated ROI placement. The scan was manually segmented into IPL (H, top) and GCL (H, bottom). In parallel, we computed mean correlation over time between all pairs of neighbouring pixels for the entire scan (I), and the resultant correlation-projection image was in turn used to seed and flood-fill ROIs (J). For further details and a discussion about the rationale of this approach, see (Franke et al., 2017).

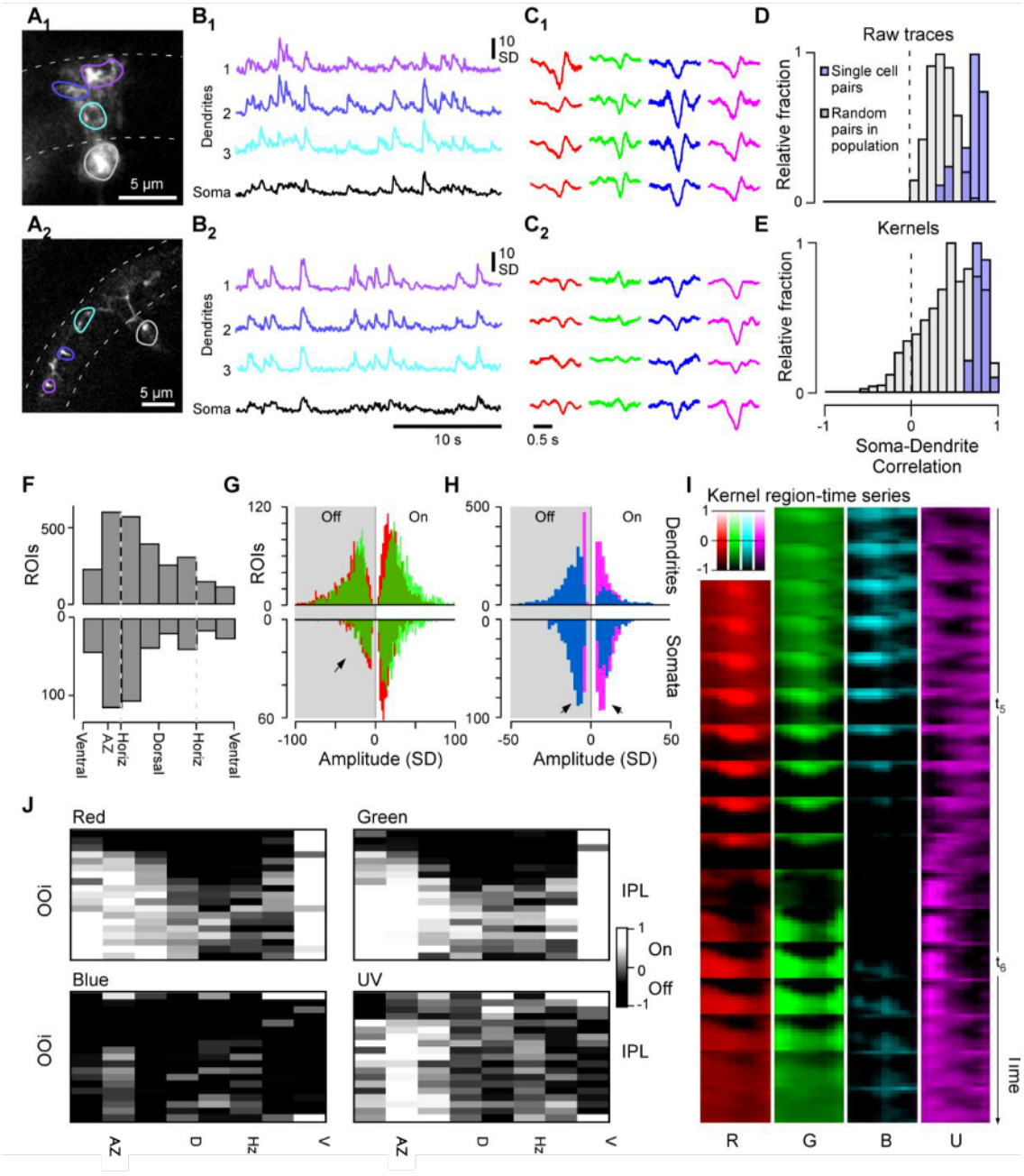

Supplementary Figure S2 | related to Figure 3.2. Linking dendritic with somatic data and eye-wide overview of RGC functions. A-C, Correlations of mGCaMP6f signals and spectral kernels from pairs of soma and dendrites belonging to the same cell, achieved by a transient expression strategy (Methods). Two RGC examples with distinct morphologies (A_1-C_1small-field and diffuse from AZ; A_2-C_2 widefield and narrow from nasal retina) are highlighted: A, High resolution 2P scan of individual RGCs in the live eye with IPL boundaries and manually placed ROIs highlighted. B, example activity traces from each of these ROIs to naturalistic white-noise stimulation (cf. Suppl. Fig. S1E) and C, spectral kernels extracted from each ROI. Note that by and large, dendritic and somatic responses (B) and kernels (C) from the same cell are very similar. **D, E,** Quantification of correlations in pairs of somatic and dendritic ROIs (light purple) of raw activity traces (D) and of kernels (E). Data from n = 7 single RGCs with a total of 20 soma-dendrite pairs is shown. For comparison, the same analysis was performed for n = 400 random within-scan pairs of somatic and dendritic ROIs from n=4 nasal/dorsal population scans comprising n = 24, 16, 7, 13 somatic and n = 99, 69, 69 and 42 dendritic ROIs, respectively (light grey). In both cases, single-cell pairs were significantly more correlated than random population pairs ($p<0.001$ Wilcoxon Rank Sum test, 1 tailed), indicating that in general dendritic responses provide a useful - albeit not perfect - approximation of somatic responses. **F,** Number of dendritic (top) and somatic (bottom, y-flipped) ROIs recorded across different positions in the eye. The relative abundance of AZ-ROIs is in line with the increased RGC numbers and thicker retinal layers (Zimmermann et

al., 2018) in this part of the eye (cf. Suppl. Fig. S4). **G,H,** Distribution of dendritic (top) and somatic (bottom) On- and Off-kernels (as in Fig. 3.2A), divided into the four wavebands, with red/green (G) and blue/UV shown together (H). Chi-Squared with Yates correction for On:Off distributions dendrites vs. somata: $p < 0.00001$ in all cases except blue, where $p = 0.0018$. I, Eye-IPL maps for R/G/B/U kernels (cf. Fig. 3.2J) plotted over time (cf. Suppl. Video S4) J, Projection of an On-Off index (OOi, Methods) in the four wavebands (as in Fig. 3.2J) into an Eye-IPL map, with lighter and darker shades indicating an overall On- and Off- bias, respectively (see also Suppl. Fig. S2G,H).

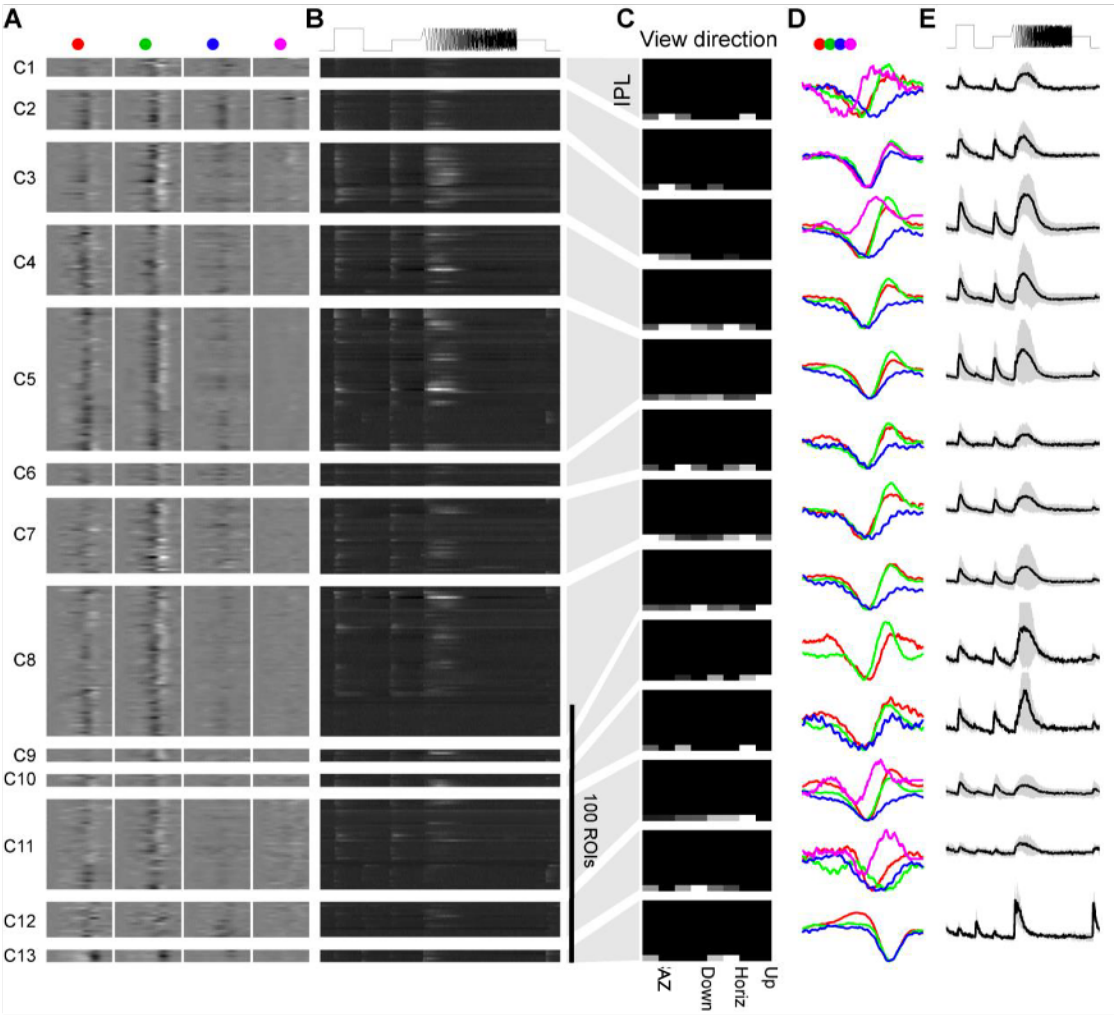

Supplementary Figure S3 | related to Figure 3.4. Functional clustering of somatic ROIs across the eye. A-E, Somatic data from across the eye clustered based on spectral kernels, presented following the same organisation as used for dendritic data (Fig. 3.4 A-F).

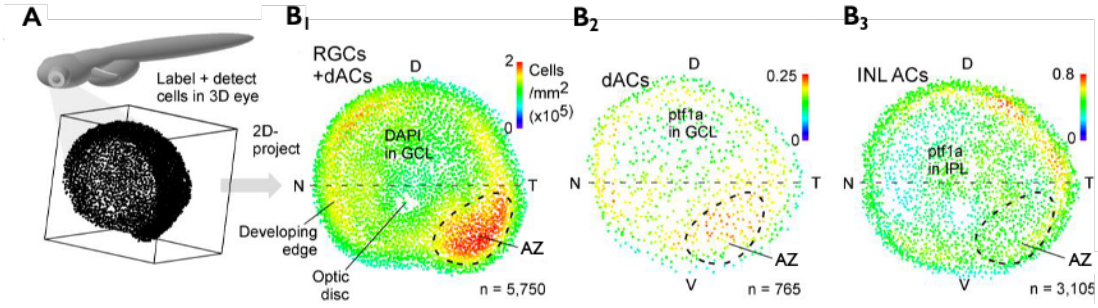

Supplementary Figure S4 | **Elevated RGC density in the acute zone.** (immunostaining and cell count by JB, cell density plot by TY; included to provide context to Discussion). **A,** Schematic of larval zebrafish and enlarged 3D representation of GCL nuclei in the eye. **$B_{1\text{-}3}$,** 2D projections of detected soma positions across the eye of all GCL cells based on a DAPI stain which includes all RGCs and all dACs ($_1$) and selective isolation of amacrine cells in the GCL (dACs , $_2$) and INL (ACs, $_3$) based on ptf1a labelling. N = 1 eye. D, Dorsal; N, Nasal; V, Ventral; T, Temporal, AZ, Acute zone.

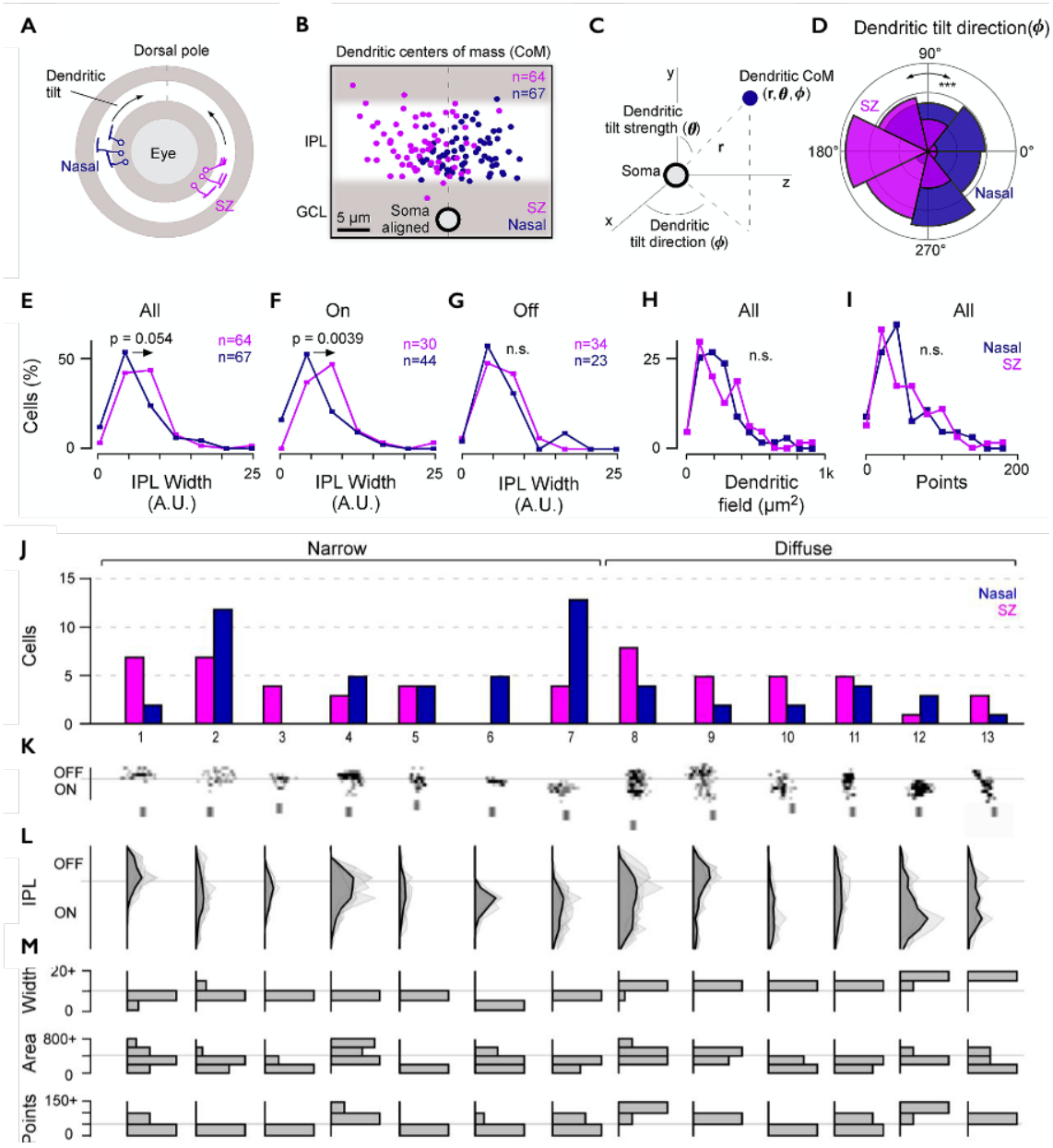

Supplementary Figure S5 | Anatomical distribution of morphological RGC types across the eye. (separate experiments performed by JB, included to provide context to Discussion). **A-I,** A total of n = 64 and n = 67 randomly targeted RGCs from the AZ and nasal retina, respectively, were processed for further analysis, which included computation of their dendritic tilt (A-D), stratification widths within the IPL (E-G), *en face* dendritic field area (L), and total number of detected dendritic structures ('points'; M; Methods). The dendrites of nasal (purple) and SZ (pink) RGCs both tended to tilt toward the eye's dorsal pole (A: schematic; B: soma-aligned data of all dendrites' center of mass). Dendritic tilt was quantified in soma-centered polar coordinates based on the Cartesian x,y,z coordinates that emerge from the original image stacks (C), such that r: distance in microns between soma and dendritic center of mass, θ (0°:90°): strength of the dendritic tilt (0° and 90° denoting no tilt and maximal positive tilt, respectively), and ϕ (0°:360°): direction of the dendritic tilt in approximately retinotopic space (approximate as the eye is curved). ϕ significantly differed between nasal and AZ RGCs (D). For summarizing widths, RGCs were considered as a single group (E) or split into On and Off RGCs (F and G, respectively), based on the IPL depths of their dendritic center of mass (here, the upper third of the IPL was considered "Off" and the bottom two-thirds were considered "On"). Kolmogorov-Smirnov test for circular statistics (D) and Wilcoxon rank sum test, 1 tailed (E-I), is shown. **J-M,** summarises an asymmetric distribution of anatomical RGC types across the eye. Photoconverted and processed RGCs from both nasal and AZ (A-I) were jointly clustered based on morphological criteria (Methods). **J,** Number of RGCs for AZ (pink/ left) and nasal retina (blue/right) allocated to each of n = 13

clusters. **K,** Individual RGC morphologies representative for each cluster. Note that each morphology's depth profile (y) is stretched five-fold relative to its lateral spread (x) to highlight stratification differences between clusters. **L,** Mean (dark) and individual depth profiles (light) and **M,** distribution of widths, dendritic field area and number of puncta for each cluster. Clusters were divided into narrow (left) and diffusely stratified (right) based on their mean widths (M, top, cf. labels in J).

Supplementary Video Legends

This section contains the legends for the supplementary videos referenced in Chapter 3.

Supplementary Video S1 | Example 2P scan from RGCs in the live eye, related to Fig. 3.1. Background-subtracted but otherwise 'raw' fluorescence responses of the example recording summarised in Fig. 3.1C–H. RGC dendrites (top half) and somata (bottom half) respond to the presentation of full field tetrachromatic noise stimulation. Video plays at real time.

Supplementary Video S2 | RGC dendritic mean responses across the eye to a step of light, related to Fig. 3.2C–G. Average Eye(x)-IPL(y) response over time across our entire dataset to an achromatic step of light, as shown in Fig. 3.2F ($t_{1,2}$) and Fig. 3.2G (left panels), starting with the Off-response (responses in the top of the IPL), followed by the On-response (bottom of the IPL). 'Hot' colours indicate increased activity. Video plays in real time.

Supplementary Video S3 | RGC dendritic mean responses across the eye to temporal flicker, related to Fig. 3.2C–G. As Suppl. Video S2, but for the temporal flicker portion of the stimulus ($t_{3,4}$). 'Hot' colours indicate increased activity. Video plays in real time.

Supplementary Video S4 | RGC dendritic mean 4-Color kernels across the eye, related to Fig. 3.2H–J. As Suppl. Video S2, but instead of showing the mean step/flicker responses to achromatic stimulation, showing the average temporal kernels recovered from tetrachromatic stimulation (cf. Fig. 3.2H–J and Suppl. Fig. S2I). From top left to bottom right: Red, Green, Blue, UV. Stronger colours indicate deviations above baseline. For clarity, approximately equal and opposite deviations below baseline are masked in this colour map and appear black. Video plays at 25% real time.